The Dissertation Committee for Sudip Chakraborty Certifies that this is the approved version of the following dissertation:

Interaction between Aerosols and the Mesoscale Convective Systems over the Tropical Continents

Committee:

Rong Fu, Supervisor

Robert E. Dickinson

Zong-Liang Yang

David T. Allen

Steven T. Massie

Jose Marengo

Interaction between Aerosols and the Mesoscale Convective Systems over the Tropical Continents

by

Sudip Chakraborty, B.E.; M.Tech

Dissertation

Presented to the Faculty of the Graduate School of

The University of Texas at Austin

in Partial Fulfillment

of the Requirements

for the Degree of

Doctor of Philosophy

The University of Texas at Austin

May 2016

Dedication

To,

Rik

Acknowledgements

There would be no words that can thank my supervisor Dr. Rong Fu enough. My dream of higher education and pursuing a Ph.D. would not have been possible had there been no support and the letter of acceptance from her when I was in India. She is a great supervisor. She taught me the scientific knowledge, writing, and helped improving my research skills. Her instructions and the courses she taught have shown me the road map to be a scientist from an undergraduate student. The transition from an undergrad to a scientist found a responsible, caring, and innovative hands of Rong. Not only she is a great inspiration and enthusiastic supervisor to me, her friendly nature has helped me a lot in difficult and tough times in life. Her supportive and warm-hearted supervision have always helped me to be confident in research during my degree requirements and achieving my future goals. She has always encouraged me to work in the research of my choice and I am fortunate that I would continue to work with her after my graduation.

It would have been impossible without my three year's old little daughter, Sharanya, whose innocent, cute, beautiful smiles, and love are the biggest sources of energy and enthusiasm for me. She is the reason I feel responsible, caring, and dedicated to my family and work. It's her love that shows me the steps in the future. She makes me feel the importance of my life.

I want to thank Dr. Steven T. Massie for his great support and guidance for the progress of my research projects and the knowledge he shared to improve my manuscripts and scientific writing.

Thanks to my parents and Monalisa. It would have been impossible without the basic knowledge of everything they taught me and the courage and support they gave me. Thanks to all my professors in UT Austin for showing me

the pathway of being a scientist by enriching my knowledge and encouraging me to ask questions, which is immensely important to being a scientist.

Thanks to Dr. Jonathon S. Wright and Dr. Graeme Stephens for their insightful contributions to our publications. I acknowledge my dissertation committee members, Drs. Robert E. Dickinson, Zong-Liang Yang, and David T. Allen for their important feedback during my defense process.

I also acknowledge my research group members in UT Austin. It has been a pleasure to work with all of them. Thanks to my friends from different and diverse research groups in the Jackson School of Geosciences at UT Austin. They have made my life much happier and easier!

Interaction between Aerosols and the Mesoscale Convective Systems over the Tropical Continents

Sudip Chakraborty, Ph.D.

The University of Texas at Austin, 2016

Supervisor: Rong Fu

Abstract

Presence of aerosols in the upper troposphere can have significant impacts on the Earth's radiative energy budget. However, the aerosol–cloud relationship represents the largest uncertainty in the radiative energy budget. Relationships between aerosols and the mesoscale convective systems (MCSs) are complicated and difficult to ascertain, due in large part to inadequate availability of satellite datasets until recent years. Variation of aerosol impacts with meteorological parameters and the relative influence of these parameters on the convective strength of the MSCs can also be attributed to limited detectability of aerosol invigoration effects. To address the interaction between aerosol and the MCSs, I first address the influence of MCS on the distribution of the aerosols, which is poorly known on a global scale. Then, I investigate the influence of aerosol on MCSs. This dissertation addresses these problems by collocating a suite of geostationary and polar orbital satellites at three different phases of their convective lifecycle. First, I estimate the extent of upper

tropospheric aerosol layers (UT ALs) surrounding the MCSs and explore the relationships between UT AL extent and the morphology, location, and developmental stages of collocated MCSs in the tropics over equatorial Africa, South Asia, and the Amazon basin between June 2006 and June 2008. I identify that the most extensive UT ALs over equatorial Africa are associated with the mature MCSs, while the most extensive UT ALs over South Asia and the Amazon basin are associated with the growing MCSs. Convective aerosol transport over Amazonia is weaker than that observed over the other two regions despite similar transport frequencies, likely due to smaller sizes and shorter mean lifetimes of Amazonian MCSs. Variations in UT ALs in the vicinity of tropical MCSs are primarily explained by variations in the horizontal sizes of the associated MCSs and are not related to aerosol loading in the lower troposphere. Relationships between convective properties and aerosol transport are relatively weak during the decaying stage of convective development.

Then I estimate the relative influence of aerosols and other meteorological parameters on MCS strength and longevity using collocated samples of MCSs from January 2003 to June 2008. The results show that relative humidity (RH) and convective available potential energy (CAPE) have the strongest impacts on MCS lifetime and enhance the lifetime of the MCSs by 6-36 hours when other parameters such as vertical wind shear (VWS) and aerosols are kept constant. Aerosols also enhance the convective lifetime of MCSs, however at a much weaker rate (6-24h) and only when RH and VWS are high. Moreover, aerosol influence on convective lifetime is detected during the mature and decaying phases only. At the continental scale, aerosols explain 20-27% of

the total variance of MCSs' lifetime over equatorial South America, but explain only 8% of the same over equatorial Africa. South Asian MCSs are more strongly influenced by meteorological parameters and MCS-associated aerosols when they are over the ocean than when over the land since most MCSs form and develop over the oceans.

After that, I estimate the influence of aerosols and other meteorological parameters on MCSs' rain rate (RR). Results show that an increase in aerosol concentration enhance IWC and suppress RR and LH during all three phases of convective lifetime. Increasing aerosol concentrations suppress RR at the rate of -0.38 mm/h and -0.47 mm/h during the growing, decaying phases when VWS is high and at a rate of -0.30 mm/h during the mature phase when RH is low. Meteorological parameters such as VWS and RH have significant effects on these aerosol influences. The suppression of RR is also associated with a decrease in latent heat released by large hydrometeors. Aerosols explain 16%, 23%, and 29% of RR's variance during the growing, mature and decaying phases, respectively, as estimated by a multiple linear regression method. Consequently, aerosols enhance IWC of the MCSs inside the anvil up to 0.72, 1.41, 0.82 mg/m^3 and enhance the total integrated reflectivity of the larger-sized ice particles up to 8, 11, and 18 dBZ in the convective core regions during the growing, mature and decaying phases, respectively. In contrast, changes (one standard deviation) in CAPE and RH enhance the RR up to 0.35 mm/h.

This dissertation study provides the first satellite based global tropical assessment of the relative influences of aerosols and meteorological conditions on MCSs' lifetime, rain rate, and IWC and the mutual dependence of these

influences. It also shows how aerosols influence the rain rate, cloud ice and lifetime of the MCSs, varying within their lifecycle and between different tropical continents ranging from humid equatorial South America during wet season and big monsoonal systems over South Asia to relatively dry equatorial Africa with high aerosol loading. In doing so, this work has also advanced our capability to evaluate whether or not aerosols could increase convective lifetime by suppressing rain rate and invigorating the MCSs on climate scale and what are the favorable meteorological conditions for aerosol to affect the lifetime of the MCSs. Our results also provide an interpretive framework for devising and evaluating numerical model experiments that can examine relationships between convective properties and ALs transported in the upper troposphere. In the future, we would like to investigate the influence of different meteorological parameters and aerosols on extra tropical MCSs and on self-aggregation of convection.

.

Table of Contents

List of Tables

List of Figures

Chapter 1

General Introduction

Aerosols are very small particles, found as either solids or liquids that form from both natural and anthropogenic sources. Natural sources include generation of mineral dust aerosols due to wind erosion of land surfaces, biogenic emissions, and wildfires. Anthropogenic sources include vehicles, as well as factory emissions and agricultural burning. Emission of aerosols, especially due to anthropogenic effects, is increasing at the global scale due to fossil fuel burning and extensive changes in land use patterns by humans for agriculture [*Ramanathan et al.*, 2001].

Aerosols are ubiquitous; satellite and in-situ measurements indicate increasing aerosol concentrations over diverse regions, especially the tropics [*Ackerman et al.*, 2000; *Charlson et al.*, 1992; *Ichoku et al.*, 2003; *Kaufman et al.*, 2002; *Ramanathan et al.*, 2001]. Geographically, natural and anthropogenic aerosols are very common over equatorial Africa, equatorial South America, and South Asian regions [*Crutzen and Andreae*, 1990; *Huang et al.*, 2012; *Huang et al.*, 2013; *Ito et al.*, 2007]; however, aerosols can also be transported over long distances [*Glaccum and Prospero*, 1980; *Muller et al.*, 2005; *Prospero*, 1996]. The presence of aerosols has also been detected in the stratosphere [*Hofmann*, 1990; *Myhre et al.*, 2004; *Solomon et al.*, 2011] and tropical tropopause [*Vernier et al.*, 2011].

Because of their extensive geographical distribution, aerosols can have significant impacts on global climate in the troposphere and stratosphere. The impacts of aerosols are mainly the reflection and absorption of incoming solar radiation (direct effects) and the invigoration of clouds by suppressing precipitation (indirect effects, also Twomey effects). The direct effect of aerosols warms the atmosphere due to absorption of solar radiation by black carbon or soot particles [*Satheesh and Ramanathan*, 2000]. Impacts due to the indirect effect of aerosols are mainly seen in changes in cloud microphysics, dynamic structure, and longevity. The 5th assessment report of the Inter-governmental Panel on Climate Change (IPCC) notes that clouds and aerosols still contribute the largest uncertainty in both the sign and magnitude of the Earth's energy budget, especially in climate models where such uncertainties are even larger than in observations.

Aerosols are also widely distributed vertically throughout the atmosphere; *Vernier et al* [2011] used satellite datasets to detect persistent aerosol layers in the tropical tropopause layer (TTL), whereas *Solomon et al.* [2011] detected similar layers in the stratosphere. This vertical distribution plays a role in shaping weather and climate; for example, aerosols in the upper troposphere can have a profound impact on cirrus cloud formation [*Froyd et al.*, 2009; *A P Khain et al.*, 2008] and lead to an increase in water vapor concentration in the stratosphere [*S Sherwood*, 2002]. Moreover, aerosol impacts on the radiative budget depend on both surface radiative properties and the vertical location of aerosols relative to clouds [*Keil and Haywood*, 2003; *McComiskey and*

Feingold, 2008; *Satheesh and Ramanathan*, 2000]. As a result, aerosols can alter the Earth's radiative budget as a result of their location in the middle and upper troposphere and stratosphere. Despite the fact that aerosols have been detected at high altitudes and can have significant impacts on the global radiation budget, relatively little research has addressed the issue of aerosol transport in the context of deep convection, especially the mesoscale convective systems (MCSs).

The role of the MCSs need to be investigated on vertical transport of aerosols because the MCSs are very large in size (>100km) and their cloud top reaches between 12-18 km above sea level. The mass of the planetary boundary layer is circulated by deep convective clouds ~90 times [*W. R. Cotton et al.*, 1995] per year. These systems are vigorous and can transport aerosols along with water vapor though the convective core and detrain in the upper troposphere and lower stratosphere (UTLS). Evidence of water vapor transport by these "tropical pipes" has already been documented [*Fu et al.*, 2006], and recent studies show that transport pathways of carbon monoxide (CO), a gas phase precursor of aerosols to the UTLS, includes direct or indirect contribution from the MCSs [*Huang et al.*, 2014; *Huang et al.*, 2012]. Thus, studying the influence of the convective strength of MCSs on the transport of aerosol particles to the UTLS is very important for climate science. So far, observational studies are mostly based on a few incidences of deep convective clouds, especially pyro-convective clouds from in-situ measurements from field campaigns [*Andreae et al.*, 2004]. As a result, the role of the MCSs on aerosol transport is still not clear at global scales.

Moreover, the MCSs over equatorial Africa are the deepest and most intensive in nature, whereas the MCSs over the South Asia are part of world's

largest monsoonal circulation pattern. Convective systems over equatorial South America are shallower but more frequent in nature. Additionally, the aerosol concentrations and type are different over these three regions [*S M Fan et al.*, 2004; *Huang et al.*, 2013]. Due to differences in the convective nature of the MCSs and aerosol concentrations over these three different regions, transport of aerosols to the UTLS may also vary.

Apart from the impact of transported aerosols to the UTLS on Earth's radiative energy balance, the influence of aerosols on MCS microphysics and dynamic structure may be even more important for global climate. For example, *Rosenfeld et al.* [2008] hypothesized that aerosols can have significant impacts on global droughts and floods because of their role in delaying or suppressing precipitation and enhancing cloud longevity.

Cloud droplets or cloud condensation nuclei (CCN) form on aerosol particles. For a given amount of water vapor, enhanced aerosol concentration increases the number of CCNs and decreases their effective radii [*Rosenfeld and Woodley*, 2000]. As a result, the formation process of larger size hydrometeors by coalescence and coagulation of CCNs slows down [*Gunn and Phillips*, 1957; *Twomey*, 1977] and precipitation is delayed. This leads to an enhanced moisture supply through cloud updrafts, providing excess latent heat release inside the clouds and increasing cloud buoyancy. Consequently, cloud water content increases, clouds often reach higher altitudes [*Koren et al.*, 2010a], and cloud size increases. This leads to the possibility of an increase in a cloud's lifetime due to enhanced moisture and reduced precipitation. However, whether such impacts of aerosols can also enhance MCS strength and longevity is still not clear even

three decades after probable impacts of aerosols on cloud's lifetime was first coined by *Albrecht* [1989].

Several observations using satellite datasets and model simulations have pointed out such effects of aerosols on clouds, especially on shallow clouds [*H L Jiang et al.*, 2006]. However, clear evidence of such impacts on deep convective clouds, especially on the MCSs, are largely unavailable and are often ambiguous. Many studies have observed evidence of precipitation suppression [*A Khain and Pokrovsky*, 2004; *A Khain et al.*, 2004; *Rosenfeld*, 1999; 2000; *Rosenfeld and Lensky*, 1998], impacts on cloud microphysics [*Tulet et al.*, 2010], an increase in anvil water content [*de Boer et al.*, 2010], longevity [*Bister and Kulmala*, 2011; *de Boer et al.*, 2010; *Tulet et al.*, 2010], higher cloud top height [*Koren et al.*, 2010a], and cumulus formation [*X W Li et al.*, 2013]. Conversely, there are many studies that have observed precipitation enhancement [*A Khain et al.*, 2005; *A P Khain et al.*, 2008; *Z Q Li et al.*, 2011; *Lin et al.*, 2006; *van den Heever et al.*, 2006; *R Y Zhang et al.*, 2007] and the presence of larger ice particles inside the anvil [*Chylek et al.*, 2006]. Meanwhile, *Tao et al.* [2012] suggest that aerosols may not have any significant influence on heavily precipitating systems. Several reasons exist for these ambiguities. *Stevens and Feingold* [2009] point out that low resolution models overestimate aerosol impacts on clouds compared to cloud resolving models. They also postulate that whether aerosols can delay or suppress rainfall and intensify convection in general remains unclear due to the lack of observational evidence. However, the use of observational datasets to untangle the relationship between aerosols and the MCSs is still difficult because of the influence of meteorological parameters. The fifth assessment report of the IPCC

notes that the determination of aerosol–cloud interactions based on satellite datasets is sensitive to the treatment of meteorological influences. This is because different meteorological parameters, such as convective available potential energy (CAPE) [*R. A. Houze*, 2004; *Mapes*, 1993], relative humidity (RH) [*Del Genio and Wu*, 2010; *R. A. Houze*, 2004; *Langhans et al.*, 2015], and vertical wind shear (VWS) [*R. A. Houze*, 2004; *Kingsmill and Houze*, 1999; *Moncrieff*, 1978; *Petersen et al.*, 2006; *Weisman and Rotunno*, 2004] can influence MCS strength. Moreover, these meteorological parameters can also influence the distribution and impacts of aerosols [*J W Fan et al.*, 2007; *J W Fan et al.*, 2009] on the MCSs; *Rosenfeld et al.* [2014a] point out that aerosol invigoration is more detectable at cloud and regional scales than at large scales due to large-scale variation of such effects with meteorological conditions.

Another important factor behind the lack of understanding may be the absence of lifecycle analyses of the MCSs while addressing aerosol impacts on them. Aerosol-related MCS influence may be different at different stages of MCSs' lifecycles [*Rosenfeld et al.*, 2008]. Moreover, convective strength, RR, and interactions of MCSs with the environment can also vary at different phases of the convective lifecycle [*Machado et al.*, 1998]. Hence, ambiguities at large scales may be better resolved through statistical analyses using large samples of the MCSs and relative properties of relevant meteorological parameters and aerosol concentrations at different phases of convective lifecycle over different regions of the world.

With the advancement of satellites, information on MCS dynamic structure, RR and aerosols have become available over diverse geographical regions across the world. For example, CloudSat, on board the A-Train satellite constellation, measures larger-sized ice particles and smaller-sized hydrometeors. Aura Microwave Limb Sounder (MLS), on the other hand, can observe small ice particles inside the anvil. The Cloud-Aerosol Lidar and Infrared Pathfinder Satellite Observation (CALIPSO), meanwhile, can observe the thin cirrus anvil and cloud top height. CALIPSO also monitors the vertical profiles of aerosols, whereas the Ozone Monitoring Instrument (OMI) on board the Aura satellite measures the Aerosol Index (AI). Moderate Resolution Imaging Spectroradiometer (MODIS) on board the Aqua satellite can measure aerosol optical depth (AOD). These instruments are all part of the A-Train constellation [*L'Ecuyer and Jiang*, 2010] and take measurements at maximum intervals of 15 minutes. As a result, detailed information about the convective dynamic structure and associated aerosol properties can be obtained for the same MCSs. Despite expansive global coverage, the A-train satellites take measurements just twice a day over the same location; hence, variation of the dynamic structure of convections cannot be adequately obtained by these polar-orbiting satellites. However, geostationary satellites of the International Satellite Cloud Climatology Projects (ISCCPs) can provide observations of many key aspects of convective dynamic structure throughout the life cycles of convective systems [*Machado et al.*, 1998] at intervals of 3 hours. We have therefore developed a method here to collocate different polar-orbital and geostationary satellite datasets to obtain a large number of MCS samples with information about their convective dynamic

structure and surrounding aerosol concentrations. For RR and latent heat (LH) profiles, we use measurements from the Tropical Rainfall Measuring Mission (TRMM) datasets. This dissertation aims to assess the relative influence of aerosols, CAPE, RH, and VWS on MCSs over equatorial Africa, equatorial South America, and the south Asian regions using these multiyear satellite datasets with statistical analysis at different phases of convective lifecycle. The following chapters refer to different manuscripts either published or in review to assess different aspects of aerosol-MCS relationships including aerosol transport, aerosol impacts on cloud dynamic structure, rain rates, and cloud longevity.

In Chapter 2, I present my results that investigate the extent of aerosol layers (ALs) in the middle-upper troposphere (UT) surrounding the MCSs and explore the relationship of ALs with the morphology of the MCSs over the tropics. Detection of aerosols in the UT and the variation of these aerosols highlights the importance of understanding aerosol transport mechanisms by the MCSs, especially at times when CALIPSO detects higher amounts of aerosol pixels near the MCSs as compared to background conditions. We note, however, that the physical mechanism of aerosol transport with the strength of the MCSs and aerosol concentration at the boundary layer (BL) is poorly understood and empirical relationships between them are still unavailable. Moreover, convective strength of the MCSs vary at different phases of lifecycle, which may also influence the amount of aerosols transported above the lower troposphere. We have used the collocated A-Train and geostationary ISCCP-DX datasets between June 2006 to June 2008 to investigate the relationships between MCSs' number

of convective cores, their size and convective fraction (CF) with the total number of pixels detected at different phases of their lifecycle. The results from this study have already been published in the *Journal of Geophysical Research: Atmospheres*.

Chapter 3 aims to understand the effect of aerosols on convective lifetime of the MCSs over three different tropical regions as well as at three phases of convective lifecycle. Since aerosols can suppress precipitation, invigorate the MCSs and intensify their ice water content, it has been hypothesized by many researchers in the past decades that the lifetime of the MCSs will increase. However, the impacts of meteorological parameters on MCS strength must also be taken into consideration. So far, clear knowledge about the relative influence of aerosols and other meteorological parameters is not available.

ISCCP DX datasets provide information about MCS lifetimes; hence, we look at the rate of change of MCS lifetimes (in hours) due to the variation in aerosol concentrations as well as changes in meteorological conditions, such as lower tropospheric humidity (typically at 850 hPa), ambient humidity around 500 hPa, CAPE, and VWS. We use collocated samples of the MCSs from January 2003 to June 2008 for this study and compute the rate of change of MCS lifetimes at three different phases of convective lifetime as well as over three different terrestrial study regions in the tropics. The results presented in this chapter in its manuscript form have been submitted to *Proceedings of the National Academy of Sciences of the United States of America* and is currently under revision.

Chapter 4 aims to investigate the relative influence of different meteorological parameters and aerosol concentrations on MCS rain rate and ice

water content (IWC) during the growing, mature, and decaying phases. The impacts of aerosols in suppressing precipitation and increasing the IWC of the MCSs is not clear in the literature. However, evaluation of the relative influence of aerosol concentrations and meteorological parameters on MCS rain rate and IWC is important and necessary with regard to global climate. Because MCS rain rate and IWC simultaneously depend on the strength of meteorological parameters such as CAPE, RH, and VWS, we explore such relationships by collocating TRMM 2A25 surface precipitation rate datasets with the A-train and ISCCP DX datasets for the period January 2003 to June 2008. We also explore such influences on MCSs' IWCs consisting of large (from CloudSat data) and small (from Aura MLS data at 216 hPa) ice particles for the period June 2006 to June 2008 (since measurements from CloudSat are available after June 2006). The results presented in this chapter in its manuscript form will be submitted to the *Journal of Geophysical Research: Atmospheres*.

Chapter 5 summarizes the main findings and conclusions obtained from this dissertation. It also provides the scope of future studies.

Chapter 2

Relationships between convective structure and transport of aerosols to th[1]e upper troposphere deduced from satellite observations

2.1 Introduction

Atmospheric aerosols exert significant influences on the Earth's radiation balance and surface temperature [*Menon et al.*, 2002; *Twomey*, 1977]. These influences depend not only on the radiative properties of aerosols, but also on their vertical distribution [*Keil and Haywood*, 2003; *McComiskey and Feingold*, 2008; *Satheesh and Ramanathan*, 2000]. For example, aerosols in the upper troposphere (UT) may increase planetary albedo under clear sky conditions, but reduce planetary albedo when located above clouds. Aerosols in the UT typically have longer lifetime and more persistent and far-reaching radiative effects than aerosols at lower levels [*Lacis et al.*, 1992]. Increases in aerosols in the UT can influence the formation of in situ cirrus clouds [*Froyd et al.*, 2009; *A P Khain et al.*, 2008], enhance the lifetime of convective anvil clouds [*Bister and Kulmala*, 2011], and increase water vapor transport into the stratosphere by distributing the water content of ice clouds among a larger number of smaller crystals [*Bister and Kulmala*, 2011; *S Sherwood*, 2002; *Su et al.*, 2011].

[1] This article has been published as Chakraborty, S., R. Fu, J. S. Wright, and S. T. Massie (2015), Relationships between convective structure and transport of aerosols to the upper troposphere deduced from satellite observations, *J Geophys Res-Atmos*, *120*(13), 6515-6536. SC designed the research, analyzed the data, and wrote the paper. RF designed and supervised the research. JW analyzed the data and wrote the paper. SM wrote the paper.

Most previous studies of convective influences on aerosol transport to the UT have focused on the convective transport of insoluble gas-phase aerosol precursors. Convective transport of existing aerosols to the UT has been suggested by cloud resolving models [*Ekman et al.*, 2006; *J W Fan et al.*, 2009] and measurements made during field campaigns [*Andreae et al.*, 2004; *Heald et al.*, 2011; *Heese and Wiegner*, 2008; *Nakata et al.*, 2013]; however, observational evidence of large-scale convective aerosol transport was unclear until re- cent satellite measurements revealed large areas of persistent aerosol layers in the tropical tropopause layer (TTL) over the Asian monsoon region [*Vernier et al.*, 2011]. Moreover, *Solomon et al.* [2011] showed that background stratospheric aerosol loading has increased since 2000, reducing the global radiative forcing by about 0.1 W m^{-2}. These studies highlight the potential importance of convective aerosol transport on climatic scales and raise a number of important questions. How do aerosols that reach the upper troposphere survive wet scavenging during convective transport? Is convective transport of aerosols limited to certain geographic regions or aerosol types, or does it occur on global tropical and climatological scales? What conditions favor convective transport of aerosols?

Large samples that cover a variety of different climate regimes are needed to develop a general statistical characterization of the factors that influence convective transport of aerosols. Satellite measurements can provide these samples. For example, as shown by *Vernier et al.* [2011], the Cloud-Aerosol Lidar and Infrared Pathfinder Satellite Observations (CALIPSO) instrument suite can detect aerosol layers in the UT and TTL (between 10 and 18 km altitude).

Observations from CALIPSO have also been combined with observations from the CloudSat cloud radar to infer the properties of cloud and aerosol layers [*Kato et al.*, 2011] and the distributions of stratiform and upper-level clouds [*D M Zhang et al.*, 2010]. Several studies have used measurements of carbon monoxide (CO) made by the Aura Microwave Limb Sounder (MLS) as a proxy for convective transport of aerosols generated during biomass burning [*Di Pierro et al.*, 2011; *J H Jiang et al.*, 2009; *J H Jiang et al.*, 2008; *Knippertz et al.*, 2011]. CALIPSO, CloudSat, and Aura MLS are all part of the A-Train satellite constellation [*L'Ecuyer and Jiang*, 2010].

The role of wet scavenging on aerosol concentrations in convective environments has been extensively studied using both field observations [*Martin and Pruppacher*, 1978; *Okita et al.*, 1996; *Pratt et al.*, 2010] and numerical model simulations [*Ervens et al.*, 2004; *Hoose et al.*, 2008; *Mohler et al.*, 2005]. By contrast, relatively few studies have focused on the influence of convective dynamic structure on aerosol transport to the UT. The dynamic structure of convection varies substantially on diurnal timescales and can- not be adequately described by polar-orbiting satellites such as those in the A-Train. However, geostationary satellites, such as those used in the International Satellite Cloud Climatology Projects (ISCCP) Cloud Tracking data, provide observations of a number of important parameters that either directly or indirectly describe key aspects of convective dynamic structure throughout the life cycles of convective systems [*Machado et al.*, 1998]. Here, we collocate instantaneous 3-hourly ISCCP Cloud Tracking data with CloudSat, CALIPSO, Aura MLS, and other related A-Train satellite measurements to examine variations in the influence of convective

dynamic structure on aerosol transport by both region and stage of convective development.

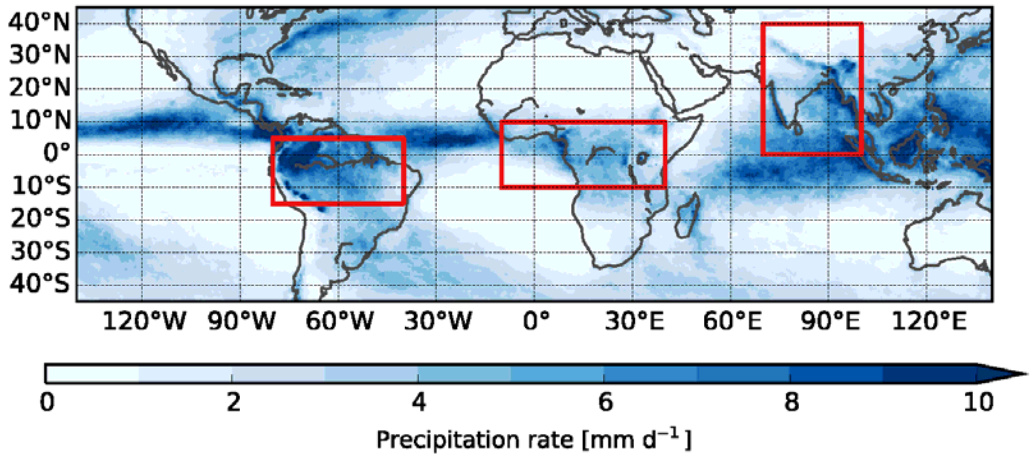

Figure 1. Definition of the analysis domains (red boxes). Shading shows mean precipitation rates (in mm d−1) during the analysis period (June 2006 to June 2008) based on the Tropical Rainfall Measuring Missing (TRMM) Multisatellite Precipitation Analysis (TMPA).

We focus on MCSs over three tropical regions (Fig. 1): equatorial Africa (10°S–10°N; 10°W–40°E), South Asia (0°–40°N, 70°–100°E), and the Amazon basin (15°S–5°N; 40°W–80°W). This approach allows us to examine upper tropospheric aerosol layers over three important tropical sources of aerosol pollution with substantially different convective regimes [*Petersen and Rutledge*, 2001]. Aerosols from biomass and fossil fuel burning, dusts, and different types of sulfate, nitrate, and ammonium aerosols are predominant over these regions [*Chung and Ramanathan*, 2004; *S M Fan et al.*, 2004; *Huang et al.*, 2013]. Mesoscale convective systems (MCSs) over equatorial Africa are prototypical of tropical continental convective systems, and contain some of the deepest and most intense convection in the world. MCSs over South Asia and the Amazon

basin are generally shallower and less intense than MCSs over equatorial Africa, and share many characteristics in common with convection over tropical oceans. We restrict our analysis of MCSs over South Asia to the peak monsoon rainy season (June–August); these rainy season MCSs typically have longer lifetimes and greater horizontal extents than MCSs over the Amazon basin.

2.2. Data and Methodology

We use a suite of several satellite data sets to describe the properties of MCSs and detect the existence and extent of aerosol and pollution layers in the nearby atmosphere. Table 1 lists key properties of the data sets and information regarding data access. This section presents an overview of our approach (Section 2.1), the sources, limitations, and uncertainties of the data sets (Section 2.2), our approach to collocating and analyzing the data (2.3), and the methodology used to construct statistical models of the data (2.4).

2.2.1. Identification and description of clouds and aerosol layers

Although satellites cannot directly measure the dynamic properties of MCSs (such as vertical velocity, mass flux, and vorticity), they are able to measure many physical properties of clouds that are related to these dynamic properties. The International Satellite Cloud Climatology Project (ISCCP) has produced data that tracks a suite of convective morphological properties at three-hourly resolution, including the number of convective cores (NCC), the convective fraction (CF), and the radius associated with observed convective systems [*Machado et al.*, 1998]. A typical MCS contains a stratiform part and a convective core part, the ratio of the latter to the total cloud area is called the convective

fraction (CF). NCCs within the convective part act as a pathway for the updraft that contains water vapor, aerosols, and many other gases to the top of the convection. NCCs are identified by their high reflectivities caused by heavy rainfall. Observations of ice water content (IWC) data from CloudSat are used to infer the height of the detrainment layer (HDL) [*Mullendore et al.*, 2009]. CloudSat also provides an estimate of cloud top height (CTH); however, CloudSat is primarily sensitive to larger hydrometeors and cannot detect the relatively small ice particles in cirrus anvils near the top of tropical convective storms. We therefore estimate CTH using measurements from the Cloud-Aerosol Lidar and Infrared Pathfinder Satellite Observation (CALIPSO) satellite [*Winker et al.*, 2009], which, like CloudSat, is part of the A-Train satellite constellation [*L'Ecuyer and Jiang*, 2010]. The Aura Microwave Limb Sounder (MLS), which is also part of the A-Train, provides measurements of IWC in upper troposphere that complement CALIPSO and CloudSat observations of convective anvil clouds [*Wu et al.*, 2008]. Precipitation rates are a fundamental measure of convective intensity and can influence the wet scavenging of aerosols; we use gridded estimates of precipitation rate from the Tropical Rainfall Measuring Mission (TRMM) Multi-satellite Precipitation Analysis (TMPA) [*Huffman et al.*, 2007], which are provided at the same temporal resolution (and approximately the same spatial resolution) as ISCCP data. In addition to cloud physical properties, environmental properties such as vertical wind shear (VWS) can play an important role in cloud formation, storm development, and convective aerosol transport [*R. A. Houze*, 2004; *Kingsmill and Houze*, 1999; *Moncrieff*, 1978; *Thorpe et al.*, 1982; *Weisman and Rotunno*, 2004]. We derive VWS using data from the

Modern-Era Retrospective-analysis for Research and Applications (MERRA) [*Rienecker et al.*, 2011], provided MERRA successfully detects the observed convective event.

It is difficult to detect aerosol layers in the vicinity of convection. We therefore use three complementary sets of aerosol measurements made by instruments in the A-Train satellite constellation. Our analysis of aerosol transport is based primarily on CALIPSO observations, validated and supplemented by observations from the Ozone Monitoring Instrument (OMI) onboard the Aura satellite and the Moderate Resolution Imaging Spectroradiometer (MODIS) onboard the Aqua satellite. CALIPSO provides high-vertical resolution profiles of aerosols along a narrow swath, and is sensitive to thin layers of aerosols above clouds and above the boundary layer. By contrast, MODIS provides observations of column-integrated aerosol optical depth (AOD) over a wide swath. These measurements are dominated by aerosol loading in the boundary layer. OMI uses observations of ultra- violet radiation to measure aerosol index (AI) and reflectivity. Because its instrumental wavelength is much smaller than cloud droplets or ice particles, OMI can be used to observe aerosol layers above clouds.

2.2.2. Data

The core of our analysis is the ISCCP DX data set. These data include cloud properties that have been derived from ISCCP B3 infrared and visible radiances, and are provided every 3 hours between July 1983 and December 2009 at 30 km spatial resolution. Measurement uncertainties are approximately ±2% for

infrared wavelengths and ±5% for visible wavelengths. Cloud identification in the ISCCP DX dataset is based on brightness temperature and visible reflectance [*Machado et al.*, 1998]. Once identified, MCSs are tracked by matching 28 different parameters at three-hourly intervals within $5^\circ \times 5^\circ$ *domains* [see *Machado et al.*, 1998, for details]. Only MCSs with radii greater than 100 km and lifetimes longer than 6 h are considered. We use ISCCP DX data to identify the time of origin and track the evolution of MCSs over three regions in the tropics. We focus on variations in location, radius, NCC, CF, and stage of storm development. MCSs can undergo several cycles of growth and decay as they propagate through different locations, with related changes in convective dynamic structure. The developmental stage of an MCS is calculated from the continuity equation by estimating the areal time rate of expansion ratio:

$$\mathrm{AE} = \frac{1}{\mathrm{A}}\left(\frac{\mathrm{dA}}{\mathrm{dt}}\right) \quad (1)$$

where A is the area of the convective system [*Machado et al.*, 1998]. Large positive values of AE (AE > 0.1) are associated with the growing stage of the convective life cycle, whereas large negative values (AE < −0.1) are associated with the decaying stage. Values of AE associated with mature MCSs are close to 0 ($-0.1 \leq \mathrm{AE} \leq 0.1$).

The primary CloudSat instrument is a 94 GHz nadir-pointing cloud profiling radar (CPR), which measures radar backscatter from clouds as a function of distance from the instrument [*Stephens et al.*, 2002]. Where possible, we use Level 2 (along-track) Cloud Water Content-Radar Only (2B-CWC-RO) profiles of cloud water content (CWC) to determine the HDL of MCSs observed by

ISCCP. Convective detrainment occurs when the convective air mass loses buoyancy. This loss of buoyancy leads to vertical convergence of IWC, which is balanced by horizontal divergence. The convective detrainment layer is therefore linked to a local increase in IWC [*Mullendore et al.*, 2009]. We estimate the rate of change of CloudSat IWC with respect to height (∂IWC$/\partial z$), and define the base of the detrainment layer as the peak in positive ∂IWC$/\partial z$ and the top of the detrainment layer as the peak in negative ∂IWC$/\partial z$. The HDL is then defined as the center of this layer.

CloudSat profiles of CWC are provided in 125 vertical bins with a vertical resolution of 240 m. The horizontal footprint is 1.4 km×1.7 km (across track × along-track), with samples collected at 1.1 km intervals along the orbit. Liquid and ice water content are retrieved using an algorithm that combines active remote sensing data with a priori data via both forward and backward models. 2B-CWC-RO retrievals may fail in regions of high reflectivity (indicating strong precipitation); however, our focus is on IWC near the top of the cloud, where precipitation rates are generally low. The retrieval algorithm assumes a constant ice crystal density; this assumption allows for the introduction of a correction factor based on the complex refraction index of ice particles. We limit our analysis to IWC data for which the quality flag is set to zero, indicating measurements that are of good quality and suitable for scientific research.

The primary instrument in the CALIPSO suite is the Cloud-Aerosol Lidar with Orthogonal Polarization (CALIOP) [*Winker et al.*, 2009]. We use Level 2 Version 3-01 Vertical Feature Mask (VFM) data, which includes both cloud and aerosol products at 0.33–5 km horizontal resolution and 30–180 m vertical

resolution. The CALIOP transmits laser signals simultaneously at two wavelengths (532 nm and 1064 nm) with a pulse repetition rate of 20.16 Hz. The receiver measures backscatter intensity at 1064 nm and two orthogonally

Table 1. Specifications for Data Sets Used in This Paper, Including Observation or Model Platform, Product Identifier, Version, Resolution (H: Horizontal, V: Vertical, and T: Time), and Data Source[a]

Platform	Identifier	Version	Resolution	Source
Aura MLS	IWC, CO	v3.3 L2	(H) ~300 km ×7 km (V) ~3 km	GES DISC[b]
CALIPSO	CAL_LID_L2_VFM	v3.01 L2	(H) ~0.33 – 5 km (V) ~60 – 180 m	LARC ADSC[c]
CloudSat	2B-CWC-RO	R04 L2	(H) 2.5 km (V) 250 m	CS DPC[d]
ISCCP	Convection	DX L3	(H) 30 km × 30 km (T) 3-hourly	GISS[e]
MERRA	MAI6NPANA	v1, stream 3	(H) 0.5∘ × 0.67∘ (V) 42 pressure (T) 6-hourly	GES DISC
MERRA	MAI3CPASM	v1, stream 3	(H) 1.25∘ × 1.25∘ (V) 42 pressure (T) 3-hourly	GES DISC
MODIS	MYD04-L2	v5 L2 v5 L3	(H) 10 km×10 km (T) daily	LAADS[f]
OMI	OMAERUV	v3 L2 v7 L3	(H) 13 km × 24 km (T) 3-hourly	GES DISC

[a] All but MERRA are based on satellite observations.

[b] Goddard Earth Sciences Data and Information Services Center (http://disc.sci.gsfc.nasa.gov).

[c] Langley Atmospheric Science Data Center (https://www-calipso.larc.nasa.gov).

[d] CloudSat Data Processing Center (http://www.cloudsat.cira.colostate.edu).

[e] Goddard Institute for Space Studies (http://isccp.giss.nasa.gov).

[f] Level 1 and Atmosphere Archive and Distribution System (http://ladsweb.nascom.nasa.gov).

polarized components at 532 nm. Misclassification of aerosols and clouds can occur due to a variety of reasons, including differences in aerosol type (such as dense smoke or dust), proximity of the aerosols to the edge of the cloud, the presence of optically thin clouds, and many more scenarios [*Z Y Liu et al.*, 2009]. We limit ambiguity between clouds and aerosols by considering only those measurements with high cloud–aerosol discrimination (CAD) scores (absolute value > 70) [*Z Y Liu et al.*, 2004; *Z Y Liu et al.*, 2009; *Omar et al.*, 2009]. CALIPSO CAD scores indicate the confidence in cloud–aerosol discrimination, and are based on five parameters: layer-mean attenuated backscatter at 532 nm, layer-mean attenuated backscatter color ratio, layer-mean volume depolarization ratio, altitude, and latitude [*Z Y Liu et al.*, 2009]. Negative values (–100 to 0) are associated with aerosols and positive values (0 to 100) are associated with clouds. CALIPSO Version 3 has been validated by several previous studies [*Kacenelenbogen et al.*, 2011; *Koffi et al.*, 2012; *Redemann et al.*, 2012], and the use of CAD score has been shown to provide a reliable discrimination between clouds and aerosols with a classification error of only 2.01% [*J J Liu et al.*, 2014]. CALIPSO is unable to detect aerosols when the aerosol backscatter signal is less than the instrument sensitivity of $2 - 4 \times 10^{-4}$ km^{-1} sr^{-1}.

We use precipitation rates from Version 7 of the TMPA daily gridded precipitation product [*Huffman et al.*, 2007]. These data are based on

observations from several satellites and rain gauge networks, and are provided every three hours at 0.25° × 0.25° spatial resolution between 50°S and 50°N.

We derive VWS from MERRA data as the difference between the mean horizontal wind speed (/**v**/) in the 925–850 hPa layer and the mean wind speed in the 250–200 hPa layer, divided by the difference in mean geopotential height (z) between the two layers [*Petersen et al.*, 2006]:

$$\mathrm{VWS} \equiv \frac{\partial |\mathbf{v}|}{\partial z} \approx \frac{\langle |\mathbf{v}|_{\mathrm{LT}} \rangle - \langle |\mathbf{v}|_{\mathrm{UT}} \rangle}{\langle z_{\mathrm{LT}} \rangle - \langle z_{\mathrm{UT}} \rangle} \tag{2}$$

where *(x)* indicates the layer mean of quantity x. We use six-hourly reanalysis winds at 0.67◦ × 0.5◦ horizontal resolution for ISCCP observations at 00, 06, 12, and 18 UTC, supplemented by three-hourly forecast winds at 1.25◦ × 1.25◦ horizontal resolution for ISCCP observations at 03, 09, 15, and 21 UTC. The reanalysis winds include data assimilation; the forecast winds are products of the forecast model alone. Both products are reported on 42 vertical pressure levels. We use MERRA analyses of vertical pressure velocity (ω) and IWC (in-between 500-100 hPa) to verify that MERRA successfully represents the occurrence of the collocated convective event.

OMI measures backscatter radiance between 270 nm and 500 nm, and provides daytime observations of clouds, aerosol layers, and surface UV irradiance. The OMI footprint is 13×24 km. We use OMI aerosol index (AI) to validate upper tropospheric aerosol layers detected by CALIPSO in the vicinity of MCSs during the daytime. AI is based upon differences in observed and model radiance ratios and detects the presence of UV- absorbing aerosols in regions where ozone absorption is very small [*Torres et al.*, 2012].

MODIS observes AOD in clear sky conditions across a swath approximately 2300 km wide, which allows us to assess the environmental aerosol loading in the vicinity of an MCS. We use AOD at 550 nm from Aqua MODIS (as opposed to Terra MODIS) because the Aqua satellite is part of the A-Train, so that Aqua MODIS observes approximately the same locations as CALIPSO, CloudSat, and MLS at approximately the same time. Like OMI, MODIS AOD is only available for the daytime. We use two MODIS products: the Level 2 MYD04-L2 data and the Level 3 MYD08-D3 daily gridded product. The former allows us to characterize environmental aerosol loading during the convective time frame for daytime events only, while the latter provides a measure of environmental AOD in the region where the convection took place. MYD04-L2 aggregates observed aerosol concentrations and optical properties into 10 km×10 km pixels. MYD08-D3 further aggregates these observations into a global $1^\circ \times 1^\circ$ *grid* on a daily basis. AOD in both datasets is based on observations using MODIS channels 1 through 7 and 20 (of 36 visible and infrared channels).

Several previous studies have indicated that MODIS AOD observations are reliable over land regions [*Levy et al.*, 2010]and have evaluated the associated uncertainties [*Chu et al.*, 2003; *Chu et al.*, 2002; *Remer et al.*, 2005]. We only consider MCSs with polluted pixels located nearby, where polluted pixels are defined as pixels with AOD greater than 0.3 [*J Lee et al.*, 2012; *Livingston et al.*, 2014]. AOD measurements near clouds can be highly uncertain [*Tackett and Di Girolamo*, 2009; *Varnai and Marshak*, 2009], both because of signal degradation due to clouds and because AOD varies due to spatial heterogeneity in relative humidity in the vicinity of clouds. To limit these uncertainties, we evaluate the

presence or absence of polluted air within a radial distance of 2° *from* the cloud boundary (where the latter is based on ISCCP data).

We supplement the above data with Version 3.3 MLS retrievals of IWC and CO. This version of the MLS data accounts for contamination of CO by Milky Way core galaxy radiation, flagging contaminated retrievals as bad data [*Pumphrey et al.*, 2009]. We analyze MLS retrievals of CO and IWC between 216 and 83 hPa in the vicinity of the detected MCSs. This pressure range is within the valid range for both CO and IWC. IWC retrievals are filtered to remove profiles for which the status flag of the MLS temperature retrieval is odd. We then apply the '$2\sigma - 3\sigma$' screening process suggested by [*Livesey et al.*, 2013] to limit the effects of spectroscopic and calibration uncertainties. This process has the effect of removing IWC retrievals that are less than three standard deviations above the mean in 10° latitude bands. Other potential uncertainties in IWC include the effects of gravity waves originating in the wintertime stratosphere; however, these uncertainties are most pronounced over mid-to-high latitudes during wintertime, whereas our analysis focuses on the tropics. MLS CO retrievals are filtered to remove profiles for which the status flag is even, the convergence flag is greater than 1.4, the quality flag is less than 1.1 (0.2 at 83 hPa), or the retrieved IWC at 147 hPa is greater than or equal to 8 mg m−3. We also eliminate CO retrievals for which either the precision or the retrieved value is less than zero.

2.2.3. Collocation criteria

ISCCP, TRMM, and MERRA data are provided every three hours, while CloudSat, CALIPSO, Aqua MODIS, OMI, and Aura MLS are provided along the

orbits of their respective satellites. A-Train satellites orbit the earth sixteen times per day, with equator- crossing times at approximately 01:30 and 13:30 local time. The regions we consider are located in the tropics, so that A-Train observation times approximately correspond to A-Train equator-crossing times.

We initially collocate the ISCCP convective tracking data with CloudSat 2B-CWC-RO profiles based on time (within ±1 h) and location (within the radius of the storm). We start by checking whether the CloudSat orbit passed through an MCS detected by ISCCP. We then check to see whether MODIS observed aerosols within a 2° radial distance from the outer boundary of the MCS, since we intend to examine the factors that control convective aerosol transport from the lower troposphere to the UT within MCSs. During nighttime, we use CALIPSO data set to ensure the presence of aerosols below 4 km altitude within a range of 2◦ radial distance from the outer boundary of the MCS. If the MCS occurred within a polluted environment, we use CALIPSO to characterize the aerosol profiles surrounding the MCS. We identify possible convective transport of aerosols by selecting mesoscale convective systems (detected by ISCCP and CloudSat) that occurred in a polluted environment (detected by MODIS and CALIPSO) with aerosol layers in both the lower troposphere and the upper troposphere (detected by CALIPSO). We then examine the evolution of the MCS before and after collocation to determine whether it was observed during a growing, mature, or decaying stage. We use gridded data from TMPA and MERRA to determine the precipitation rate and VWS associated with each MCS. As both MERRA and TMPA are available at 3-hourly intervals, we calculate precipitation rate and VWS by averaging all data within the estimated (circular) area of the

cloud indicated by ISCCP (defined by the center and the radius). We use Aura MLS IWC to supplement observations of deep convection and Aura MLS CO to supplement observations of aerosol transport [*Jiang et al.*, 2008].

We validate the upper tropospheric aerosol layers detected by CALIPSO using OMI (see below), and the lower tropospheric aerosol layers using MODIS. This validation is limited to daytime MCSs, because MODIS and OMI are only able to observe aerosols during the day. This limitation restricts the total number of collocated samples to 963 (353 growing MCSs, 400 mature MCSs, and 210 decaying MCSs). OMI is able to distinguish between absorbing and non-absorbing aerosols: positive values of AI indicate the presence of absorbing aerosols (such as dust or smoke), while near-zero or negative values indicate the presence of non-absorbing aerosols or cloud particles. An OMI measurement with AI close to 1 and a reflectivity greater than about 0.15 likely indicates a cloud–aerosol mixture, while a measurement with AI larger than 1 and reflectivity larger than 0.25 likely indicates aerosols above clouds (Dr. Omar Torres, personal communication, 3 October 2011). 79% of collocated OMI and CALIPSO measurements in the vicinity of convective anvils agree regarding the presence (or absence) of aerosols at the cloud top.

Torres et al. [2012] used simultaneous measurements from A-Train satellites (specifically CALIPSO, MODIS, and OMI) to detect the properties of aerosol and cloud layers over the southern Atlantic Ocean. They used large values of AI measured by OMI to identify the presence of aerosol layers above clouds, and CALIPSO measurements at 532 nm to deduce information about the vertical profile of aerosols and clouds. CALIPSO consistently confirmed the

presence of enhanced aerosol layers above clouds observed by OMI. They further used MODIS true color images to determine the horizontal extent of the observed clouds. The success of their study and others [*Yu et al.*, 2012] shows that approximately simultaneous measurements made by satellites (such as the A-Train satellites, which follow each other at a maximum interval of ⍰15 minutes) can be used to describe the collective properties of cloud and aerosol layers. Moreover, measurements from additional satellite instruments provide independent support and validation of the core data sets we use in this study.

Figure 2 shows an example of A-Train satellite measurements collocated with an MCS identified and tracked using ISCCP data. The ISCCP data provide the location of the center and the radius of the system every three hours (Fig. 2a). This MCS was first observed over the southern Amazon (16.7◦S, 57.3◦W) at 21 UTC on 20 January 2007. The MCS moved west as it developed, where it intersected with the A-Train tracks at approximately 06 UTC on 21 January 2007, when the MCS was in a growing stage (AE = 0.36). The radius of the system grew from 158 km at 03 UTC to 228 km at 06 UTC. According to collocated TMPA data, the mean precipitation rate at this time was 0.69 mm h^{-1}. CALIPSO and CloudSat passed over the eastern side of the MCS as it moved westward at 05:27 UTC, and Aura MLS passed over just west of the center of the system at 05:35 UTC. The convection began to decay after 09 UTC, eventually disappearing after 15 UTC on 21 January 2007. It was only observed by the A-Train satellites once.

Figure 2b shows profiles of IWC and increases in CO relative to background concentrations (calculated as the mean clear-sky CO observed within 1000 km of the system on 21 January 2007) retrieved by Aura MLS during

the overpass of this system. Large values of IWC were observed both within the system and immediately to its north, with a maximum value of 43 mg m^{-3}. Large positive CO anomalies above the storm indicate that polluted air was transported to the upper troposphere, particularly near the geographic center of the system. Figure 2c shows observations of cloud and aerosol layers made by Cloud- Sat and CALIPSO as they passed over the system. The CALIPSO measurements show both extensive anvil layers and aerosol layers in the upper troposphere, approximately 10–12 km above the surface on either sides of the MCS in-between 10°S and 22°S. The vertical cloud layer at 10°S is detected with low or no confidence by the CAD algorithm and is termed as false determination. However, the columnar layer of aerosols detected at 9°S is not a false determination and indicates a real aerosol feature. CloudSat profiled the vertical structure of the central part of the cloud system, which CALIPSO was partially unable to detect due to attenuation in the lidar signal. Large values of CWC (indicative of NCCs) were observed within the system, particularly near its northern edge.

CloudSat and CALIPSO observations collected during overpasses that passed close to the center of an MCS can be used to verify the size and location of the same MCS reported by ISCCP. Cloud sizes based on CALIPSO observations of anvil clouds are slightly greater than those reported by ISCCP, while cloud sizes based on CloudSat observations are slightly less than those reported by ISCCP. These differences can be explained by differences in the sensitivities of these instruments to small ice particles and optically thin clouds. The central location of MCSs based on CloudSat is within ±1° of the center reported by ISCCP. Differences in the central location could be attributable to horizontal

propagation of the storm during the time gap between when it is observed by ISCCP and when it is observed by the A-Train satellites.

The occurrence of convective aerosol transport is inferred from changes in the vertical distribution of aerosol pixels relative to expected background values. The background profile of aerosol pixels is derived by averaging all clear-sky CALIPSO data over one month in a $1^\circ \times 1^\circ$ grid box with a vertical resolution of 1 km between the surface and 20 km altitude. Aerosol pixel counts near convection are defined as the number of aerosol pixels along the satellite track within $\pm 2^\circ$ (222 km) of the boundary of the MCS along the satellite track, but not within the system itself. Aerosol pixel counts are thus calculated along the same horizontal length on both sides of every system, regardless of its size. The background profile from the grid cell containing the MCS is subtracted from the number of aerosol pixels observed in the vicinity of the convection at each altitude. The differences are then binned in 2 km vertical increments. For example, the change in the number of aerosol pixels at 9 km altitude is defined as the sum of differences between the observed and background profiles in the 8–9 km and 9–10 km layers. This procedure mitigates uncertainties associated with horizontal advection of aerosols into the vicinity of the MCS. The vertical distributions of convective detrainment height based on CloudSat IWC (Fig. 3) and MERRA vertical velocity (not shown) also support the hypothesis that the detected aerosol layers are primarily transported to the UT by the collocated convective systems. The number of background aerosol pixels is very low above 4 km altitude, consistent with previous results based on CALIPSO [*Huang et al.*, 2013] and Department of Energy Atmospheric Radiation Measurement (ARM)

observations *[Turner et al., 2001]*. The detected aerosols are unlikely to be freshly nucleated, as previous studies indicate that only a small number of nucleation mode aerosols reach the convective anvil [*Ekman et al.*, 2006]. Hence, we use the vertically integrated extent of the convective aerosol layers (ALs), defined as the total number of aerosol pixels between 4 and 20 km within a range of 2° radial distance from the outer boundary of the MCS, to explore the influence of convective dynamic properties on aerosol transport.

Due to laser attenuation, CALIPSO can only observe aerosols near the periphery of the cloud systems; it cannot detect aerosols inside clouds with substantial water content (see, e.g., Fig. 2c). Our analysis is therefore based on aerosol profiles detected on the periphery of MCSs, either above or beneath the stratiform portions of the system. Aqua MODIS and OMI are completely unable to detect aerosol layers underneath clouds. These instruments are not suitable for detecting aerosols when the CWC is large.

We use MERRA data to provide a meteorological context for each MCS, including the grid-scale vertical pressure velocity (ω) and the vertical wind shear (VWS) in the area surrounding the convection. The occurrence of convection in MERRA matches well with the occurrence of convection observed by the A-Train satellites. MERRA simulates strong negative values of ω (indicative of upward motion) and detects IWC in-between 500-100 hPa (indicative of presence of a system extending from mid altitudes to anvil level) in 98% of the collocated cases. We eliminate the other 2% of cases from the analysis.

Our study includes a total of 963 MCSs (systems with lifetimes more than 6 hours) over equatorial Africa, South Asia, and the Amazon basin between June

2006 and June 2008. We restrict our analysis of MCSs over South Asia to systems that occurred during the peak monsoon months (June–August 2006, June–August 2007, and June 2008). The 963 identified systems include 353 growing MCSs, 400 mature MCSs, and 210 decaying MCSs. We also briefly examine 111 short-lived convective systems (systems with lifetimes less than 6 hours) over the Amazon basin.

Our collocation methodology (Section 2.3) contains several potential sources of random error, such as measurement uncertainties and differences in the part of the MCS observed by the A-Train satellite instruments (e.g., edge versus center, convective versus stratiform parts of the MCS, etc.). To mitigate the effects of these random errors, we aggregate each sample into 50 bins of approximately equal size according to the observed aerosol layer extent and perform the regression using the mean values in each bin. For example, the full sample of 963 MCSs is separated into 50 bins, each containing between 19 and 20 MCSs. Missing data are masked and excluded from the mean value in each bin.

2.2.4. Statistical model construction

The statistical models we consider here are based on multiple linear regression, in which the dependent variable (or output) is modeled as a linear combination of the independent variables (or predictors):

$$y_i = \beta_0 + \sum_{j=1}^{p} \beta_j x_{ij}, \quad (3)$$

where β_0 is the intercept and β_j , $j \in [1, p]$ is the coefficient associated with the j^{th} of p predictors. In our analysis, the dependent variable y_i is the aerosol layer

extent, defined as the aerosol pixel count relative to the local background aerosol pixel count based on CALIPSO observations. This variable can be either negative (indicating dilution of the upper tropospheric background aerosol layer) or positive (indicating aerosol transport). The independent variables x_{ij} include the radius, number of convective cores (NCC), and convective fraction (CF) observed from ISCCP data, the cloud top height (CTH) from CALIPSO, the vertical wind shear (VWS) from MERRA, the precipitation rate from TRMM, and the aerosol optical depth (AOD) from MODIS (i.e., $p = 7$).We standardize all predictors so that they have a mean of zero and a variance of one.

Traditional linear regression selects the coefficients $\hat{\beta}$ that minimize the residual sum of sum of squares;

$$\sum_{i=1}^{N}\left(y_i - \beta_0 - \sum_{j=1}^{p}\beta_j x_{ij}\right)^2. \quad (4)$$

This approach is unsuited to coefficient determination and variable selection for modeling physical systems like deep convection, for which two or more of the predictors may be tightly correlated. In particular, the coefficients for tightly correlated predictors may be large, with opposite signs that cause compensation in the model. To mitigate this effect, we apply the elastic net method for coefficient shrinkage [*Zou and Hastie*, 2005]. This method applies a penalty on the size of the coefficients. The coefficients $\hat{\beta}$ are then determined by minimizing the penalized residual sum of squares

$\sum_{j=1}^{p} |\beta j|$ is often referred to as the $L1$ prior (used in Lasso regression) and the penalty $\sum_{j=1}^{p} |\beta 2j|$ is referred to as L2 prior (used in ridge regression).

$$\sum_{i=1}^{N}\left(y_i - \beta_0 - \sum_{j=1}^{p}\beta_j x_{ij}\right)^2 + 0.5\alpha\sum_{j=1}^{p}|\beta_j| + 0.25\alpha\sum_{j=1}^{p}\beta_j^2. \quad (5)$$

Our goal is to identify the subset of predictors that best explain variability in the dependent variable. We therefore use recursive feature elimination to identify subsets of independent variables that maximize the explained variance in the sample. It eliminates the redundant or irrelevant independent variables that make no useful contribution in predicting the dependent variable. We are then left with seven subsets with sizes of one to seven, where the subset of size one includes the single predictor that maximizes the explained variance, the subset of size two includes the pair of predictors that maximizes the explained variance, and so on. The subset of size seven includes all seven predictors.

We apply a random five-fold cross-validation to train and test the models using optimal subsets of various size. Specifically, we randomly divide the sample into five approximately equal bins. We then use 80% of the data to construct a statistical model based on each optimal subset of size one to seven, and then test the model using the remaining 20% of the data. This approach is applied recursively, so that each 20% is used as test data. We repeat this random five-fold cross-validation process 100 times, so that 500 models are trained and tested. We then calculate the coefficients $\beta\hat{}$ as the average coefficients over those 500 models. Repeating this process generally results in identical coefficients to three significant digits.

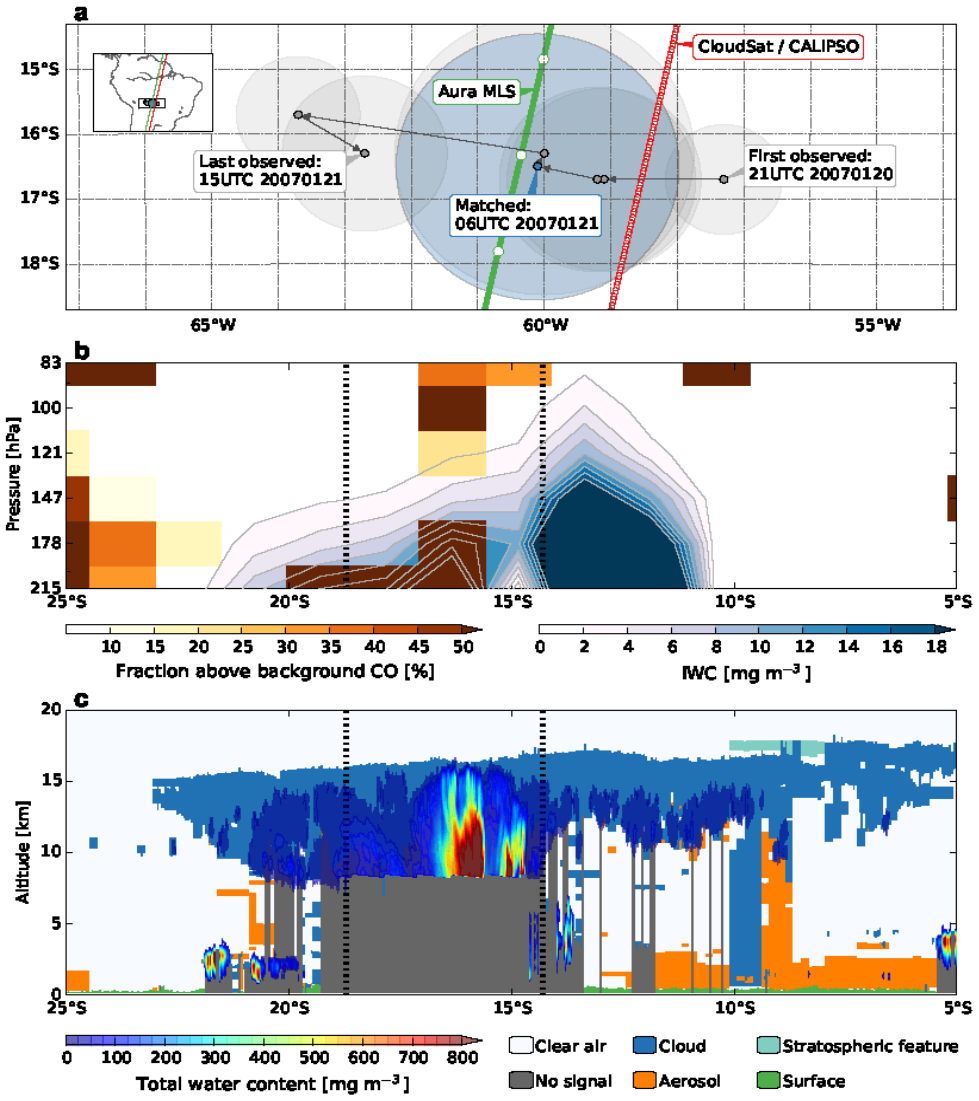

Figure 2. An example of a collocated MCS, including (a) the origin and development of the MCS, (b) the vertical distribution of IWC and fractional CO anomalies in the upper troposphere along the MLS track, and (c) the vertical distribution of aerosol and cloud layers along the CALIPSO and CloudSat track. This MCS was first detected by ISCCP at 21 UTC 20 January 2007 at 16.7◦S and 57.3◦W. The system then moved west, where the A-Train satellites observed it at approximately 06 UTC 21 January. The dark and light blue circles in Figure 2a show the approximate central position and radius of the MCS at the A-Train overpass time. The cloud was growing when CALIPSO and CloudSat (red line) observed its trailing edge at 05:27 UTC and Aura MLS (green line) observed the system near its center at 05:35 UTC. The central positions of each satellite footprint are shown as white circles along the satellite track.

The optimal model is chosen by identifying the subset of independent variables that minimizes the mean squared error in the test data. Choosing a model that is too simple (i.e., including too few predictors) will underfit the training data, with errors in the test data dominated by large biases. Choosing a model that is too complex (i.e., including too many predictors) will overfit the training data, with errors in the test data dominated by large variance. Using this procedure, we are able to construct statistical learning models that strike a balance between maximizing explained variance (via recursive feature elimination) and minimizing mean squared error (via cross-validation).

2.3 Results

In principle, aerosols can be transported to the UT by either long-range transport or by local convective transport. The slopes of isentropic surfaces, sedimentation, and vertical motion driven by diabatic heating can all influence the height of an aerosol layer, so that the vertical distribution of aerosol layers is unlikely to remain constant during long-range transport. By contrast, the vertical locations of aerosol layers recently transported to the UT by local convective transport are likely to match the vertical locations of the associated convective detrainment layers. Figure 3 shows the distributions of aerosol layer height (HAL), cloud detrainment height (HDL), and cloud top height (CTH) for all MCSs detected by ISCCP with aerosol layers in the upper troposphere. The vertical distribution of aerosol layers observed in the vicinity of convection is very similar to the vertical distribution of convective detrainment heights. This

similarity supports the hypothesis that local convective transport dominates the formation of UT aerosol layers in the vicinity of convective systems, and suggests that joint application of CALIPSO and CloudSat is a reasonable approach to detecting convectively-generated aerosol layers.

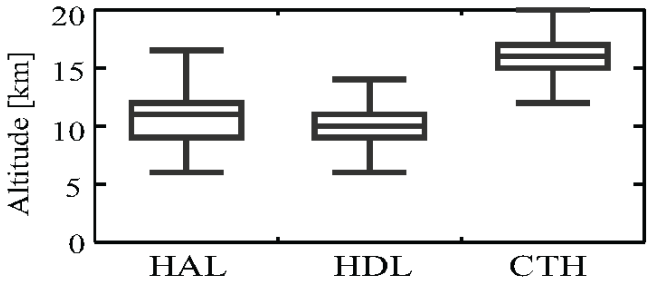

Figure 3. Box and whisker plots showing the distributions of the height of the aerosol layer (HAL), the height of maximum convective detrainment (HDL), and the cloud top height (CTH) for collocated MCSs. The bottom and top of each box represent the upper and lower quartiles, respectively, and the horizontal line inside the box represents the median. The ends of the whiskers are the minimum and maximum of the data. MCSs with HAL < 6 km (the minimum observed detrainment layer) have been excluded.

The cloud top heights detected by CALIPSO are located several kilometers above the convective detrainment layers, likely due to the sensitivity of the CALIPSO lidar to smaller ice particles and relatively thin cirrus clouds. The sensitivity of the lidar enables us in detecting CTHs more accurately than CloudSat. These clouds may be associated with overshooting convection or local in situ condensation due to convectively-generated gravity waves.

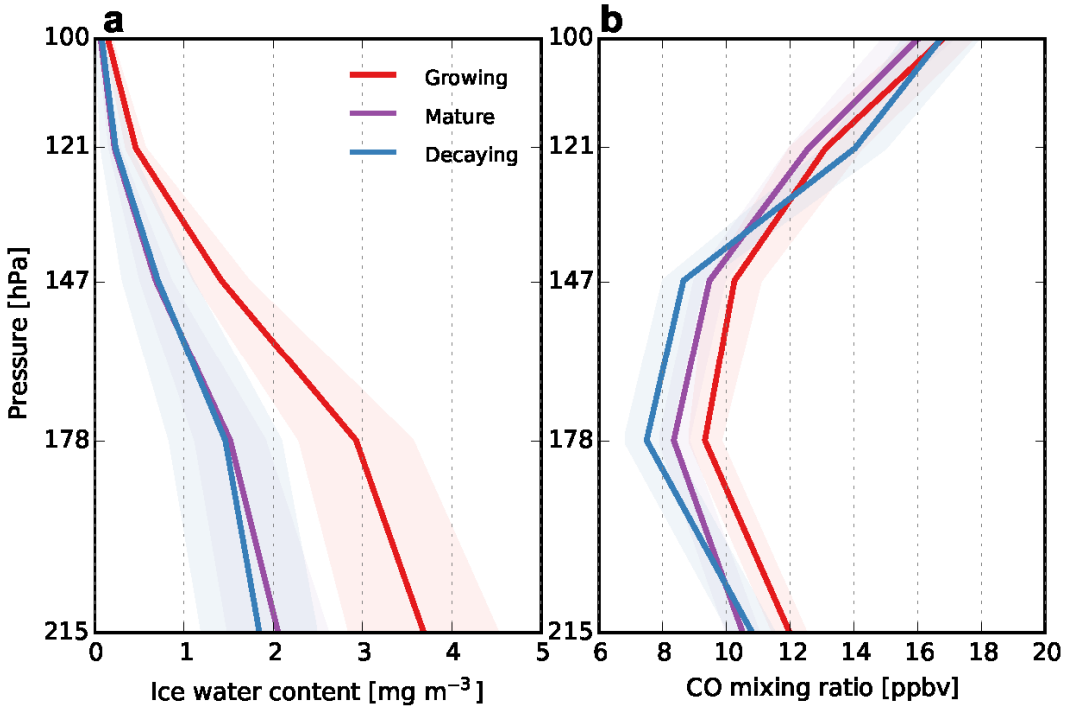

Figure 4. Mean profiles of (a) IWC and (b) CO in the upper troposphere based on Aura MLS profiles collocated with growing (red), mature (purple), and decaying (blue) MCSs. Shading represents intervals of one standard error around the mean.

Figure 4 shows variations in IWC and CO in the upper troposphere during different stages of convective development. Both IWC and CO tend to be larger during the growing stage than during the mature or decaying stages. This result indicates that convection is typically deepest and most intense during the growing stage, with stronger transport of near-surface air to the UT.

This hypothesis is further supported by Fig. 5, which shows variations in aerosol transport and convective properties during different stages of the convective life cycle. The vertically-integrated extent of the convective aerosol

layer (i.e., the total number of aerosol pixels surrounding the MCSs between 4 and 20 km relative to

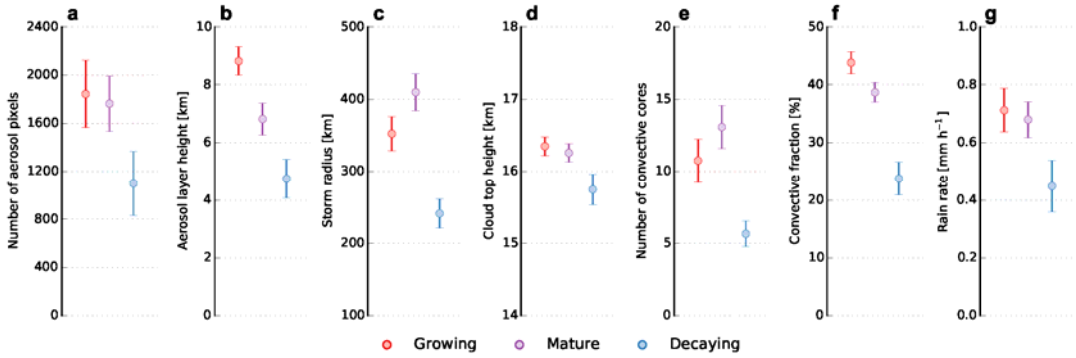

Figure 5. Variations in mean values of (a) vertically integrated anomaly in number of aerosol pixels, (b) aerosol layer height (HAL), (c) storm radius, (d) cloud top height (CTH), (e) number of convective cores (NCC), (f) convective fraction (CF), and (g) precipitation rate during different stages of the convective life cycle. Error bars and shading represent intervals of two standard errors around the mean.

background values) is significantly larger during the growing and mature stages of convection than during the decaying stage. Likewise, the mean height of the aerosol layer is significantly higher during the growing stage (8.8±0.5 km) than during the mature stage (6.8±0.6 km), and significantly higher during the mature stage than during the decaying stage (4.7±0.7 km). These variations in the height and extent of aerosol layers may be attributed to differences in the intensity and extent of convection. The intensity of convection is highest during the growing stage, as indicated by larger mean values of CTH, CF, and rain rate. Mature convective events are nearly as intense (differences in the mean values of CF and rain rate are not significant between growing and mature events), and are also

more extensive (as indicated by larger mean values of radius and NCC). The mean values of all variables are significantly lower for decaying MCSs than for growing or mature MCSs.

Figure 6 shows profiles of the magnitude and frequency of convective aerosol transport over the equatorial Africa, South Asia, and Amazon regions. The magnitude of convective aerosol transport is inferred by subtracting a local clear-sky background profile from profiles of aerosol pixels observed within ±222 km of the boundary of the MCS along the satellite track (but not within the boundary of the MCS; see Section 2.3 for details). This metric can be thought of as the extent of the convective aerosol layer in a given altitude range. The magnitude of aerosol transport is bimodal, particularly over equatorial Africa and South Asia, with peaks in the middle troposphere (approximately 5 km altitude) and upper troposphere (approximately 9–11 km altitude). This distribution of aerosol changes is consistent with the vertical profile of convective detrainment, and indicates that convective influences on aerosol concentrations are strongest at the levels where mid-level congestus and deep convective clouds detrain. The extent and frequency of convective aerosol layers are largest during the mature stage over equatorial Africa and during the growing stage over South Asia. Over the Amazon, the frequency and mean extent of convective aerosol layers are substantially larger during the growing stage than during the mature or decaying stages. The frequency of convective aerosol layers over the Amazon during the growing stage is comparable to the frequencies of convective aerosol layers over equatorial Africa and South Asia, but the extent of these aerosol layers is much smaller (≈50%) over the Amazon.

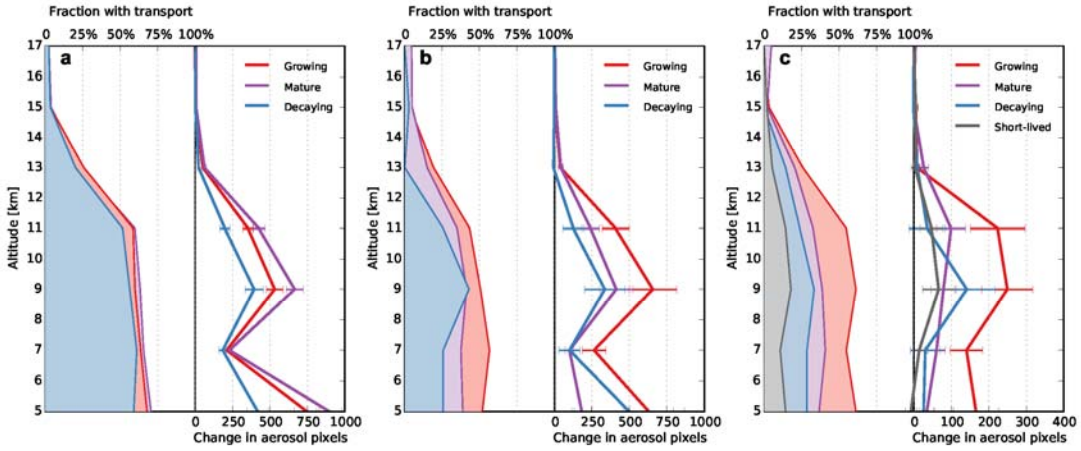

Figure 6. Vertical profiles of aerosol transport associated with growing (red), mature (purple), decaying (blue), and short-lived convective events (gray) over (a) equatorial Africa, (b) South Asia, and (c) the Amazon basin. The left side of each panel shows the vertical distribution of the fraction of convective events for which the anomaly in aerosol pixels relative to the background profile is positive. The right side of each panel shows the mean anomaly in the number of aerosol pixels at that height. The vertical resolution is 2 km. Error bars indicate intervals of one standard error around the mean.

Differences in convective aerosol transport among the three regions may also be explained by differences in convective properties. For example, mean radius and NCC peak during the mature stage over equatorial Africa and peak during the growing stage over the Amazon (not shown). This difference may explain why aerosol layers are most extensive during the mature stage over equatorial Africa but most extensive during the growing stage over the Amazon. Mean radius and NCC also peak during the mature stage over South Asia; however, differences between the growing and mature stage are much smaller

over South Asia than over equatorial Africa. Moreover, unlike over equatorial Africa, these differences are not statistically significant. Growing systems are almost as large as mature systems over South Asia (mean radius of 438.2±55.6 km relative to 499.3±57.7 km) and have nearly as many convective cores (18.6±4.8 relative to 20.5±4.6). When coupled with the greater intensity of growing MCSs relative to mature MCSs and the greater potential for mature MCSs to occur in environments with aerosol concentrations already diluted by wet scavenging, these differences provide a plausible explanation for why convective aerosol transport is strongest during the growing stage over South Asia.

The smaller mean extent of convective aerosol layers over the Amazon relative to convective aerosol layers over equatorial Africa and South Asia has several possible explanations. MCSs over the Amazon have a shorter mean lifetime (~19 h), a much smaller mean radius (~120 km), and higher mean rain rates (~1.5 mm h−1) than MCSs over equatorial Africa or South Asia. The differences in lifetime and radius are likely to reduce the area influenced by the MCSs over the Amazon relative to the larger, longer-lived systems over the other regions, while the difference in rain rate may enhance wet scavenging. Short-lived convective systems are also more common over the Amazon than over the other regions; the frequent precipitation associated with these systems may act more effectively to flush aerosols out of the atmosphere.

Our results indicate that convective aerosol transport is stronger, deeper, and more frequent during the growing and mature stages of the convective life cycle than during the decaying stage over all three analyzed regions. Although this conclusion is unsurprising given the well-known differences in convective

intensity between growing systems and decaying systems [*Machado et al.*, 1998], it provides a strong indication that our approach is able to capture variations in both convective structure and aerosol transport. We therefore use these data to construct a series of statistical models. This approach allows us to establish firmer connections between measures of convective intensity and aerosol transport, identify the most influential variables, and evaluate the potential for using these variables to predict the occurrence and extent of aerosol layers generated by convective transport in MCSs.

2.4. Statistical model results and discussion

Figure 7 shows the fraction of variance of aerosol layer extent in the full data set explained by the predictors in the optimal statistical models for MCSs in different stages of the convective life cycle (see Section 2.4 for details). Table 2 lists the associated coefficients and evaluation metrics for each model based on test data alone. Approximately 80% of the variance in UT aerosol layers (ALs) associated with all MCSs can be explained by three predictors: radius, NCC, and VWS. Likewise, approximately 58% of the variance in ALs associated with growing MCSs can be explained by two predictors (radius and VWS), approximately 75% of the variance in ALs associated with mature MCSs can be explained by three predictors (radius, NCC, and CF) and approximately 52% of the variance in ALs associated with decaying MCSs can be explained by two predictors (radius and AOD). The most influential predictor in each case is the size (radius) of the MCS.

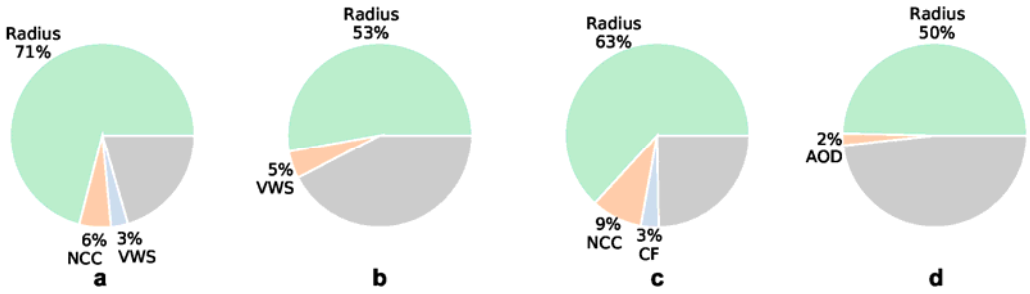

Figure 7. Fraction of variance of aerosol layer extent in the binned data explained by the independent variables in the optimal statistical models for aerosol transport associated with (a) all MCSs, (b) growing MCSs, (c) mature MCSs, and (d) decaying MCSs. Gray area shows fraction of variance not explained.

Figure 8 shows the covariation of the dependent and independent variables in the optimal statistical model for ALs associated with all MCSs. Radius and NCC are both significantly positively correlated with AL extent (R = 0.92 and R = 0.66, respectively), as well as with each other (R = 0.92). As a result, the strong positive coefficient for radius (β_{RAD} = 6.66) is compensated by a strong negative coefficient for NCC (β_{NCC} = –54.1) despite the positive single-variable correlation between NCC and AL extent. The negative dependence of AL extent on NCC is at least partially a surrogate for regional differences in the relationship between radius and AL extent. For example, mean AL extent is larger over equatorial Africa (1904 ± 169) than over South Asia (1432 ± 423) (see also intercept values for these two regions in Table 3), but mean radius is slightly larger over South Asia (431 ± 36 km) than over equatorial Africa (364 ±

17 km). By contrast, the mean value of NCC is almost twice as large over South Asia (17.5 ± 2.9) as over equatorial Africa (9.8 ±0.8). NCC therefore becomes a useful surrogate variable for representing the smaller mean extent of UT aerosol layers over South Asia, and its coefficient is negative despite the positive linear relationship between NCC and AL extent.

The role of VWS is more difficult to parse. VWS accounts for 3% of the variance in AL extent for all MCSs and 5% of the variance in AL extent for growing MCSs (Fig. 7). It is tempting to ascribe the negative coefficients for VWS in these models to the adverse impacts of strong VWS on convective development. However, the overall linear correlation between VWS and UT aerosol layer extent is weak, and Fig. 8 and Fig. 9 suggest a more complicated relationship. Local regression indicates a positive relationship between VWS and aerosol layer extent at smaller values of VWS ($R \approx 0.24$ for VWS ≤ 10 s−1) and a negative relationship at larger values of VWS ($R \approx -0.38$ for VWS > 10 s−1), although neither relationship is significant at the 95% confidence level ($p = 0.1$ – 0.2). Moreover, VWS is most influential over South Asia (Table 3), where it is positively correlated with AL extent ($R = 0.3$, $p = 0.03$).

VWS can be beneficial to the growth of an MCS and the transport of water vapor and aerosols from the boundary layer to the UT. The presence of VWS between low levels and upper levels produces steady storms [*Thorpe et al.*, 1982] and provides a slant-wise path for air to ascend through the system [*Houze* , 2004]. Wind shear allows updrafts to rise over cold pools formed by downdrafts at an angle between 34◦ and 76◦ [*Kingsmill and Houze* , 1999], so that large values of VWS may be associated with convective systems that contain distinct

regions of updrafts and downdrafts [*Weisman and Rotunno*, 2004]. Slantwise ascent and separation of updraft and downdraft regions both favor aerosol transport through the convective cores, because they allow the aerosols to bypass scavenging in downdrafts. Moreover, cold pool formation and layer overturning are associated with enhanced storm propagation, which is a function of stability and shear of the environment [*Moncrieff* ,1978]. Storms subject to stronger VWS may therefore be more likely to sample locations in which lower tropospheric aerosols have not yet been scavenged by earlier precipitation.

Table 2. Coefficients for background-relative aerosol pixel counts between 4 and 20km in optimal statistical models by stage of convective development, along with the correlation coefficient between the expected and predicted values in the test data (R2) and the explained variance in the test data (EV).

	β_0	β_{RAD}	β_{NCC}	β_{VWS}	β_{CF}	β_{AOD}	R^2	EV
All	1690	6.66	-54.1	-44.6			0.64±0.02	69±5%
Growing	1950	5.19		-52.6			0:22±0:04	32±3%
Mature	1860	5.19	-67.4		9.8		0:62±0:02	66±2%
Decaying	1120	4.99				-745	0:09±0:05	24±3%

Table 3. Coefficients for background-relative aerosol pixel counts between 4 and 20 km in optimal statistical models by region[a].

	β_0	β_{RAD}	β_{NCC}	β_{VWS}	β_{CF}	β_{AOD}	R^2	EV
Africa	1960	5.01						
Africa (G)	2100	4.35						
Africa (M)	2350	5.39	-66.1			6.62		
Africa (D)	1300	3.96					-776	
South Asia	1632			3.65				57.5
Amazon	475	2.63	-98.2					

[a]Data for equatorial Africa is separated into different stages of the convective life cycle (G: growing; M: mature; D: decaying). Sample sizes for South Asia and the Amazon basin are too small to separate by stage of convective life cycle.

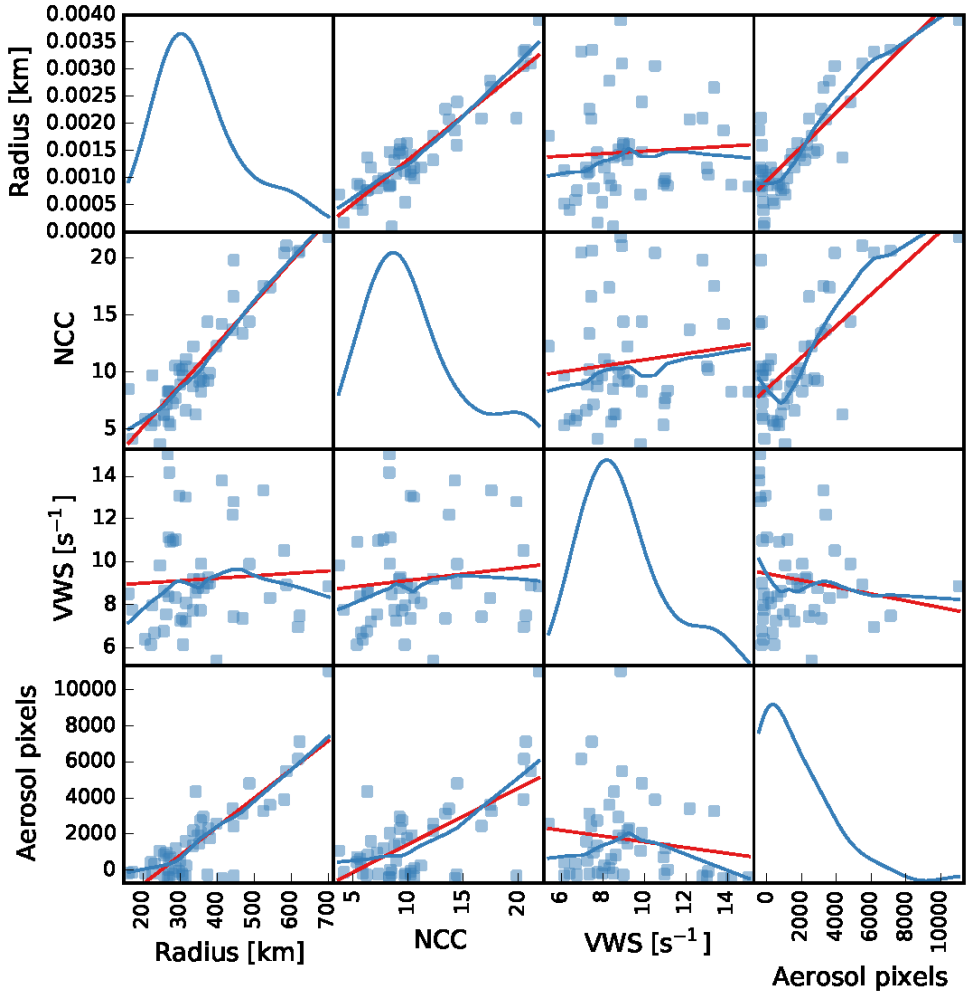

Figure 8. Scatter matrix showing co-variability among the independent variables (ordinates in first to third rows; abscissas in first to third columns) and the dependent variable (ordinate in fourth row; abscissa in fourth column) in the optimal statistical model for aerosol transport associated with all MCSs. The model-independent variables (in the order of importance) are radius, number of convective cores (NCC), and vertical wind shear (VWS). The dependent variable is the vertically integrated anomaly in aerosol pixels (see text for details). Red lines in scatterplots show linear relationships; blue lines show local linear regressions using a lowess filter. Blue curves along the diagonal show the density distributions of each variable (scale as shown in the top left ordinate).

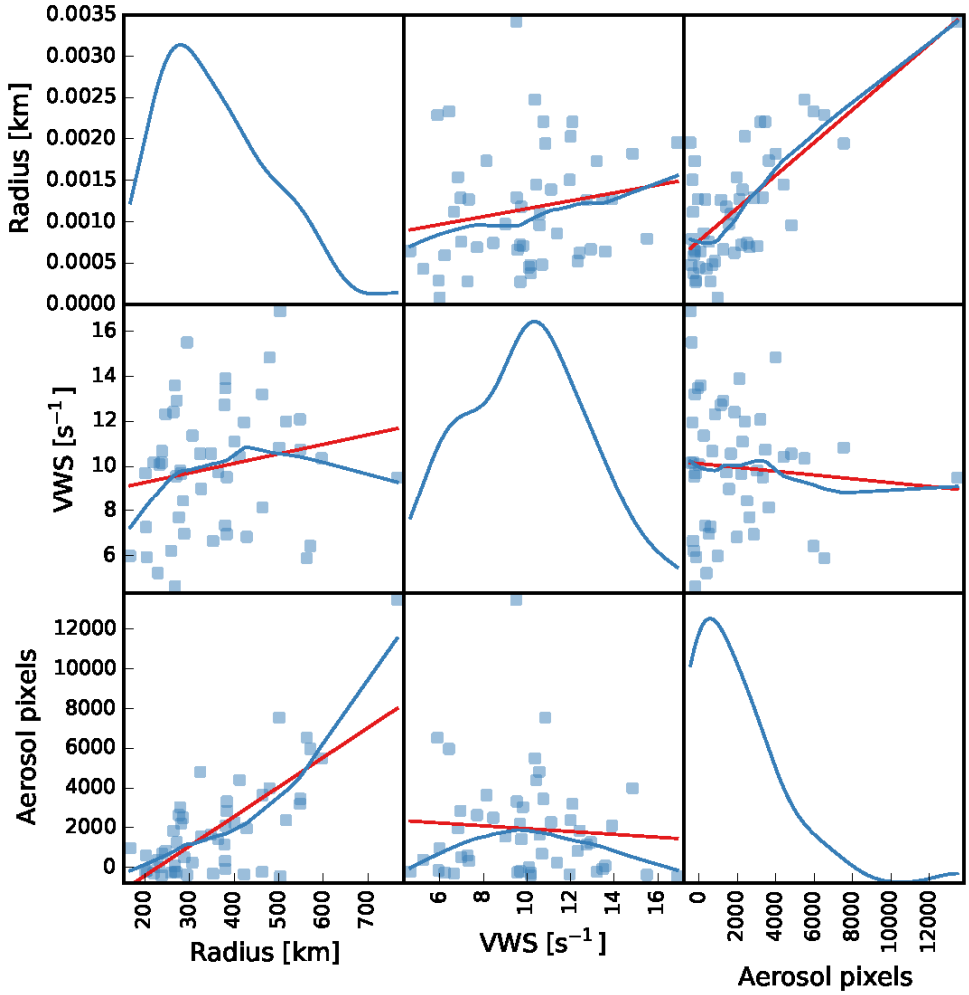

Figure 9. As in Figure 8, but for growing MCSs. The independent variables are radius and vertical wind shear (VWS).

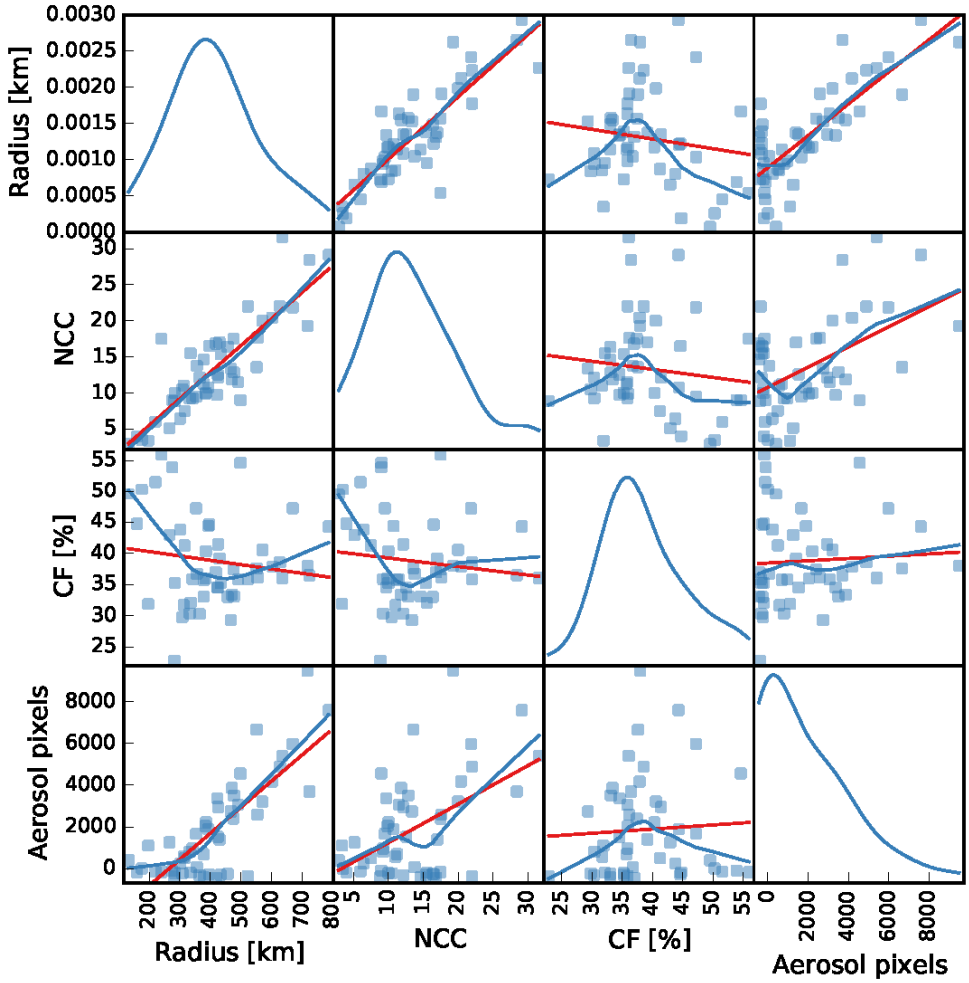

Figure 10. As in Figure 8, but for mature MCSs. The independent variables are radius, number of convective cores (NCC), and convective fraction (CF).

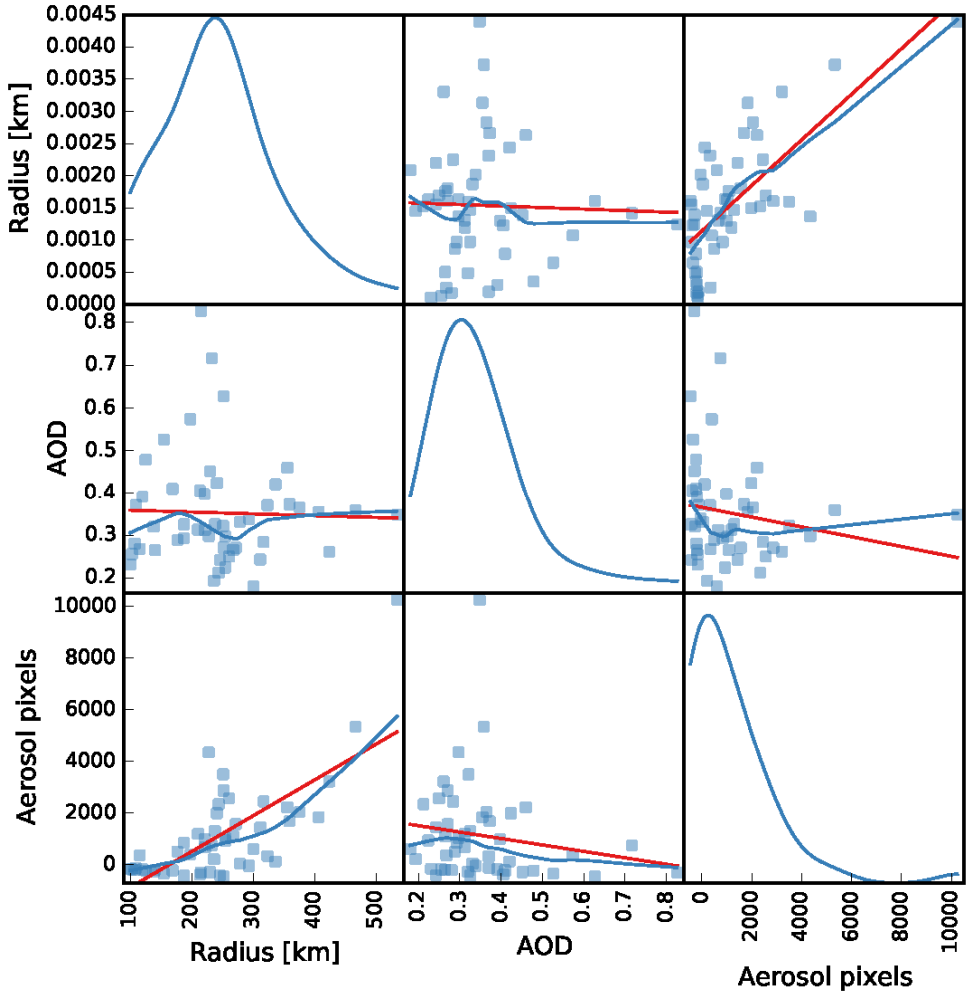

Figure 11. As in Figure 8, but for decaying MCSs. The independent variables are radius and aerosol optical depth (AOD).

We are unable to fully clarify the relationship between VWS and AL extent based on these data alone, but our results do permit some insight that could be used to develop model-based studies to further explore this relationship. First, the relationship between VWS and AL extent is strongest during the growing stage. This result is consistent with expectations: growing MCSs are strongly rooted in the boundary layer, while mature MCSs are maintained primarily by latent heating and gravity wave dynamics in the free troposphere [*Houze* , 2004] and decaying MCSs have weaker updraft speeds and fewer convective cores. Second, the relationship between VWS and UT aerosol layer extent is strongest over South Asia. Mean VWS in convective environments is approximately twice as large over South Asia ($15.4 \pm 1.1 \times 10^{-4} S^{-1}$) as over equatorial Africa ($7.5 \pm 0.5 \times 10^{-4} S^{-1}$) or the Amazon basin ($8.1 \pm 1.4 \times 10^{-4} S^{-1}$), suggesting that the relationship between VWS and UT aerosol layer extent may be more pronounced in optimal-shear environments. Finally, like NCC, the dependence of UT aerosol layer extent on VWS may be confounded by regional differences in VWS. The stronger wind shear over South Asia than over equatorial Africa, combined with the weaker dependence of AL extent on radius over South Asia relative to over equatorial Africa, may partially explain the negative values of $\hat{\beta}_{\mathrm{VWS}}$ shown in Table 2. It is also possible that the strong relationship between VWS and AL extent over South Asia represents sub-regional variability with the larger South Asia domain; however, while VWS depends strongly on latitude ($R = -0.57$), most of the MCSs are clustered within the same latitude band (10◦N–18◦N) and there is no significant relationship between latitude and AL extent.

Figure 10 shows the covariation of the dependent and independent variables in the optimal statistical model for ALs associated with mature MCSs. The primary difference between the model for mature MCSs and the model for all MCSs is that CF is flagged as important for AL extent associated with mature MCSs, particularly over equatorial Africa (Table 3). The linear relationship between CF and AL extent for mature MCSs over all regions is weak and statistically insignificant (R = 0.06, p = 0.68), but the linear relationship between CF and AL extent for mature MCSs over equatorial Africa is significant (R = 0.33, p = 0.02). The former is again likely due to regional differences (the largest values of CF are observed over the Amazon, and are associated with smaller systems and less extensive ALs), while the latter likely reflects the actual relationship between CF and AL extent during the mature stage of MCS development. This conclusion is supported by the positive value of $\hat{\beta}_{CF}$ in both cases, which indicates that, given the sa me radius, larger values of CF are associated with more extensive aerosol layers.

Figure 11 shows the covariation of the dependent and independent variables in the optimal statistical model for ALs associated with decaying MCSs. In addition to the dependence on radius, a small fraction of the variance (□2%) is explained by AOD. Surprisingly, the coefficient for AOD is negative. This may again be partially attributable to regional variability (mean AOD is significantly larger for decaying MCSs over South Asia but mean AL extent is largest for decaying MCSs over equatorial Africa); however, this negative relationship is also identified for AL extent over equatorial Africa alone (Table 3). One possibility is that larger values of AOD indicate environmental air that has experienced less

wet scavenging, and are therefore evidence of either (1) greater horizontal displacement of the MCS between its growing and mature stages (when ALs were more likely to develop in the UT) and its decaying stage, or (2) lower peak convective intensity, which could potentially reduce both convective transport and washout. Along with the weakness of relationships between AOD and AL extent in other stages of convective development, the negative relationship between AOD and AL extent during the decaying stage underscores the fundamental independence of UT aerosol layer extent relative to aerosol loading in the lower troposphere.

Figure 12 illustrates the expected variations of AL extent according to the regression models summarized in Table 2. Although the models for all MCSs and mature MCSs contain three independent variables, we have used the strong correlation between NCC and radius (NCC = 0.0483 × RAD − 6.561 for all MCSs; NCC = 0.0482 × RAD − 6.871 for mature MCSs) to illustrate them in two dimensions. Figure 12a–b shows that AL extent is expected to increase with increasing radius and decreasing VWS. Likewise, AL extent increases with increasing radius and CF during the mature stage (Fig. 12c), and increases with increasing radius and decreasing AOD during the decaying stage (Fig. 12d). The models explain much of the qualitative variance in the data, but consistently overestimate the lowest values of AL extent and consistently underestimate the highest values of AL extent. These errors may reflect nonlinear relationships that are unaccounted for in the model construction.

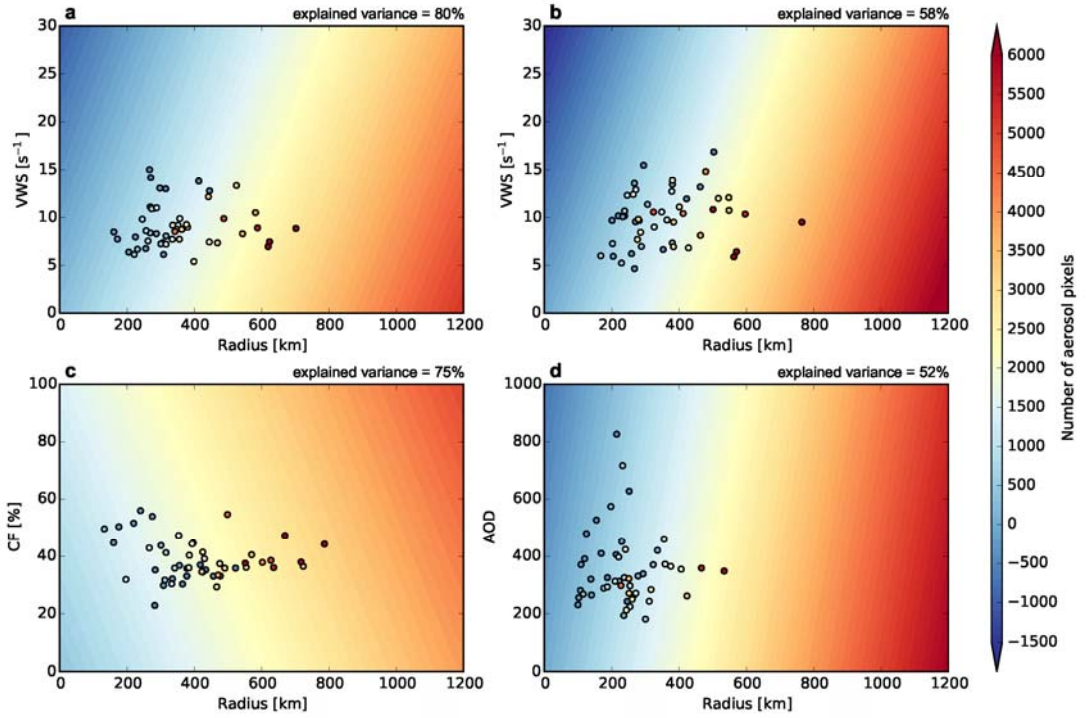

Figure 12. Graphical representations of the statistical models for (a) all MCSs, (b) growing MCSs, (c) mature MCSs, and (d) decaying MCSs. The models for all MCSs and mature MCSs have been collapsed into two dimensions by using the strong linear correlation between radius and NCC (see text and Figures 8 and 10). A scatterplot of the binned data for each case is shown for reference, and the fraction of variance explained by the linear model is shown at the top right of each panel.

2.5. Summary

The morphology and dynamic structure of MCSs is potentially critical for convective aerosol transport throughout their life cycle, yet relatively few studies have evaluated the relationships between the morphology of MCSs and aerosol transport at the scales of tropical continents. Our analysis uses multiple years of satellite data to evaluate relation- ships between convective properties and

aerosol transport to the UT over three different tropical regions and during three different stages of MCS development.

Many previous studies of aerosol transport have focused on variations in UT CO, which has been used as a surrogate for biomass burning aerosols [*Jiang et al.*, 2008]. Here, we have introduced an approach that combines ISCCP and A-Train satellite observations to explore the relationships between convective characteristics and direct observations of aerosol layers in the nearby UT. A-Train observations allow us to examine the detailed vertical structure of clouds and aerosol layers in the tropical UT, while ISCCP data provides valuable context with respect to both the large-scale environment and the stage of convective development. We focus on three stages of convective development, which have been defined according to changes in the area of the underlying MCS: the growing stage, the mature stage, and the decaying stage. Our approach yields a sample of 963 MCSs covering three tropical regions: equatorial Africa, South Asia, and the Amazon basin. This sample size is considerably larger than previous attempts to infer relationships between convective properties and aerosol transport, and allows us to develop more robust statistical models. We find that the dynamic structure of convective systems and the influence of this structure on aerosol transport vary significantly during the convective life cycle.

Although it is generally expected that the magnitude and frequency of convective aerosol transport are fundamentally tied to the strength of the convection, our analysis represents the first attempt to characterize the evolution of these relationships throughout the MCS life cycle. Aerosol transport is strongest during the growing stage of MCS development over South Asia, but

strongest during the mature stage of MCS development over equatorial Africa. These differences are attributable to a combination of (1) larger differences in convective intensity between the growing and mature stages over equatorial Africa than over South Asia and (2) the greater likelihood of diluted aerosol concentrations during the mature stage due to scavenging by earlier precipitation. Growing MCSs are almost equally as strong as mature MCSs over South Asia, but growing MCSs are considerably weaker than mature MCSs over equatorial Africa. The variation of convective aerosol transport frequency by developmental stage is qualitatively similar over all three basins, but convectively-generated ALs are considerably less extensive over the Amazon basin than over the other two regions. Rain rates are typically higher in convective systems over the Amazon than in convective systems over South Asia or equatorial Africa, which may enhance wet scavenging over the Amazon. Moreover, convective size and lifetime are considerably shorter over the Amazon than over South Asia or equatorial Africa, which may limit aerosol transport.

Our results show that much of the variability in convectively-generated UT aerosol layers (ALs) can be explained by variations in the size (radius) of the MCS. This dependence does not arise from the definition of ALs, as AL extents are calculated over the same horizontal distance along the CALIPSO track regardless of MCS size. The number of convective cores (NCC) is also identified as influential in several cases, although its coefficient in the multiple regression models is opposite in sign to its coefficient in single-variable regression. NCC is strongly correlated with radius (R = 0.92), and careful analysis suggests that the primary function of NCC in the model is to account for regional variability in the

relationship between radius and AL extent. Stronger vertical convective flux is associated with a larger number of convective cores embedded in a MCS, and the larger vertical flux leads to more aerosol being transported to the 10-12 km altitude levels.

Optimal statistical models relating convective properties to AL extent vary considerably by both region and stage of the convective life cycle. In particular, vertical wind shear (VWS) is related to AL variability during the growing stage, convective fraction (CF) is related to AL variability during the mature stage, and aerosol optical depth is related to AL variability during the decaying stage. Regional variability in several convective properties confounds physical interpretation of the statistical relationships. This confusion may be particularly important for VWS, which receives a negative coefficient when all regions are considered, but a positive coefficient when only South Asia is considered.

Our analysis indicates that VWS may play an important role in aerosol transport during the growing stage. The VWS coefficient appears to act as a surrogate for regional variability when all regions are considered together, but AL extent over South Asia increases significantly with increasing VWS (R = 0.30, p = 0.03). A positive relationship between VWS and aerosol transport is physically plausible, given the close relationship between convective and boundary layer properties during the growing stage and the potential for VWS to enhance convective aerosol transport by establishing separate regions for up-drafts and downdrafts. Our results suggest that this physical interpretation is most likely, but we are unable to conclusively rule out alternative explanations

(such as sub-regional co-variability in VWS and AL extent). A full evaluation of this hypothesis will require detailed model simulations.

Our statistical model results further indicate that mature systems with similar sizes will typically produce more extensive ALs when the CF is larger. This positive dependence on CF is only observed for mature systems. By contrast, the extent of ALs associated with decaying systems is negatively correlated with aerosol optical depth (AOD). This result is intuitively surprising, and may reflect a positive relationship between convective aerosol transport to the UT and wet scavenging in the lower troposphere over the preceding hours. We find no significant correlations between AOD and UT AL extent, although we note that our analysis is restricted to MCSs that occurred in environments that were at least somewhat polluted (i.e., at least some nearby pixels with AOD $\geq$ 0.3).

Our results provide valuable context regarding the relative importance of different convective properties over different regions and at different stages of the convective life cycle. In particular, we have identified a potentially important relationship between VWS and aerosol transport during the growing stage of convective development, and we have shown that variations in AL extent in the upper troposphere are largely independent of variations in lower-tropospheric AOD above the threshold value. These results demonstrate the potential value of ISCCP observations for developing deeper physical interpretations of the detailed profiles of cloud and aerosol properties provided by the A-Train satellites, and provide an interpretive framework for constructing and evaluating numerical model simulations of convective aerosol transport.

Chapter 3

Relative influence of the meteorological conditions and aerosols on the lifetime of the mesoscale convective systems

3.1 Introduction

The hypothesis that aerosols may delay precipitation and increase cloud lifetime of shallow marine clouds [*Albrecht*, 1989] has motivated many researchers to study the aerosol indirect effect on convective clouds; however, the influence of aerosols on enhancing cloud lifetime has remained under debate. Mesoscale convective systems (MCSs) are deep convective clouds that cover several hundred kilometers. Previous studies have shown that aerosols affect deep convection, in particular that aerosols increase the number of smaller size cloud nuclei (CCN) [*Rosenfeld and Woodley*, 2000], which weaken coagulation and coalescence that form rain droplets, and consequently delay warm rainfall [*Rosenfeld and Lensky*, 1998; *Rosenfeld et al.*, 2007]. These processes allow more cloud droplets to rise above the freezing level and increase latent heat released due to glaciation [*Rosenfeld et al.*, 2008], resulting in stronger updraft speed, enhanced cloud ice content [*Lin et al.*, 2006], larger anvil size [*Rosenfeld et al.*, 2008], and higher cloud top height [*Koren et al.*, 2005]. The top of the troposphere warms owing to the aerosol-induced changes in convective anvils [*Koren et al.*, 2010b]. Although these aerosol effects have been seen in observations from field campaigns [*Bister and Kulmala*, 2011; *Lindsey and Fromm*, 2008], they have been undetectable on large spatial and multi-year

scales. *Rosenfeld et al.* [2014b] have attributed this lack of detectability on the large scale of aerosol invigoration of convection to its variation with meteorological conditions and to the lack of knowledge of the relative humidity (RH) outside the clouds.

The variation of aerosol effects on convection with meteorological parameters has been studied previously [*Rosenfeld et al.*, 2014b]. For example, model simulation has shown that an increase in aerosol concentrations up to an optimal level can invigorate the MCSs under weak vertical wind shear (VWS) and higher relative humidity, but suppress the MCSs under strong VWS in a dry environment [*J W Fan et al.*, 2007; *J W Fan et al.*, 2009]. They found that due to a significant enhancement in the convective available potential energy (CAPE), corresponding to an increase in RH from 50% to 70%, aerosol impacts on ice crystal mass becomes pronounced with a dramatic increase in the size of the anvils and the mass of ice crystals of the deep convection. However, such impacts are negligible when RH increases from 40% to 50% due to little increase in CAPE [*J W Fan et al.*, 2007]. Moreover, consumption of CAPE for a given amount of rainfall is converted to an equal amount of kinetic energy that invigorates the convection [*Rosenfeld*, 2006; *Rosenfeld et al.*, 2008]. These studies indicate that VWS, RH, and CAPE are important factors that can influence aerosol impacts on the MCSs. However, no quantitative assessment of the relative influence of aerosols verses these meteorological parameters on convective lifetime using satellite measurements has been established [*Rosenfeld et al.*, 2014b].

The influence of aerosols on the MCSs are expected to vary in different phases of the convective life cycle. For example, *Rosenfeld et al.* [2008] hypothesized that the impact of aerosol on deep convection is stronger and more prominent during the dissipating phase. Using cloud-resolving simulations, *J W Fan et al.* [2013] found out that aerosol microphysical effects intensify the deep convection during the mature and decaying phases by forming larger number of smaller and long-lasting particles, whereas additional latent heat released due to aerosols' thermodynamic effect is responsible for invigorating the deep convections during the growing phase. Hence, the detection of aerosol impacts might may not be visible until the mature phase as no satellite can directly measure the thermodynamic properties.

Most of the above discussed studies were based on either model simulations or limited case studies from field campaigns. Observational assessments of how the influence of aerosols depend on meteorological conditions and the convective life cycle, and whether aerosols could have a significant influence on the lifetime of the MCSs at climate and large spatial scales, have not been available [*Rosenfeld et al.*, 2014b]. *Stevens and Feingold* [2009] have suggested that climate models with parameterized cloud and turbulence schemes tend to overestimate the effect of aerosols on clouds compared to the models that resolve cloud processes and large eddies. The extrapolation of the results obtained from a limited number of field campaigns to global and climate scales is questionable. Hence, whether aerosols could increase the lifetime of the MCSs on large spatial and climate scales, and if so,

how would such an effect vary with meteorological conditions and the convective life cycle, has not been clear. Detection, measurement, and retrieval of the aerosols properties from the satellite data in the vicinity of deep convective clouds at various stages of a cloud's lifecycle is challenging [*Koren et al.*, 2010a].

Isolating the impact of aerosols from other meteorological conditions observationally requires large samples of the MCSs under similar meteorological conditions and at different phases of their life cycle [*Rosenfeld et al.*, 2014b]. For this purpose, we use a suite of collocated geostationary and polar-orbital satellite measurements, along with reanalysis products, constrained by both physical principles in the atmospheric model and observations, to determine the phases of MCSs' lifecycle, lifetime, and ice water content of the MCSs and associated ambient meteorological and aerosol conditions (See Methods). We examine 2430 cases of the MCSs with co-located ISCCP convective clouds and MODIS AOD measurements to estimate changes of MCS's lifetime with aerosol as a function of changing meteorological conditions. We estimate changes in MCS's lifetime with various meteorological parameters as a function of aerosol and other meteorological parameters. We can also estimate the relative influences of aerosols and various meteorological parameters on MCS's lifetime using multiple linear regression at different stages of the convective lifecycle and over different regions.

3.2 Data and Methods

Methods

We collocate MODIS and ISCCP datasets to identify the convections that are observed by different satellites between January 2003 and June 2008, in order to have sufficient numbers of the MCSs needed for the statistical analysis used in this study. For South Asia, only monsoon months (June-September) of every year are considered. Domains of analysis, details of the collocation technique and related error estimation processes are given in Chakraborty et al. [2015]. Once a collocated MCS is observed, we compute f_{AOD} using the MODIS AOD pixels [*Koren et al.*, 2008; *J Lee et al.*, 2012; *Livingston et al.*, 2014; *Rosenfeld et al.*, 2008] within an area of 2° latitude/longitude in the vicinity of a MCS. We determine MCSs' lifetime, phase of convective life cycle, and different convective properties from the ISCCP DX dataset [*Machado et al.*, 1998], and calculate the CAPE, RH_{850}, RH_{500}, and VWS [*Petersen et al.*, 2006] from the MERRA data [*Chakraborty et al.*, 2015]. We integrate the mean vertical reflectivity profile (Z) above the freezing level to represent the columnar IWC [*Matrosov*, 2009a] or IZ. For details of the calculations and equations, please see the supporting Information. We have used multiple linear regression statistics [*Chakraborty et al.*, 2015] based on the linear combination of the predictors (CAPE, RH_{850}, RH_{500}, VWS, and f_{AOD}) to form a set of predictive equations to estimate the variance of MCS explained lifetime.

3.3 Results and Discussion

The lifetime of the MCSs is influenced by convective available potential energy [*Robert A. Houze*, 1993; *R. A. Houze*, 2004; *Mapes*, 1993], an useful measure for cloud buoyancy and vertical velocity [*William R. Cotton and Anthes*, 1989; *Edward J. Zipser*, 2003], moisture entrained from the warm atmospheric boundary layer [*William R. Cotton and Anthes*, 1989; *Robert A. Houze*, 1993; *R. A. Houze*, 2004], and lateral entrainment of free tropospheric moisture, which can dilute the buoyancy of the rising air and account for up to 33%-50% of the rainfall [*Langhans et al.*, 2015]. VWS contributes to organizing the storms, determining whether updraft and downdraft regions overlap, slantwise accent of the moist air, and precipitation [*R. A. Houze*, 2004; *Kingsmill and Houze*, 1999; *Marwitz*, 1972; *Moncrieff*, 1978; *Weisman and Rotunno*, 2004]. We evaluate the influence of both the low level VWS [*Petersen et al.*, 2006; *Weisman and Rotunno*, 2004] and the deep tropospheric VWS (see Methods). The former influences rainfall and total condensation [*Weisman and Rotunno*, 2004], whereas the latter influences vertical velocity [*Weisman and Rotunno*, 2004] and also MCS anvil formation [*Harrison*, 1992; *Kilroy et al.*, 2014; *Koren et al.*, 2010b; *Petersen et al.*, 2006; *Weisman and Rotunno*, 2004].

Past studies have shown that the response of deep convective clouds to aerosols is nonlinear. Over land, aerosol microphysical effects on deep convective clouds saturate and reverse at AOD>0.3 [*Koren et al.*, 2008]. Moderate concentrations of aerosols (or CCNs) maximize the invigoration effect of aerosols, whereas higher aerosol concentrations can reduce the vigor of the

convection [*Rosenfeld et al.*, 2008]. However, over humid land and oceans, more aerosol is required to suppress rainfall. Thus, a threshold of AOD ~0.3 is likely to be optimal as a threshold of pollution to determine the influence of aerosols on the MCSs [*J Lee et al.*, 2012; *Livingston et al.*, 2014]. We use AOD>0.15 over land and AOD>0.3 over the ocean as the threshold for a polluted environment.

To isolate the effect of aerosols on MCSs' lifetime and compare it to the effect of these primary meteorological conditions, we evaluate how the lifetime of the MCSs changes with one standard deviation (1σ) of CAPE, relative humidity at 850 hPa (~ 1.5 km above the sea level, RH_{850}), relative humidity at 500 hPa (~5.5 km above the sea level, RH_{500}), deep tropospheric vertical wind shear (VWS), and the fraction of the number of aerosol pixels with AOD (f_{AOD}) greater than 0.15 (0.3) over land (the ocean) to the total number of AOD pixels within a range of 2° latitude/longitude from the boundary of the MCSs, respectively, over all three regions (see Methods and Supporting Information). Our analysis shows that using AOD > 0.3 as a threshold for polluted environment over both land and ocean does not significantly change the influence of aerosols on MCSs' lifetime (Fig. 18). Also, the MCSs' lifetime is not significantly correlated with the lower tropospheric VWS (Fig. 17). Moreover, response of MCS lifetime to a 1σ increase in CAPE is weaker when we consider lower tropospheric VWS (Figs. 17c and 17d), compared to that under the influence of deep VWS (Fig13a). Thus, we show our results in the main body of this work using AOD>0.15 as the threshold for a polluted environment over land, and AOD>0.3 as the threshold for a polluted environment over ocean, and also show results for deep tropospheric VWS.

These above mentioned conditions are determined by the International Satellite Cloud Climatology Project convective tracking, Moderate Resolution Imaging Spectroradiometer (MODIS), and the Modern-Era Retrospective analysis for Research and Applications (MERRA) data sets. Our calculations on the global tropical continental scale indicate that MCSs' lifetime increases at the highest rates with an increase of CAPE under intermediate to high VWS values and polluted conditions. MCS's lifetime increases about 3-30 hours for an increase of CAPE by one standard deviation (1σ, Fig. 13a). The multiple linear regression (Fig. 13f) also shows that CAPE explains 33% of the total variance of MCSs' lifetime, larger than any other meteorological and aerosol conditions. RH_{850} is the second most influential parameter on MCSs' lifetime, explaining 27% of its total variance (Fig.13b). MCS's lifetime increases by 3-27 hours per 1σ increase of RH_{850} under intermediate to high VWS values and polluted conditions. The lifetime of the MCSs also increases with RH_{500} by 3-9 hours for 1σ increase of RH_{500} under polluted conditions (Fig. 13c), explaining only 4% of the total variance of MCSs' lifetime. MCSs' lifetime decreases by 6-9 hours for a 1σ increase of VWS in dry environments with low f_{AOD} values, but increases by 3–30 hours for a 1σ increase of VWS in the high RH_{850} environment. Overall, VWS explains 16% of the total variance of the lifetime of MCSs. It is the third most influential meteorological condition on MCCs' lifetime. In addition, increases in MCS lifetime with other meteorological and aerosol conditions (CAPE, RH_{850}, RH_{500} and f_{AOD}, respectively) are stronger at moderate to high level of VWS (Figures 13a, 13b, 13c, 13d, and 13e), possibly because precipitation efficiency decreases below 50% when VWS is above 20 x 10^{-4} S^{-1} [*Marwitz*, 1972], whereas

weak to moderate VWS is associated with heavy convective rainfall [*William R. Cotton and Anthes*, 1989; *Maddox et al.*, 1979].

The lifetime of MCSs appears to increase with aerosols by 3-15 hours with 1σ increase of f_{AOD} but only under high RH_{850} and moderate to high VWS (Fig. 13d). MCS's lifetime decreases with f_{AOD} under lower RH_{850} by 3-6 hours per 1σ increase of f_{AOD}. MCS*s*' lifetime increases with f_{AOD} by 3-24 hours under high values of CAPE and moderate to high values of VWS (Fig. 13e) and also decreases at low values of CAPE and VWS at the rate of 3-6 hours due to 1σ increase of f_{AOD}. Overall, f_{AOD} explains less than 1% of the total variance of MCSs' lifetime. Thus, on the scale of global tropical continents, the lifetime of the MCSs is mainly linked to meteorological conditions and dominated by the CAPE and lower tropospheric humidity, which is consistent with previous studies [*William R. Cotton and Anthes*, 1989; *Del Genio and Wu*, 2010; *R. A. Houze*, 2004; *Langhans et al.*, 2015; *Mapes*, 1993]. These results do not vary significantly for f_{AOD} using the AOD > 0.3 instead of AOD>0.15 as the threshold for polluted environment over land (Fig. 13 and Fig. 18).

However, the aerosol influence on MCSs' lifetime, cloud ice water content, and convective anvils may not become detectable by satellites until the mature or decay phases, as the available satellite sensors cannot effectively detect changes of cloud particle size change in the lower and middle troposphere inside of convection and cloud thermodynamic effects. Thus, we separately analyze the variations of MCS*s*' lifetime with ambient conditions during the growing, mature, and decay phases, respectively. Figures 14a-14c shows that CAPE dominates the

variance of MCSs' lifetime during the growing phase, explains 36% of its total variance, but become less influential during the mature and decay phases, explaining 25%, and 9% of the total variance, respectively. RH_{850} dominates the variance of MCSs' lifetime during the mature and decay phases, explaining 46% and 44% of the total variance, respectively. VWS explains about 4-34% of the total variance of the durations of these phases. The dominant influence of relative humidity and CAPE over VWS reflects mainly the large geographic variations of MCSs' lifetime with the ambient atmospheric humidity that is needed to sustain the MCSs. In comparison, aerosols explain 6% and 24% of the total variance of the mature and decay phase longevity, respectively, and do not appear to have detectable influence on the duration of the growing phase of the MCSs.

Are the empirical relationships between MCSs' lifetime and ambient meteorological and aerosol conditions shown above physically reasonable? Based on the hypothesized underlying mechanism of aerosol influence on convective lifetime, an increase in MCSs' lifetime is due to increase of cloud ice, especially in the form of smaller cloud particles above the freezing level within convective cores and anvils. Such effects may be more apparent and detectable by satellite sensors, as slower sedimentation of larger amount of smaller ice particles can sustain convective anvils for longer time. Thus, we analyze the vertically integrated cloud ice content of the MCSs (IZ, See Methods and Supporting Information) derived from CloudSat (Figs. 14d-14f) and ice water content at 216 hPa (~12 km above the sea level, IWC_216) of convective anvils

from the Aura Microwave Limb Sounder (MLS) datasets based on 966 cases of the MCSs (over the limited period of June 2006 for CloudSat to June 2008 for ISCCP-DX) with co-located ISCCP, CloudSat, and MLS measurements in Figures 14d-14i. Notice that IZ represents the mass of larger ice particles above the freezing level (above 5 km) mainly within the convective cores and lower portion of the anvils, whereas IWC_216 represents the mass of smaller particles near top of the convective anvil. Hence, their relationships with meteorological and aerosol conditions can be different.

Figures 14d shows that IZ's variance is primarily explained by RH_{850} (43%) and CAPE (39%) during the growing phase. VWS explains 12% of the total variance of the IZ (Fig. 14d). The result is broadly expected based on the controlling factors of convection reported in the literature [*William R. Cotton and Anthes*, 1989; *Robert A. Houze*, 1993; *R. A. Houze*, 2004; *Mapes*, 1993]. The variance of the cloud ice in the convective anvil (IWC_216, Fig. 14g) during the growing phase is explained mostly by CAPE, presumably because convective detrainment in the upper troposphere or anvils generally increases with buoyancy. During the mature phase, CAPE and VWS explains 57% and 14% of the total variance of the IZ, respectively (Fig. 14e), presumably because of their influence on convective mass flux above the freezing level. In contrast, RH_{850} and f_{AOD} appear to be most influential on the ice water content of the anvils, explaining 64% and 26% of its total variance, respectively, presumably because of their strong influence on the amount and effective size of smaller ice particles [*J W Fan et al.*, 2013]. During the decay phase, CAPE and f_{AOD} dominate the

variance of IZ, explaining 51% and 35% of its total variance, respectively. f_{AOD} dominates the IWC_216 variation, explaining 27% of its total variance. VWS and RH_{500} also have significant influence on IWC_216; each explaining 11% of the total variance in the decay phase. Such increasing influences of aerosols, middle tropospheric humidity and deep tropospheric vertical wind shear are also physically plausible as the MCSs at decay phase become increasingly detached from the lower troposphere.

The analysis of these independently measured variables in Fig. 14 suggests a stronger influence of aerosols on the duration of the MCSs' decay phase, probably due to the stronger influence of aerosols on cloud ice water content in both convective cores and anvils during this phase. CAPE, RH_{850}, and VWS dominate the explanation of variance of MCS's lifetime, ice water content of the convective cores and anvils during the growing and mature phases. Generally, aerosols have a stronger influence on convective anvils than on ice water content of convective cores and MCSs lifetime, presumably because of the formation of larger number of smaller ice particles [*J W Fan et al.*, 2013], which are sensitive to aerosol loading. The smaller ice particles are more likely suspended in convective anvils, and thus can influence the anvil ice water content and lifetime.

Figure 15 shows the relative influences of ambient aerosols versus meteorological conditions on MCSs' lifetime within each continent. Figure 15a shows that meteorological parameters explain approximately 92% and f_{AOD} explains up to 8% of the total variance of the lifetime of the MCSs over equatorial

Africa. Over South Asia, only 39% of the total variance of the MCSs' lifetime can be explained by meteorological and aerosol conditions when we consider all the MCSs (Fig. 19). However, we found that 45% of the MCSs formed and matured over the Indian Ocean, Bay of Bengal, and Arabian Sea (Fig. 16c). Evaluating the relationship between these MCSs when they were over the ocean and the associated ambient meteorological conditions and f_{AOD} (using AOD>0.3 as the threshold), we find that RH_{850} dominates the lifetime of these MCSs, explaining about 45% of the total variance; f_{AOD} also has an important impact, explaining ~20% of the total variance (Fig. 15b). RH_{500} and VWS explain 15% and 12% of the total variance, respectively. What causes the large fraction of the unexplainable variance of the MCSs' over Indian continent remains unclear.

The dominant MCSs' type and aerosol conditions over equatorial South America are sharply different between the wet (December to April) and dry (June to September) seasons. Thus, we separately evaluate the influences of meteorological and aerosol conditions on the MCSs for the dry or wet season. CAPE, VWS and f_{AOD} explain ~31%, ~29%, and ~20% of the total variance of MCSs' lifetime during the dry season (Fig. 15c), respectively, suggesting a comparable role between these three variables. Ambient RH_{500} also explains a significant fraction of lifetime variance, likely because the drier middle troposphere is a stronger limiting factor for the occurrence of MCSs during the dry season than in the wet season over equatorial South America [*W H Li and Fu*, 2006]. During the wet season, CAPE and f_{AOD} explain ~41% and ~22% of the total variance, respectively. The link between relative humidity and MCSs'

lifetime in South America is weaker compared to other tropical continents, presumably because humidity is not as strong a limiting fact as in the drier continents (Fig. 16b).

Could different meteorological conditions explain variations of the relative environmental influences on the MCSs between different phases of the convective lifecycle and the three tropical regions? Figure 16a shows that aerosol concentrations and meteorological conditions do not change significantly between the three phases of the MCSs' lifecycle. Thus, the decrease of the total variance explained by meteorological conditions is unlikely to be caused by their changes during the MCSs' lifetime. The increased fraction of the total variance of MCSs' lifetime explained by aerosols during the decay phase is consistent with numerical model simulations [*J W Fan et al.*, 2013; *Lohmann and Feichter*, 2005] and supports the cloud lifetime enhancement by the aerosols during that phase. This can be explained by the significant fraction of the variance of ice content inside the convective core and smaller cloud particles in convective anvils explained by f_{AOD}. These effects could reduce sedimentation of ice particles and dissipation of convective anvils. We cannot rule out an influence of the reduced background aerosol loading on lifetime [*Rosenfeld et al.*, 2008; *Van Den Heever and Cotton*, 2007].

Figure 16b shows that equatorial Africa is the driest region and has highly variable relative humidity in the low and middle troposphere, as shown by the means and standard deviations of the RH_{850} and RH_{500}. The region also has relatively low VWS, but is rich in aerosols (f_{AOD}). Thus, moisture availability could

be the primary limiting factor for lifetime of the MCSs [*R. A. Houze*, 2004] and the RH_{850} and RH_{500} together explain about 70% of their total variance. The MCSs over equatorial South America are surrounded by the lowest f_{AOD} (when we consider f_{AOD} over the land sectors of all three regions) and VWS (Fig. 16b) and the highest amount of RH_{850}. Such favorable meteorological (Fig. 13b) and aerosol conditions may explain stronger connection between f_{AOD} and MCSs' lifetime over South America (Figs. 15c and 15d) than those over equatorial Africa and South Asia. In addition, MCSs over equatorial South America are smaller in size (mean radius ~168 km), have lesser numbers of convective cores (mean NCC ~3) and shorter lifetime (< 20 hours) compared to those of equatorial Africa (mean radius ~440 km, 37 hours, and mean NCC ~ 10) and south Asia (mean radius~490 km, 120 hours, and mean NCC ~ 9). The combination of these meteorological, aerosol conditions, and MCSs' structures may contribute to stronger influence of aerosols on those MCSs over equatorial South America.

Over the Indian Ocean, Bay of Bengal, and Arabian Sea, f_{AOD} that surrounds the MCSs over the ocean is 35% less than that over the land. The mean CAPE, RH_{500}, and deep level VWS associated with the MCSs over the ocean are the strongest among all the regions. Mean CAPE over land is (~ 860 J/kg) lower than that over the ocean, consistent with previous findings based on reanalysis [*Riemann-Campe et al.*, 2009] and meteorological station's data sets [*Bhowmik et al.*, 2008]. RH_{850} associated with the MCSs over the oceanic surface is also high. Based on Fig. 13, such meteorological conditions favor a stronger increase of MCSs lifetime with f_{AOD}. Figure 16c shows the mean and variability (standard

deviation) of the MCSs' lifetime over the three regions of our analysis and the adjacent oceans. The MCSs over South Asia have the longest lifetime, on average 120 hours, which is three times the average lifetime of the MCSs over equatorial Africa (37 hours) and six times of that over equatorial South America (19 hours). Only 55% of the MCSs over south Asia originally form over the land, whereas about 80-90% of the MCSs originated from land over equatorial South America and equatorial Africa. Moreover, when we consider all the MCSs, we find that the mean lifetime of convection (irrespective of whether it originates over land or ocean) over the land (orange bar) is approximately half of the time convection spends over the ocean (blue bar). In other words, 45% of the systems that end up decaying over the land spend much of their lifetime over the ocean.

Throughout our analysis, f_{AOD} explains high fractions of total variance of the MCSs' lifetime when f_{AOD} values are low, for example, over equatorial South America (with the lowest continental f_{AOD} over all the regions), over the Indian Ocean, Bay of Bengal, and Arabian Sea, and during the decaying stage.

Many environmental parameters, such as the CAPE [*Robert A. Houze*, 1993; *R. A. Houze*, 2004; *Mapes*, 1993; *Edward J. Zipser*, 2003] , RH [*William R. Cotton and Anthes*, 1989; *J W Fan et al.*, 2007; *Robert A. Houze*, 1993; *Langhans et al.*, 2015], and VWS [*William R. Cotton and Anthes*, 1989; *J W Fan et al.*, 2009; *Maddox et al.*, 1979; *Petersen et al.*, 2006; *Weisman and Rotunno*, 2004], have been known to influence MCSs lifetime. However, to our knowledge, this is the first satellite based global tropical continental scale assessment of the relative roles of meteorological conditions versus aerosols in determining the variations

of cloud ice and lifetime of the MCSs using collocated geostationary, a set of closely synchronized polar orbital satellites as part of the A-train satellite constellation, and MERRA reanalysis datasets on MCSs' lifetime. These results show that aerosol can either increase MCSs' lifetime under higher relative humidity, CAPE, and moderate-high deep tropospheric vertical wind shear, or decrease MCSs' lifetime under lower relative humidity, CAPE, and low vertical wind shear. On the global tropical continental scale, an increase in MCSs' lifetime with aerosol are most apparent during the decay phase, presumably by increasing the ice water content of convective anvils and convective cores. Such a dependence of the aerosol effect on specific meteorological conditions and phases of the MCS's lifecycle presumably explains the difficulty of establishing aerosol effects on global scale with its large variations to meteorological conditions. It also appears to broadly explain a stronger influence of aerosols on MCSs' lifetime in humid equatorial South America during the wet season and over the Indian Ocean/Bay Bengal with lower aerosol loading, versus the relatively dry conditions with higher aerosol loading over equatorial Africa and dry season South America. Thus, the approach developed in this study can potentially provide a key to reconcile the differences of the aerosol effects on the MCSs reported in various literature.

MCSs produce heavy rainfall and thus their lifetime should be important for determining rainfall/flood and diabatic heating for atmospheric circulations. Yet, our understanding of aerosol impacts on MCSs' lifetime has been very limited in large part due to lack of adequate long term observations on large

scales. The large samples of the MCSs observed by a suite of satellite sensors over global tropical continents have enabled us to evaluate aerosol effects during different phases of MCSs lifecycle under similar meteorological conditions. In doing so, this work has advanced our capability to evaluate whether or not aerosols can increase convective lifetimes on the climate scale and to identify what are the favorable meteorological conditions for aerosols to affect the lifetime of the MCSs. These are fundamental questions that have motivated many studies for decades. However, we did not address the influence of different types of aerosols (such as absorbing or scattering) on MCSs' lifetime, nor directly observe the effect of aerosols on cloud microphysics. Use of aerosol type data from in situ measurements, Cloud-Aerosol Lidar and Infrared Pathfinder Satellite Observation (CALIOP data) as well as aerosol index data from the Ozone Monitoring Instrument (OMI) along with ground based measurements could be the next step to address these limitations.

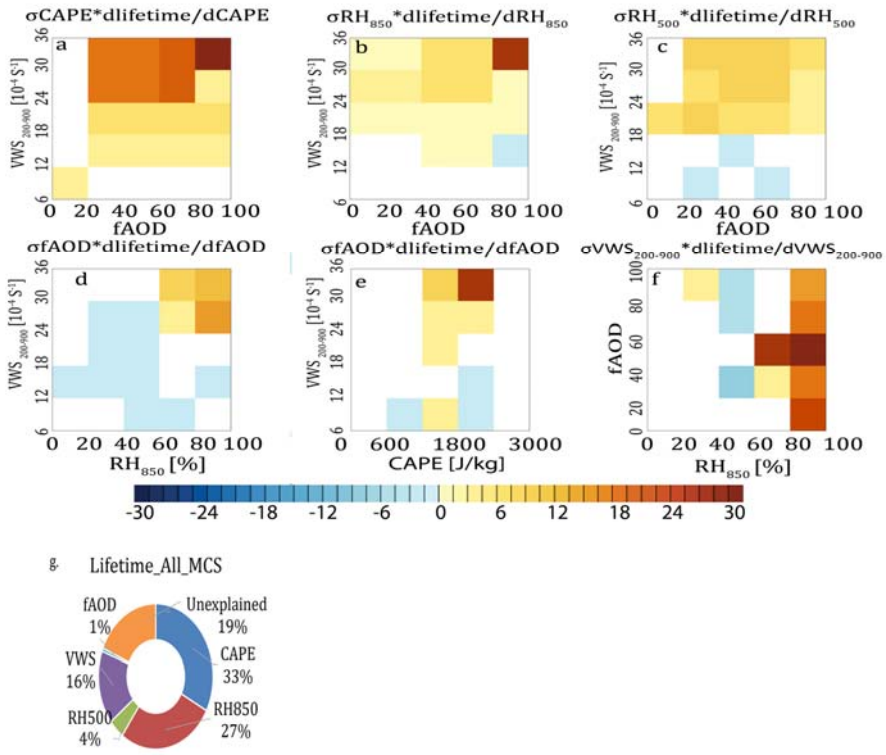

Figure 13. The rate of change of MCSs' lifetime (hours, color shades) with (a) CAPE, (b) RH_{850}, (c) RH_{500} as a function of f_{AOD} using AOD>0.15 over land and AOD>0.3 over the ocean as the threshold for a polluted environment and the deep tropospheric VWS, (d) f_{AOD} as a function of RH_{850} and the deep tropospheric VWS, (e) f_{AOD} as a function of CAPE and the deep tropospheric VWS, and (f) VWS as a function of the RH_{850} and f_{AOD}. The rates represent a change of MCSs' lifetime in hours associated with the variation of 1σ of that parameter. The bins with the number of samples less than 20 and insignificant rate of change at 95% confidence level are not shown. Note: $fAOD = NP_{AOD>0.15} / (NP_{AOD>0.15} + NP_{AOD<0.15})$ over land and $f_{AOD} = NP_{AOD>0.30} / (NP_{AOD>0.30} + NP_{AOD<0.30})$ over ocean. NP is the number of pixels. The pie chart in (f) shows the fraction of variance of MCS's lifetime explained by the environmental variables using multiple linear regression for all the MCSs.

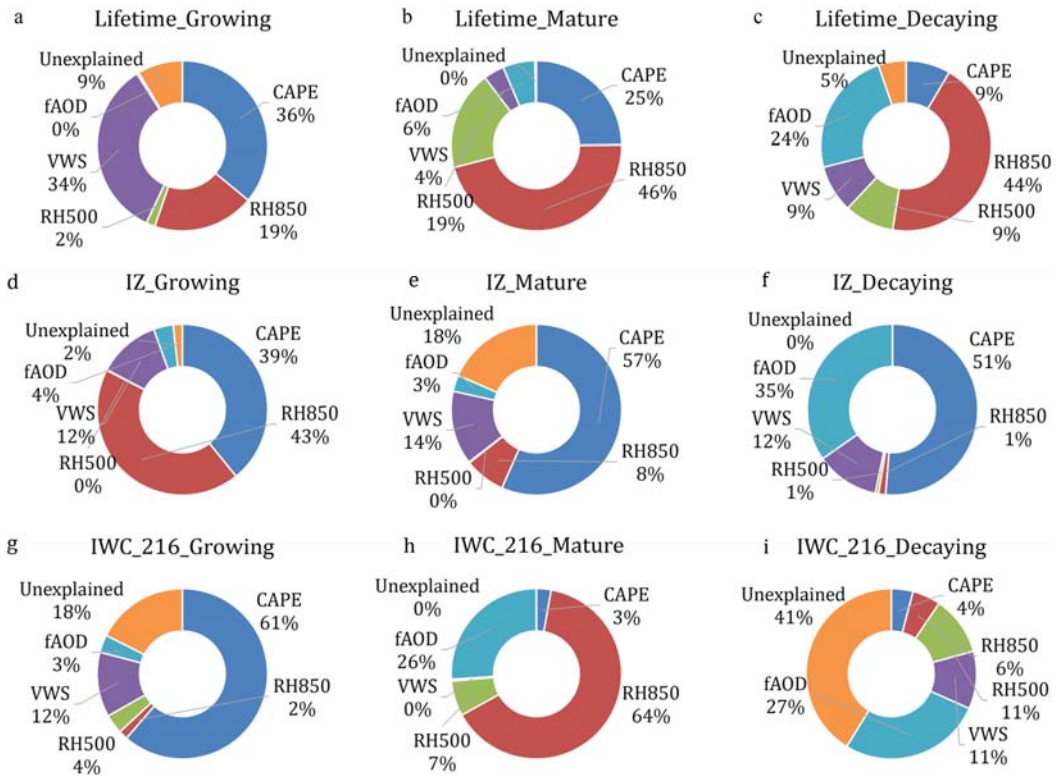

Figure 14. Fraction of the total variance of the MCS's lifetime (a, b, c), IZ (d, e, f), and IWC_216 (g, h, i) explained by the environmental variables based on the multiple linear regression during the growing, mature, and decaying phases of the MCSs.

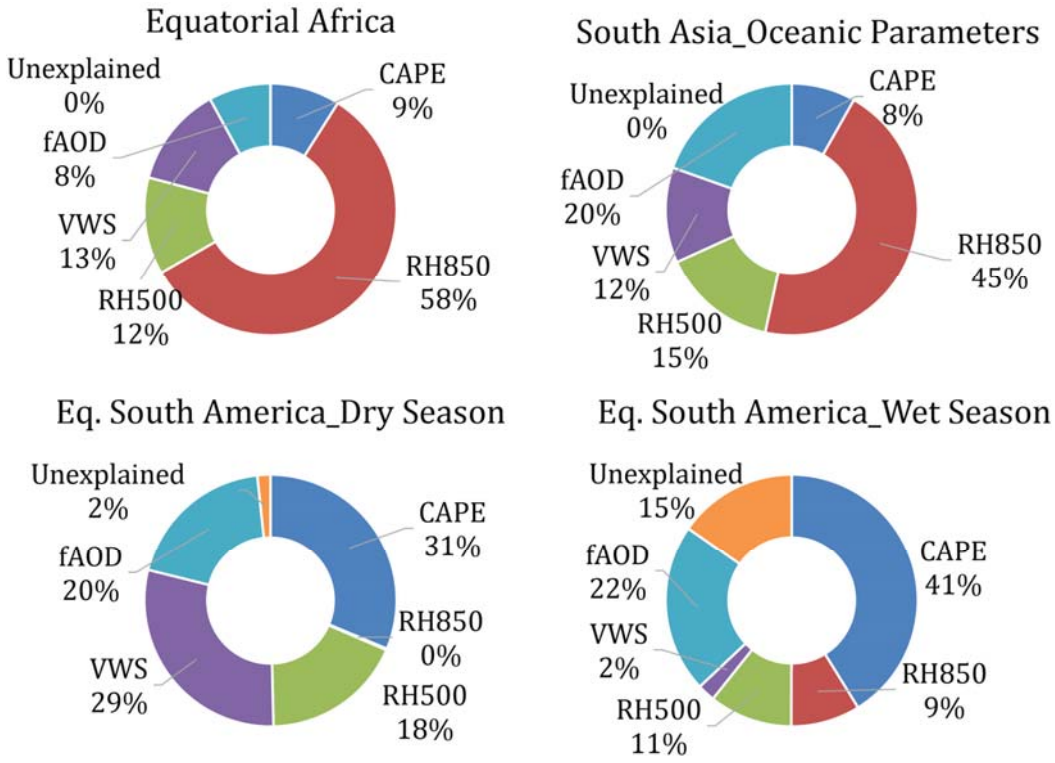

Figure 15. Fraction of the total variance of MCS's lifetime over different geographic regions (a) equatorial Africa, (b) South Asia, (c) equatorial South America during dry season, and (d) equatorial South America during wet season. For the Asian domain, we use the environmental parameters associated with the MCSs over the ocean and the AOD threshold of 0.3 for polluted conditions in the vicinity of the MCSs.

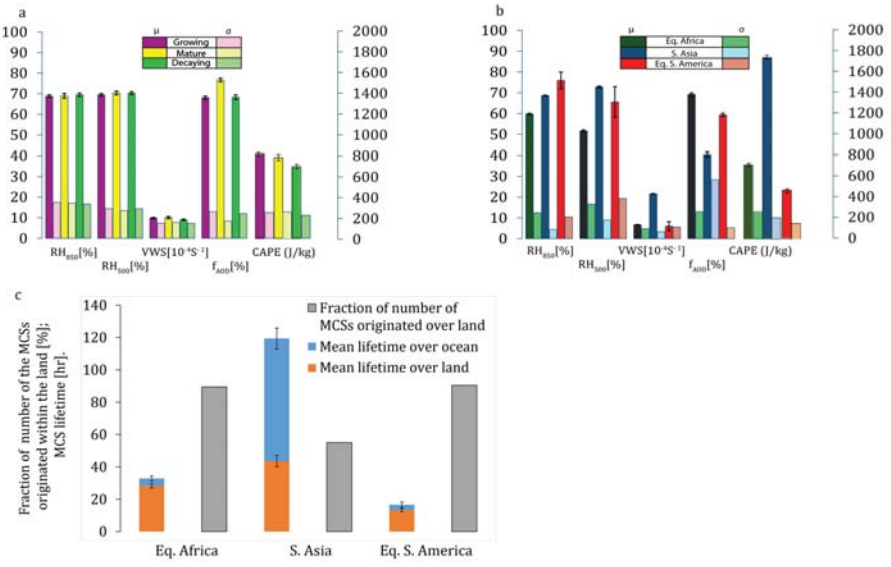

Figure 16. (a) Variations in mean values (μ, dark colors) and standard deviations (σ, light colors) of RH_{850}, RH_{500}, VWS, f_{AOD} (left Y axis) and CAPE (right Y axis) at different phases of the convective life cycle. The error bars associated with the mean values represent intervals of two standard errors around the mean. (b) Same as in (a), but over different regions. (c) Mean and two standard errors of MCSs' lifetime spent over the land (orange bars) and ocean (blue bars) for equatorial Africa, South Asia, and equatorial South America in 2007. For South Asia, only monsoonal MCSs during June-September have been considered. The gray bars in each plot represents the fraction of MCSs that originated over the land for each region. For the Asian domain, the parameters in a, and b are estimated over the ocean and f_{AOD} is computed using AOD>0.3 as the threshold for a polluted environment (see text).

3.4 Supporting Information

3.4.1 Data

Aqua MODIS: We have used the level 3 Aqua Moderate Resolution Imaging Radiometer (MODIS) AOD data set for the period of January 2003 to June 2008. This dataset has 1 km resolution and is also well validated [*Chu et al.*, 2002; *Remer et al.*, 2002]. In order to avoid erroneous measurements near the clouds [*Tackett and Di Girolamo*, 2009; *Varnai and Marshak*, 2009], we have calculated

the total number of aerosol pixels within a radial distance of 2° from the boundary of the clouds. We use AOD>0.15 over land and AOD>0.3 over ocean, respectively, [*Koren et al.*, 2008; *J Lee et al.*, 2012; *Livingston et al.*, 2014; *Rosenfeld et al.*, 2008] to determine the polluted pixels and calculate f_{AOD}. f_{AOD} surrounding a MCS is calculated as:

$$f_{AOD} = \left(\frac{\text{number of pixels with AOD>0.15 (or 0.3)}}{\text{total number os pixels surrounding the MCS}}\right) \quad (1)$$

ISCCP DX: We derive convective lifetime, number of convective cores (NCC), size of the storms (RAD) and the position of the storm (from the latitude and longitude of the center and the RAD) from the International Satellite Cloud Climatology Project (ISCCP) dataset [*Machado et al.*, 1998]. ISCCP DX dataset specifies observations of convective clouds, every three hours, of size greater than 100 km from 1983 to June 2008. Based on 28 different properties, Machado et al. [*Machado et al.*, 1998] provided the method of tracking deep convective clouds. Phases of the lifecycle are calculated according to the values of AE (see equation 2); larger positive values of AE (AE > 0.1) are associated with the growing stage of the convective life cycle, whereas larger negative values (AE < –0.1) are associated with the decaying stage [*Chakraborty et al.*, 2015; *Machado et al.*, 1998]. Values of AE associated with mature MCSs are close to 0 (i.e., –0.1 ≤ AE ≤ 0.1). Phases of convective life cycle can also be derived from ISCCP DX data based on the expansion ratio [*Machado et al.*, 1998]:

$$\mathrm{AE} = \frac{1}{\mathrm{A}}\left(\frac{\mathrm{dA}}{\mathrm{dt}}\right) \quad (2)$$

where A is the area of the convective system and t is the time.

MERRA: We also use the Modern Era Retrospective – Analysis for Research and Applications (MERRA) data sets to calculate the RH_{850} and RH_{500} in order to estimate the low level and mid-level humidity. Since MERRA also provides data at 3 and 6 hour intervals, we use the data provided in the ISCCP data set to locate the positions and boundaries of the MCSs in the MERRA data and calculate RH at a radial distance of 2° from the boundary of the clouds at two levels. VWS associated with each MCS is calculated as the difference between the mean wind speeds of the layers 925-850 hPa and 200-200 hPa[*Petersen et al.*, 2006]. It is then divided by the difference between the mean geopotential heights (∂z) of the layers used (see equation 3). For low level VWS we take the differences in mean wind speed and geopotential height between the layers 950-900 hPa and 750-700 hPa. We calculate VWS from MERRA data:

$$\mathrm{VWS} = \frac{\partial \mathrm{u}}{\partial \mathrm{z}} \tag{3}$$

where ∂u is the change in mean zonal wind speed and ∂z is the difference in mean geopotential height between the 925–850 hPa and 250-200 hPa layers for the deep tropospheric VWS, and between the 950-900 hPa and 750-700 hPa layers [*Petersen et al.*, 2006] for the low tropospheric VWS. We calculate CAPE between the level of free convection to the level of no buoyancy using the specific humidity (then, converted to mixing ratio) and the temperature datasets for all the grid cells under the MCSs.

CloudSat: CloudSat has a wavelength of 3 millimeter [*Langenberg*, 2005] and measures the power backscattered by the clouds as a function of distance from the radar [*Stephens et al.*, 2002]. The data have a vertical resolution of 240 m and horizontal resolution of 1.4 km (across track) x 1.7 km (along-track). We use radar backscatter profile (2B-GEOPROF) data with good quality (quality index equal to 0). The valid range of detection is -40 to 50 dBZ. We use the reflectivity data to represent the cloud ice water content rather than the retrieved values derived from the reflectivity data. We compute IZ for the collocated MCSs between CloudSat, MODIS, and ISCCP between June 2006 to June 2008 since CloudSat datasets are available since June 2006. From the reflectivity data, we first calculate the mean vertical reflectivity (Z) profile for each of the co-located MCSs. Figure 20 shows a typical mean reflectivity profile of a MCS. The level of maximum reflectivity denotes the freezing level or the melting layer due to the melting hydrometeors [*Matrosov*, 2009a; b; *Matrosov et al.*, 2007]. Under the freezing level, the rain layer decreases the reflectivity due to the attenuation [*Matrosov*, 2007]. We integrate the mean reflectivity above the freezing level with height to derive IZ (see equation 4). We integrate the mean vertical reflectivity profile (IZ) above the freezing level to represent the columnar IWC [*Matrosov*, 2009a] as:

$$\mathrm{IZ} = \int \mathrm{Z}\,\mathrm{dh} \tag{4}$$

where h is the height in km.

AURA MLS: We also use version 3.3 Aura Microwave Limb Sounder (MLS) retrievals of IWC to estimate the changes in the anvil IWC due to aerosols at 216

hPa. We have applied the "2σ – 3σ" screening process [*Livesey et al.*, 2013] to eliminate the uncertainties due to the effects of spectroscopic and calibration by removing IWC retrievals that are less than three standard deviations above the mean in 10° latitude bands. As our analysis is limited over the tropical region, we exclude the possibility of uncertainties in IWC due to gravity waves originating in the wintertime stratosphere over middle-to-high latitudes during wintertime. To be consistent with IZ analysis from CloudSat, we also analyze MCSs collocated between June 2006 to June 2008.

3.4.2 Statistical methods

In addition to estimate the rate of change of MCS's lifetime with a variation of one standard deviation of CAPE, RH, and VWS (both low and deep level), we also apply a multiple linear regression method. In this method, the fraction of variance of the MCSs' lifetime explained by different meteorological parameters and aerosols is estimated. The dependent variable (here, MCSs' lifetime) is statistically modeled as a linear combination of independent variables:

$$yi = \beta + \sum_{j=1}^{p} \beta j x i j \qquad (5)$$

where β is the intercept and β_j, j€ [1,p] is the coefficient associated with the j^{th} of p predictors for the dependent variable y_i. In this paper, we use traditional methods for multiple linear regression that selects the coefficients in order to minimize the residual sum of squares for N number of runs:

$$\sum_{i=1}^{N} (yi - \beta - \sum_{j=1}^{p} \beta j x i j)^2 \qquad (6)$$

The method of collocating contains many potential sources of random error. One such source is the measurement uncertainty due to the differences in the part of the MCSs the satellites observe. For example, a CloudSat swath can pass through the center as well as through the edge of the cloud. To counteract this problem, we first sort the data in increasing order of convective lifetime. We then bin the predictors (CAPE, RH_{850}, RH_{500}, VWS, f_{AOD}; xij) and the dependent variable (convective lifetime; yi) and construct a model based on multiple linear regression methods. Starting with 10 samples, we gradually increase the number of samples in each bin and each time, we obtain a model with residual sum of squares (equation 6), coefficients (βj) associated with different predictors, and variance of MCSs lifetime explained by them. Given a set of the 5 predictors, our objective is to identify a line that best fits the points. In other words, the optimal model is chosen based on the minimum value of residual sum of square. We report the explained variance of convective lifetime by different predictors corresponding to that optimal model.

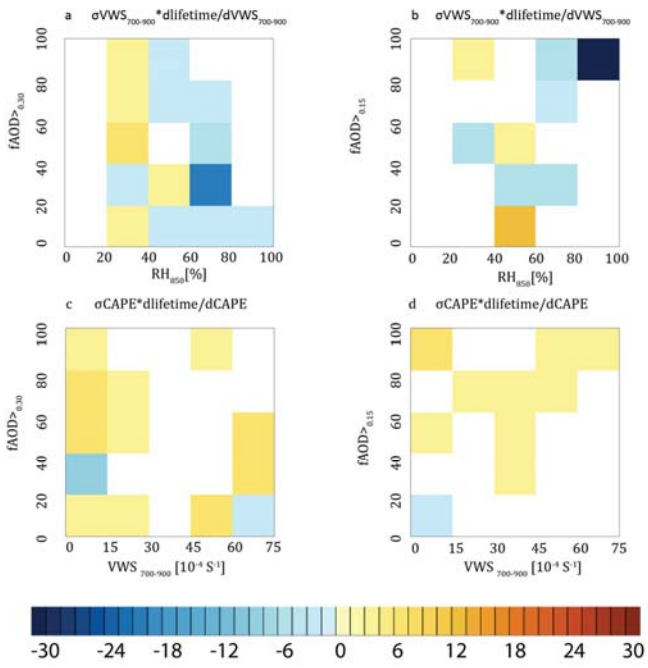

Figure 17. The rate of change of MCSs' lifetime (hours) with (a, b) low level VWS for various bins of similar f_{AOD} and RH_{850} values and (c, d) with CAPE for various bins of similar low level VWS and f_{AOD} values. The left panel uses f_{AOD} values calculated with AOD threshold of 0.3. The right panel uses f_{AOD} with AOD threshold of 0.15. The bins with number of samples less than 20 and rates insignificant at 95% confidence level are not shown. Note: $f_{AOD} = NP_{AOD>0.15(0.3)} / (NP_{AOD>0.15(0.3)} + NP_{AOD<0.15(0.3)})$.

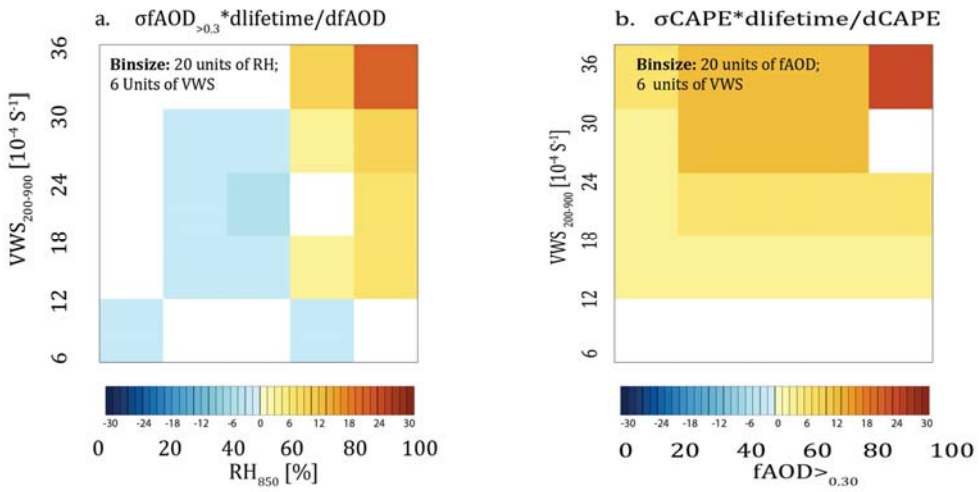

Figure 18. (a) The rate of change of MCSs' lifetime (hours) with one standard deviation of f_{AOD} (0.3 as the AOD threshold for polluted pixels) as a function of deep tropospheric VWS. and RH_{850} . (b) The rate of change of MCSs' lifetime with one standard deviation of CAPE as a function of deep tropospheric VWS. and f_{AOD} (0.3 as the AOD threshold for polluted pixels).The bins with number of samples less than 20 and rates insignificant at 95% confidence level are not shown.

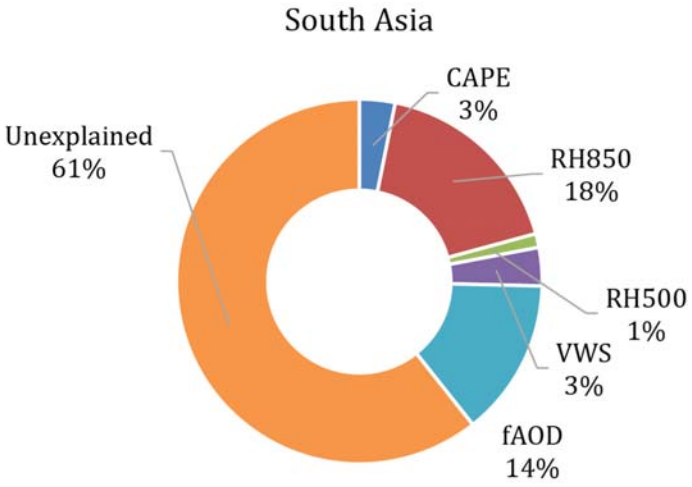

Figure 19. Fraction of the total variance of MCS's lifetime explained by the environmental variables using the MCSs over land (using AOD threshold of 0.15) and ocean (using AOD threshold of 0.3) over south Asia.

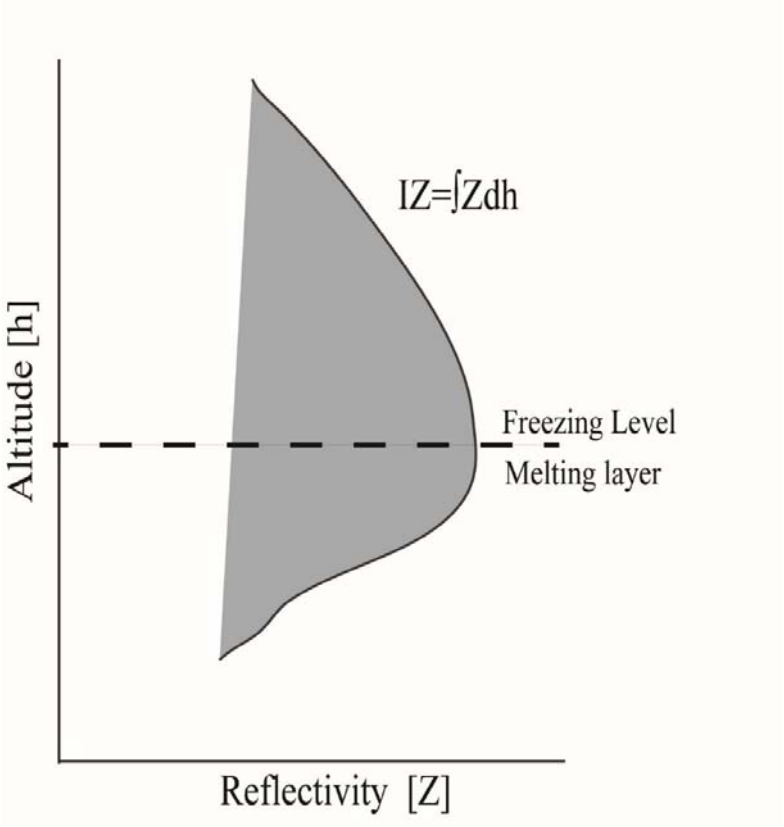

Figure 20. IZ represents the vertical integrated radar reflectivity above the freezing level using a typical reflectivity profile of a MCS as measured by the W band cloud radar.

Chapter 4

Relative influence of the meteorological and aerosol conditions on the mesoscale convective systems through their lifecycle over tropical continents

4.1. Introduction

Mesoscale convective systems (MCSs) with hundreds of kilometers in radius and lasting at least six hours are a primary source of precipitation over the tropics and mid-latitudes [*R. A. Houze*, 2004] and have disproportionally large influence on the variability of the extreme rainfall events, such as flood and droughts [*R. A. Houze et al.*, 2015]. Past studies have suggested that the intensity and life cycle of the MCSs are mainly determined by atmospheric thermodynamic and dynamic conditions [*R. A. Houze*, 2004; *S S Lee*, 2012; *Schumacher et al.*, 2004]. Over recent decades, many studies using numerical model simulations and observations have suggested aerosols as another factor that could influence the MCSs' water content, precipitation, longevity, and dynamic structure [*J W Fan et al.*, 2007; *J W Fan et al.*, 2013; *S S Lee et al.*, 2014; *Rosenfeld et al.*, 2008; *Stevens and Feingold*, 2009; *Tulet et al.*, 2010; *Van Den Heever and Cotton*, 2007]. For example, *Rosenfeld and Woodley* [2000] have reported that aerosol particles increase the total number of cloud condensation nuclei (CCNs) by reducing their effective radii. As a result, the process of coagulation and coalescence of the smaller CCNs into larger rain droplets slows down leading to a delay or suppression in precipitation due to an enhanced aerosol (both smoke as well as

dust) concentrations [*Rosenfeld and Lensky*, 1998; *Rosenfeld et al.*, 2007]. In absence of the downdraft, an increased amount of moisture enters the MCSs through the updrafts and releases enhanced amount of latent heat of condensation that makes the clouds even more buoyant. Hence, ice water content (IWC) as well as the size of the MCSs increase and cloud top often reaches higher altitude as observed by *Koren et al.* [2010a] that cloud top height increases by 120-260 m when aerosol optical depth (AOD) increases by 0.1. *Tulet et al.* [2010] found that smaller sized dust particles over Niger reach the anvil of the MCSs and increase ice particle number concentrations near the tropopause. Moreover, *de Boer et al.* [2010] also reported that aerosol can increase stratiform IWC and anvil longevity [*Bister and Kulmala*, 2011]. *Bell et al.* [2008] reported an increase of midweek thunderstorm activity coincides with an increase in midweek aerosol concentration over the southeastern United States.

However, the influence of aerosols on clouds, especially on the MCSs, is still not clear in literature. For example, *Chylek et al.* [2006] reported that larger ice particles form inside the anvils when MCSs are in a polluted environment and *S Sherwood* [2002] found out negative correlation between effective radius of ice particles and aerosol index data using a suite of satellite data sets. Conversely, *Massie et al.* [2007] reported that aerosols don't have significant effects on anvil ice crystals. Similarly, differences are also observed in studies investigating the aerosol impacts on cloud precipitation. Several studies show that aerosols suppress rainfall [*A Khain and Pokrovsky*, 2004; *A Khain et al.*, 2004; *Rosenfeld*, 1999; 2000], whereas other studies [*A Khain et al.*, 2005; *A P Khain et al.*, 2008;

Lin et al., 2006; *van den Heever et al.*, 2006; *R Y Zhang et al.*, 2007] indicate that precipitation is enhanced by aerosols.

Recent studies have attributed these differences of aerosol effects on convection reported in numerous literature to variations of meteorological conditions or convective types. For example, *Altaratz et al.* [2014] suggest that aerosols have stronger influence on strong convection with well protected convective cores than on weaker convection with diluted convective cores. *Rosenfeld et al.* [2008] hypothesized that the aerosols impact on MCSs vary with convective lifetime and such impacts are clearly and distinctively visible during the decay phase. On the other hand, meteorological parameters such as convective available potential energy (CAPE), relative humidity (RH) and vertical wind shear (VWS) have a strong influence on the convective structure of MCSs and also influence the aerosol distribution. For example, MCSs under weak VWS are invigorated due to enhanced aerosol concentrations [*J W Fan et al.*, 2007], but convective activity is suppressed under strong wind shear [*J W Fan et al.*, 2009] and the strength of the MCSs strongly depends on CAPE, which is related to the buoyancy that transports moisture from the warm and moist boundary layer to the systems [*R. A. Houze*, 2004; *Mapes*, 1993]. *J W Fan et al.* [2007] using cloud resolving models have shown that RH is an important factor in aerosol microphysics. Apart from the lower tropospheric humidity, lateral entrainment of free tropospheric humidity is also important as it contributes to a significant fraction of the total rainfall [*Langhans et al.*, 2015] and parcel's ascent [*R. A. Houze*, 2004; *E. J. Zipser*, 1977]. Thus, *Rosenfeld et al.* [2014a] points out that

aerosol invigoration is more detectable at cloud and regional scales under similar meteorological conditions than on large scale with strong variation of the meteorological conditions. The lack of general understanding on how aerosol effect on convection varies with meteorological conditions and relative importance of aerosols and meteorological conditions in determining the variability of the MCSs represent a major challenge in understanding aerosol influence on convection on climate scale [e.g., Stevens and Feingold 2009; Tao et al. 2013]. *Tao et al.* [2012] suggest that aerosols may not have any significant influence on MCSs that produce heavy rainfall.

Observational characterization of the aerosol influence on MCSs under various meteorological conditions and relative influences of aerosols and meteorological conditions on the variability of the MCSs represents a crucial first step to address this challenge. In this study, we gathered 2430 samples of the MCSs from three tropical continental regions including the equatorial Africa (10°N–10°S; 10°W–40°E), the equatorial South America (5°N–15°S; 40°W–80°W), and South Asia (0-40N, 70-100E) and evaluate the relative influence of aerosols and different meteorological parameters on MCSs' IWC and rainrates during the growing, mature and decay stages using data sets from A-Train constellation [*L'Ecuyer and Jiang*, 2010] that successfully detect clouds and aerosols [*Kato et al.*, 2011; *Varnai and Marshak*, 2009; *D M Zhang et al.*, 2010], Tropical Rainfall Measuring Mission (TRMM), International Satellite Cloud Climatology Project (ISCCP) [*Machado et al.*, 1998], and Modern Era Retrospective – Analysis for Research and Applications (MERRA) [*Rienecker et*

al., 2011], the latter is a reanalysis data set suitable for studies using A-Train data sets [*Chakraborty et al.*, 2015].

4.2 Data and Methodology

Ice particle size distribution depends on temperature and can vary from 2μm to about 1 cm in the stratiform layer and from 100 μm to about 1 cm in the convective regions [*Heymsfield et al.*, 2013], whereas a typical size of a CCN is 0.2 μm. Along with that, size of raindrops also varies [*Hodson*, 1986; *Marshall and Palmer*, 1948]. Hence to analyze impacts of aerosols on clouds, one needs to analyze a suite of observations from different satellite sensors since one sensor only measures limited range of cloud particle sizes. For example, CloudSat is a 94 GHz W band radar that measures the reflectivity, ice water content owing to larger ice particles. TRMM is a 13.8 GHz precipitating radar and it measures rates of precipitation consisting of much bigger sized droplets (including grauples to hailstones; large hydrometeor rainrate, RR, hereinafter). MLS on board of the Aura satellite is a microwave radiometer that measures the thermal emission from broad spectral bands near 118 -640 and 2500 GHz and provide information about anvil IWC.

4.2.1 Data

We use ISCCP DX data sets to estimate different convective parameters and the stage of the lifecycle. Details about the ISCCP collocating data are given in *Machado et al.* [1998]. This data only consider the MCSs that have size greater than 100 km and lasts more than 6 h of time. The data are available between

1983 and June 2008. Based on matching 28 different parameters of a MCS with the same 28 parameters measured 3 hours previously at 30 km resolution, *Machado et al.* [1998] developed a method of tracking the clouds using ISCCP DX data. Using the ISCCP DX data sets, there MCSs can be differentiated into the growing, mature, and decaying stages.

Aqua Moderate Resolution Imaging Spectroradiometer (MODIS) aerosol optical depth (AOD) data set is available for a wide swath of 2300 km at 1 km resolution. MODIS AOD (MYD04-L2) data can be used for scientific purposes [*Chu et al.*, 2003; *Chu et al.*, 2002; *Remer et al.*, 2005]. Satellite measurement of aerosols in the vicinity of clouds is very difficult since AODs may change as a function of distance from clouds due to changes in RH [*Tackett and Di Girolamo*, 2009; *Varnai and Marshak*, 2009]. In order to avoid erroneous values of AOD due to 3D radiative transfer [*Varnai and Marshak*, 2009], we calculate the number of pixels of AOD above (polluted pixels, $NP_{AOD>0.15}$) and below 0.15 (Clean pixels, $NP_{AOD<0.15}$) within a radial distance of 2° from the boundary of the clouds. The reasons behind selecting AOD equals to 0.15 as a threshold for polluted condition is discussed later in the methodology section.

We use along track reflectivity data from CloudSat to understand IWC inside the dense core region of the MCSs since CloudSat is able to see larger sized ice cloud particles. CloudSat has 3 millimeter wavelengths [*Langenberg*, 2005] and measures the power backscattered by the clouds as a function of distance from the radar [*Stephens et al.*, 2002]. The data have a vertical resolution of 240 m and horizontal resolution of 1.4 km (across track) x 1.7 km (along-track). The

radar backscatter profile (2B-GEOPROF) data are used and the retrieval process considers only one phase of water at a time. A strong echo with mask value equals to 40 has a <0.2% false detection. We use observations with good quality data (quality index equal to 0). The valid range of detection is -40 to 50 dBZ.

We use version 3.3 Aura Microwave Limb Sounder (MLS) IWC at 216 hPa (IWC_{216}) altitude, where convective anvils are located. MLS IWC is obtained from the 240-GHz channel with a 1.5 degree horizontal resolution. We screen the data using the '2σ-3σ' method [*Livesey et al.*, 2013]owing to their spectroscopic and calibration errors.

We calculate RH and VWS using MERRA data. These data sets have 1.25° x 1.25° as well as 0.67 x 0.5 degree horizontal resolution with 42 vertical pressure levels with temporal resolution of 3 and 6 hours, respectively.

We use TRMM 2A25 data sets which provide vertical rainrates measured by the precipitation radar (PR) with frequency equal to 13.8 GHz. RR is derived from PR level 1A data. The data are available from December 8th 1997 to April 1st 2015 and has a spatial coverage in-between 38°S and 38°N. The horizontal resolution is 5 km with swath width of 215 km. The rainrates are available from 0 to 20 km altitude. We also use TRMM 2B31 data sets to estimate LH profiles of the MCSs. TRMM 2B31 is a combined data set that uses PR radar and microwave imager (TMI) measurements. The data also have the same spatial and temporal coverage as the TRMM 2A25 data. The LH is calculated in 13 different layers using the vertical fluxes of different hydrometeor species as well as latitude and longitude dependent averaged archival temperature, pressure, and humidity

soundings. In the version 7 data that we use, all the precipitation is assumed to be liquid.

4.2.2 Methodology

ISCCP DX is a geostationary data set, whereas the instruments on board A-Train mission as well as TRMM are orbital in nature and they take measurements at different locations at different time. Hence, we have collocated the geostationary and the orbital data sets to identify the MCSs used for this study. Details of the colocation method and related error analysis are given in *Chakraborty et al.* [2015]. Since different satellite has different time period of observations, we collocate A-Train satellites (CloudSat and Aura MLS) with the ISCCP DX data for June 2006-June 2008. Since TRMM is not synchronized with the A-Train constellation and observes the Earth over a different time and location, its collocation with A-Train data set further limits the number of samples in the analysis. Hence, we extend our collocation between TRMM data with the ISCCP DX and MODIS data sets from January 2003- June 2008 in order to obtain larger (2430) number of samples.

Although AOD greater than 0.3 has been used as an indicator of polluted condition [*J Lee et al.*, 2012; *Livingston et al.*, 2014], *Koren et al.* [2008] found out that aerosol microphysical effect saturates and reverses at AOD>0.3 for deep convective clouds. *Rosenfeld et al.* [2008] found out that an increase in CCN reduces the vigor of the convections, but moderate concentrations of CCN maximizes that. Hence, we estimate total number of polluted pixels surrounding a MCS ($NP_{AOD>0.15}$) by setting AOD>0.15 as a threshold. Aqua MODIS cannot

detect aerosols under the cloud; hence, we determine fraction of AOD pixels (f_{AOD}) as a ratio of $NP_{AOD>0.15}$ to the total number of pixels ($NP_{AOD>0.15}$ + $NP_{AOD<0.15}$) within a radial distance of 2° from the perimeter of the MCS.

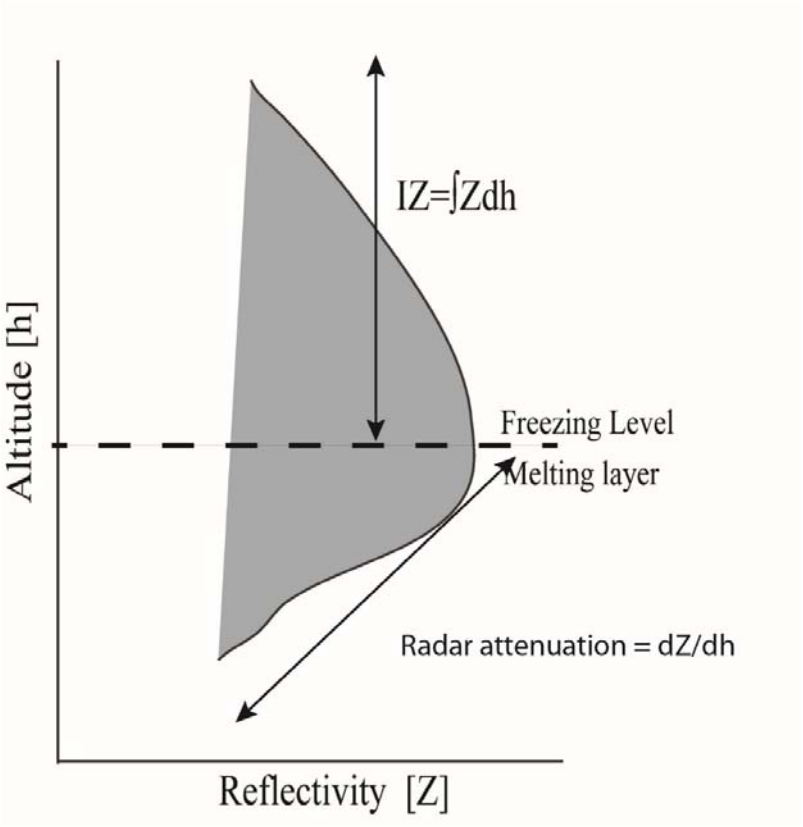

Figure 21. Calculation of IZ and radar attenuation below freezing level from a mean reflectivity profile of a MCS as measured by the CloudSat radar.

The radius (RAD), number of convective core (NCCs), latitudes and longitudes of the center of the systems, and the phase of convective lifecycle are calculated from the ISCCP data. NCCs within the convective part act as a pathway for the updraft that contains water vapor, aerosols, and many other gases to the top of the convection. By determining the center and size of the convection, it's

possible to detect the position and the propagation of the cloud every three hours. The life cycle of a MCS is calculated from the areal time rate of expansion ratio:

$$\mathrm{AE} = \frac{1}{\mathrm{A}}\left(\frac{\mathrm{dA}}{\mathrm{dt}}\right) = \nabla \cdot \mathbf{V} \quad (1)$$

where A is the area of the convective system and **V** is the horizontal wind vector [*Machado et al.*, 1998]. Larger positive values of AE (AE > 0.1) are associated with the growing stage of the convective life cycle, whereas larger negative values (AE < –0.1) are associated with the decaying stage. Values of AE associated with the mature MCSs are close to 0 (i.e., –0.1 ≤ AE ≤ 0.1) [*Chakraborty et al.*, 2015; *Machado et al.*, 1998].

From the reflectivity data, we first calculate the mean reflectivity (Z) profile for each of the co-located MCSs and calculate IZ (Figure 21). The level of maximum reflectivity denotes the freezing level or the melting layer due to the melting hydrometeors [*Matrosov*, 2009a; b; *Matrosov et al.*, 2007]. We integrate the mean reflectivity profile (IZ) above the freezing level to represent the IWC inside the MCSs' cores above the freezing level [*Matrosov*, 2009a]:

$$IZ = \int \mathrm{Z}\,\mathrm{dh} \quad (2)$$

where h is the height in km. IZ typically represents the IWC comprising of the larger ice particles observed by CloudSat inside the dense core regions of the MCSs where IWC is often greater than 400 mg/m^3 as seen from the 2b-CWC-RO data set from CloudSat. On the other hand, IWC_{216} typically represents the anvil of the cloud and is measured by the AURA MLS satellite. The ice particles inside

the anvil are smaller in size and IWC is also less (mean IWC_{216} of all the MCSs we used is ~ 20 mg/m^3).

MERRA data set successfully detects clouds along the track of the A-Train data sets [*Chakraborty et al.*, 2015]. To calculate RH, we use cloud free regions surrounding the MCSs within a range of ±2° from the perimeter of the cloud at 850 hPa (RH_{850}) and 500 hPa (RH_{500}) levels, representing the lower and middle tropospheric humidity, respectively. These two parameters are selected because they influence the humidity of the cloud base and lateral entrainment into convection. We use the location of the center, radius, and the timing as per the ISCCP data set since both ISCCP and MERRA data sets are reported at every 3 hours. We also used the wind data to calculate the VWS:

$$VWS = \frac{\partial \mathrm{u}}{\partial \mathrm{z}} \tag{3}$$

where ∂u is the change in zonal wind speed. The deep level VWS associated with each MCS is calculated as the difference between the mean wind speeds of the layers 925-850 hPa and 250-200 hPa divided by the difference between the mean geopotential heights (∂z) of the respective layers [*Petersen et al.*, 2006] to represent the deep tropospheric wind shear. We have also evaluated the influence of the lower tropospheric wind shear, defined by the mean wind difference between 950-900 hPa and 750-700 hPa, but its correlation with the variance of the MCS properties appear to be small. Thus, we do not show the analysis related to the lower tropospheric wind shear effects. To calculate CAPE, we use the temperature and the specific humidity data sets of MERRA associated with the MCSs. We compute CAPE between the level of free convection to the

level of no buoyancy. We use the mean values of CAPE of all the grid cells under the MCSs. Finally, mean RR under each MCS is calculated from the TRMM 2A25 data set. Mean LH profile is calculated from the TRMM 2B31 data set by averaging the LH values under the MCSs at 13 layers.

4.2.3 Statistical methods

In addition to estimating the rate of changes of RR associated with aerosols for constant ranges of RH and VWS values, we also use multiple linear regression method to infer the relative influence of aerosols and other meteorological parameters on IZ, IWC_{216}, and RR. In this method, dependent variable is statistically modeled as a linear combination of independent variables:

$$y = \beta 0 + \sum_{j=1}^{p} \beta j x j \quad (4)$$

where β_0 is the intercept and β_j, j€ [1,p] is the coefficient associated with the j^{th} of p predictors. The y is the dependent variable, which is the RR (or IZ and IWC_{216}) associated with large hydrometeors. It is obtained by averaging the precipitation rate of all the pixels under each cloud. The independent variables are the CAPE, RH_{850}, RH_{500}, VWS, and f_{AOD}.

In this paper, we use traditional methods for multiple linear regression that selects the coefficients in order to minimize the residual sum of squares:

$$\sum_{i=1}^{N} (y - \beta 0 - \sum_{j=1}^{p} \beta j x i j)^2 \quad (5)$$

This approach is suitable for investigating the influence of aerosols on MCSs since IWC and RR of the MCSs are also influenced by many other predictors

(meteorological parameters) that are also tightly correlated with each other and influence aerosols' distribution. In this method, the coefficients for most significantly related predictors may be large, but with opposite signs to compensate each other. The multiple linear model would compensate the values of the coefficients in such a way that they don't repeat or replicate the influences of one parameter. The method of collocating contains many potential sources of random errors. One of such is the measurement uncertainty due to the differences in the part of the MCSs the satellites observe. For example, a CloudSat or a TRMM swath can pass through the center as well as through the edge of the cloud. To counteract this problem, we have aggregated the entire MCSs into different bins. Bins are automatically chosen at an increment of 5 samples for the dependent and independent parameters. Then, multiple liner regression generates a linear equation for each bin-size based on equation 4. Each equation is also associated errors due to the linearity assumption of the method as per equation 5. Among all those equations, we choose one with the minimum error and calculate the explained variances by each variable in the equation.

4.3 Results

We evaluate the relative influence of different meteorological parameters and f_{AOD} on RR that is derived from TRMM 2A25 data sets. Figure 22 shows the rate of change of MCSs' RR associated with one standard deviation (1σ) change in CAPE, RH_{850} (lower tropospheric humidity), RH_{500} (ambient humidity around ~5.5 km altitude), f_{AOD}, and the deep tropospheric vertical wind shear (VWS), respectively, when other parameters have similar values. Our results show that

with an increase in CAPE by 1σ, RR either increases at the rate up to ~0.32 mm/h under low VWS and high f_{AOD} (Figure 22a), or decreases at the rate of -0.16 mm/h under high VWS and low f_{AOD} values. RR also increases at a rate of 0.1-0.3 mm/h with 1σ increase in RH_{850} (Figure 22b) and at a rate of 0.06-0.3 mm/h with 1σ of increase of RH_{500} under lower f_{AOD} condition (Figure 22c). RR either decreases with f_{AOD} under nearly saturated RH_{850} or VWS, or increases with f_{AOD} under 40-80% RH_{850} and intermediate VWS (10-30X10^{-4} S^{-1}) with rates ranging between -0.13 to 0.14 mm/h depending on meteorological parameters. Change of RR appear to be stronger with the changes of CAPE and RH than with VWS and f_{AOD} (Figure 22e, 22d).

The impact of aerosols on MCSs' rainrates depends on their interaction with the environment [*Del Genio and Wu*, 2010; *R. A. Houze*, 2004] and may not be clearly detectable by satellites until we divide and analyze the MCSs according to the phases of their lifecycle. Moreover, the MCSs interact with the environment in different ways depending on their size and structure that also varies with different phases of lifecycle [*Machado et al.*, 1998]. To clearly understand the impact of aerosols on RR at different stages of lifecycle, we compute the change in rainrates (mm/h) due to 1σ change in f_{AOD} at three different phases of lifecycle when other conditions like RH_{850} and VWS are fixed to constant values (Figure 23).

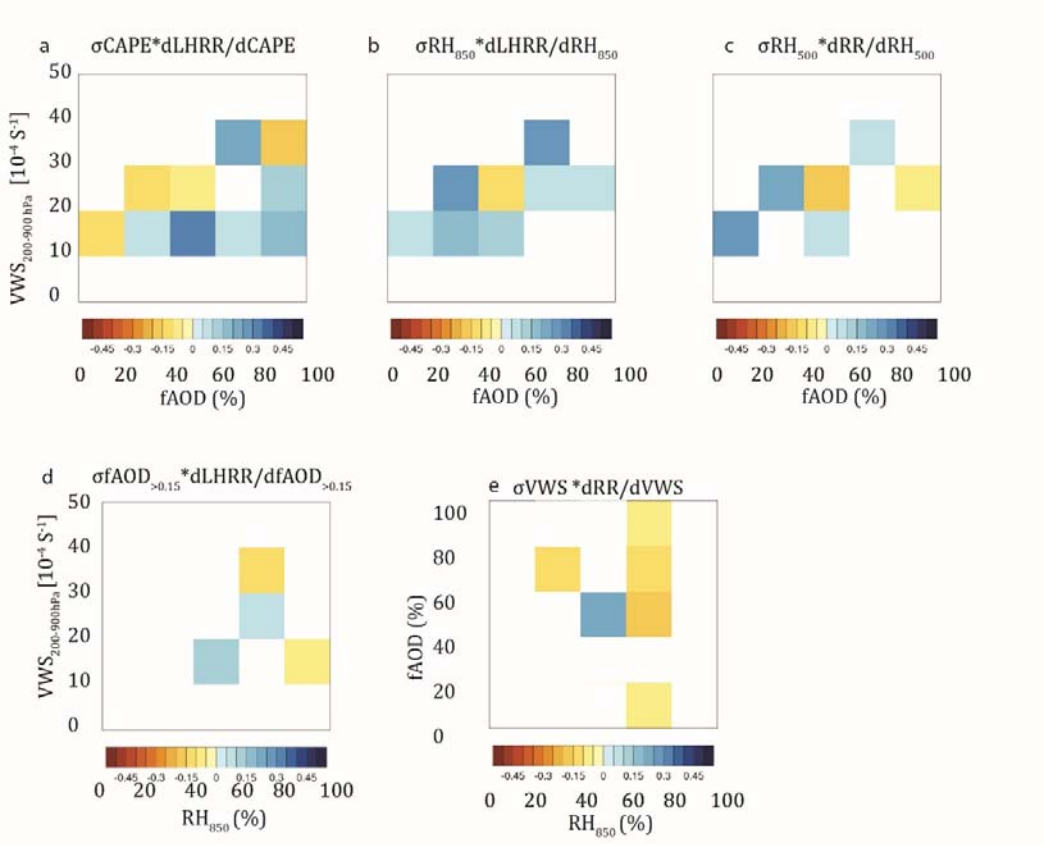

Figure 22. Rate of change of RR (mm/h) for 1σ change in (a) CAPE, (b) RH850 , (c) RH500 , (d) fAOD, (e) VWS using all the MCSs. White color denotes either insignificant change (see text) in rain rate reported or number of samples of the bin is less than 20.

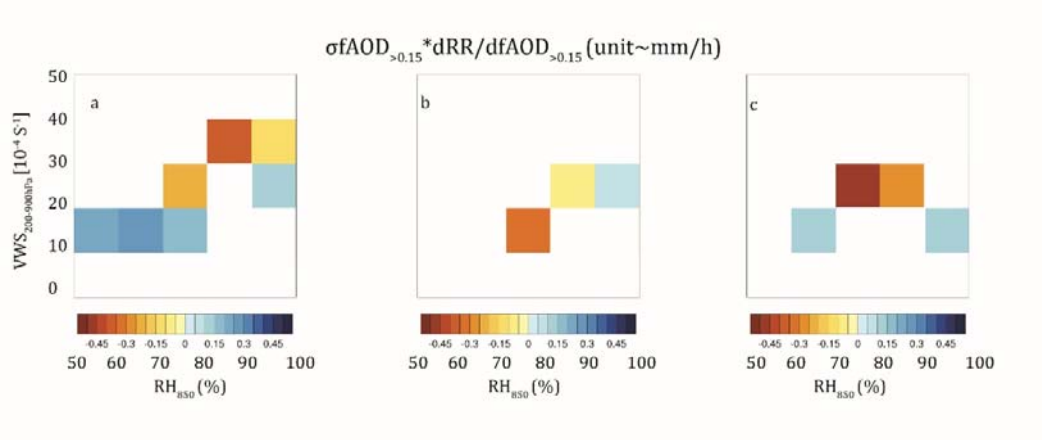

Figure 23. Rate of change of RR (mm/h) for the (a) growing, (b) mature, and (c) decaying MCSs for with 1σ change in fAOD and when RH850 and deep level VWS low level VWS are kept constant. White color denotes either insignificant change (see text) in rain rate reported or number of samples of the bin is less than 20.

With an increase in 1σ f_{AOD}, RR increases (up to 0.27 mm/h) when VWS is low (Figure 23a) and decreases (up to -0.38 mm/h) under moderate to high values of VWS during the growing phase. In this regard, it's important to note that the growing phase of the MCSs we refer to is different from the developing stage of a fresh MCS and aerosols impact may not always be suppressing RR as hypothesized by *Rosenfeld et al.* [2008] for developing systems. This is because the mean lifetime of the MCSs calculated using the ISCCP data set over equatorial South America, south Asia, and equatorial Africa are approximately 21, 120, and 60 hours, respectively. As a result, the MCSs oscillate between three different phases of lifecycle and a growing phase often follows either a decaying or a mature phase. Figure 23b shows that the rate of change of RR with a change of 1σ of f_{AOD} is negative (-0.30 mm/h) at low values of RH_{850} during the mature phase. Again, during the decaying phase (Figure 23c), aerosols suppress RR at a

strong negative rate (up to -0.47mm/h) as VWS increases. The change in RR is weakly positive (~0.13 mm/h) at low values of VWS. These findings clearly show that aerosol impacts on MCSs depend on VWS and humidity and is much apparent when we divide the MCSs according to the phases of their lifecycle.

How does RR suppression by aerosols influence LH release is investigated in Figure 24. The TRMM LH is derived from the surface rain rates for all precipitation categories, precipitation top height, rain rate profiles, and terminal velocities of rain hydrometeors using a cloud resolving model [*Tao et al.*, 2001; *Tao et al.*, 2006] and has been used in many studies [*Barnes et al.*, 2015]. However, because TRMM is largely sensitive to larger precipitation size hydrometeors, its latent heat product is determined by changes of these large hydrometeors. Figure 24b shows that MCSs in polluted environment (f_{AOD}>67‰) release less LH, especially above the freezing level or 5-6 km above the sea-level, during all three phases of the convective lifecycle. This result also confirms that with increasing aerosol concentrations suppresses the formation of larger hydrometeors.

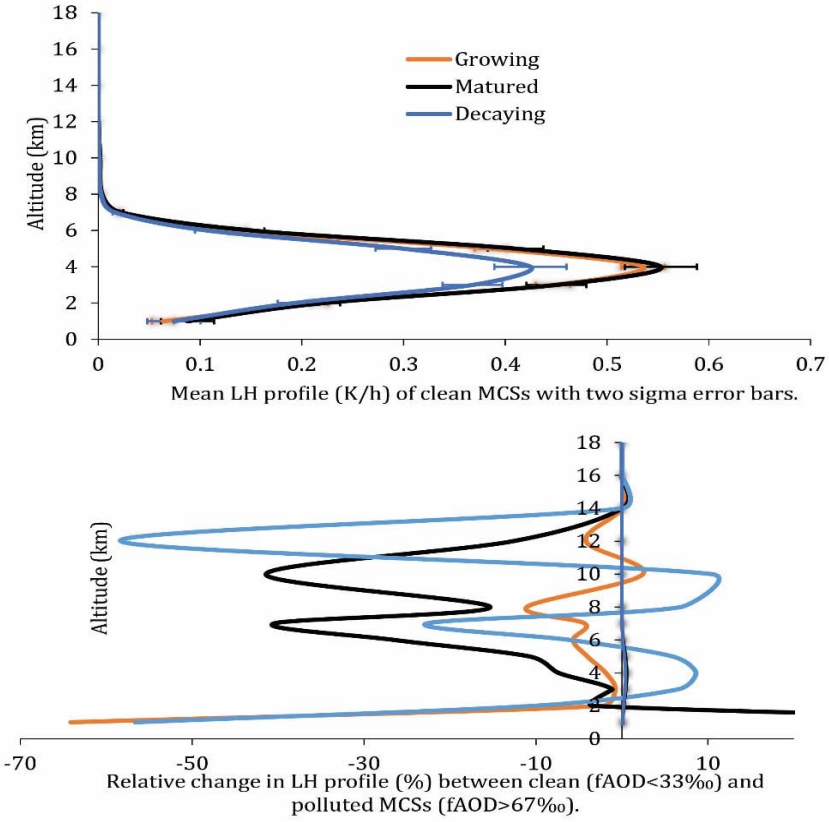

Figure 24. (a) Vertical profiles of mean LH (K/h) of the clean MCSs and (b) relative changes in LH released by the polluted MCSs compared to clean MCSs for the growing, mature, and decaying MCSs.

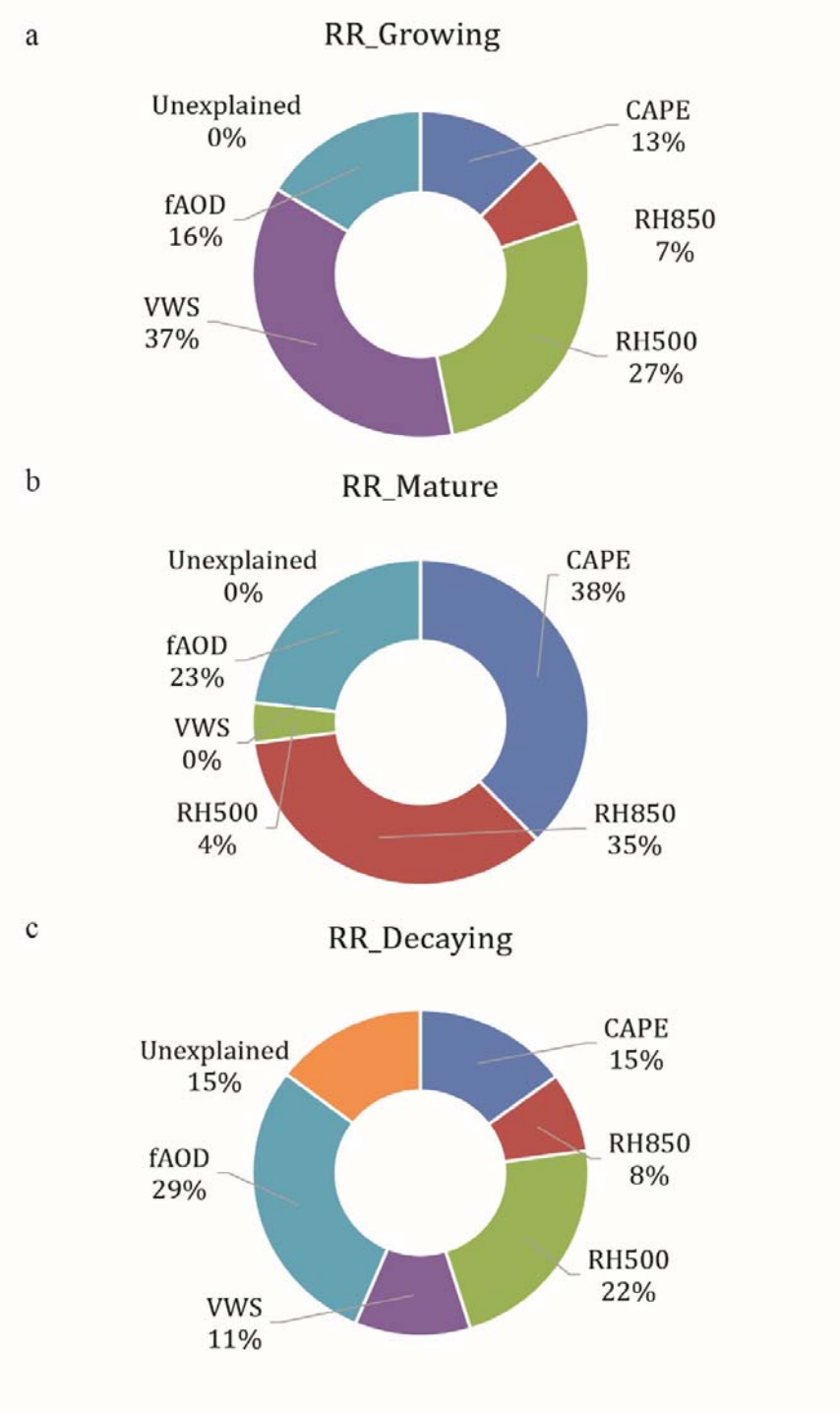

Figure 25. Fraction of variance of LHRR in the binned data explained by the environmental variables and fAOD in the multiple linear regression method associated with the (a) growing, (b) mature, and (c) decaying MCSs.

These results suggest that aerosols mainly suppress the RR during all three phases of the convective lifecycle. As a result, aerosols explain 16%, 23%, and 29% of the RR's variance (Figure 25) in multivariate linear regression during the growing, mature, and decaying phases, respectively. VWS explains 37% and 11% of the RR variance (Figure 25a and 25c) during the growing and decaying phases, respectively. This is because aerosols suppress (enhances) RR during those phases (Figure 23a and 23c) when VWS is moderate to high (low). On the other hand, aerosol's impact on RR depends strongly on humidity rather than VWS during the mature phase (Figure 23b); hence, meteorological parameters related to humidity, such as CAPE (derived from water vapor mixing ratio and temperature), RH_{850}, and RH_{500} explain the largest fraction of variance (~77%) during the mature phase (Figure 23b).

RR suppression by aerosols would lead to an enhancement of IWC of the MCSs. Thus, we analyze the influences of aerosols on total integrated reflectivity (IZ) of the MCSs using CloudSat data set (Figure 26a-26c), and IWC_{216} using the Aura Microwave Limb Sounder (MLS) data set (Figure 27a-27c) at three different stages of lifecycle. Figure 26 shows that an enhancement in IZ occurs during the growing (up to 8 dBZ), mature (up to 11dBZ), and decaying (up to 18 dBZ) phases associated with an increase in 1σ of f_{AOD}. These results are consistent with the findings from Figure 23 and 24 and suggest that aerosols increase MCSs' IWC comprised of bigger-sized ice crystals as observed by CloudSat W-band radar due to a decrease in RR as estimated from TRMM precipitation radar (13.8 GHz; sensitive to large hydrometeors). Since aerosols enhance RR at low values

of VWS (10-20 x 10^{-4} S^{-1}) during the growing phase (Figure 23a), the rate of change of IZ with 1 σ change in f_{AOD} within that range of VWS is either negative (up to -6.87 dBZ) or weakly positive (2.2 dBZ).

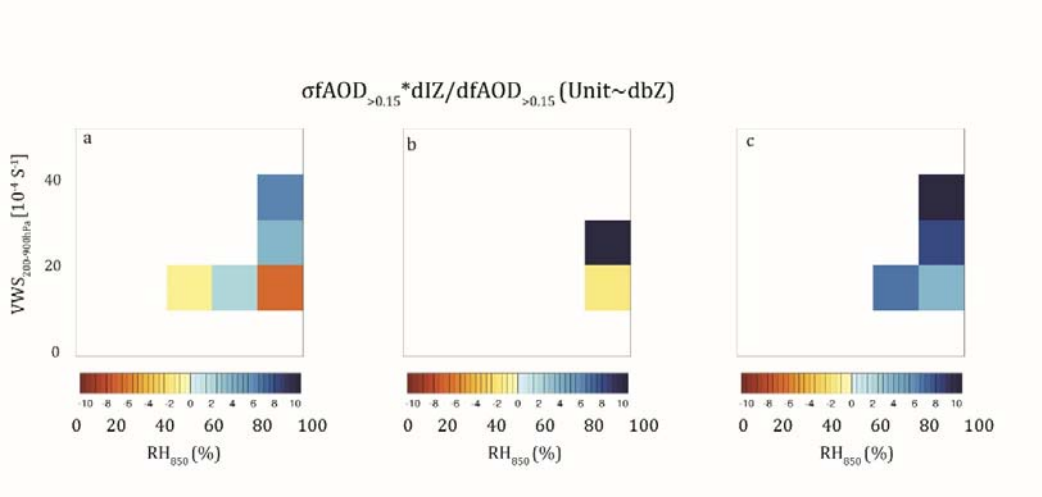

Figure 26. Same as in Figure 19 but for IZ derived from CloudSat datasets for the (a) growing, (b) mature, and (c) decaying MCSs for with 1σ change in fAOD>0.15 and when RH850 and VWS are kept constant.

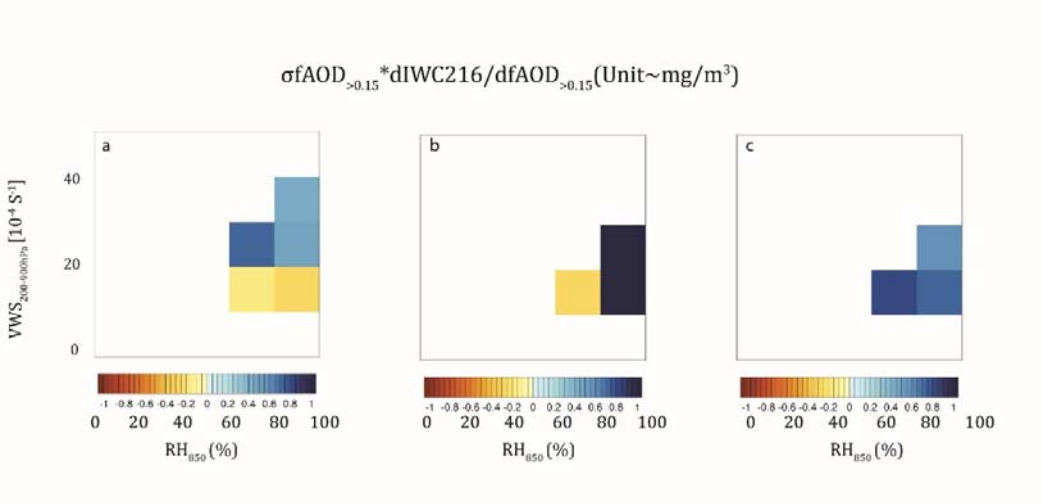

Figure 27. Same as in Figure 19 but for IWC_{216} (mg/m3) derived from Aura MLS datasets for growing, mature, and decaying MCSs for with 1σ change in fAOD>0.15 and when RH_{850} and deep level VWS are kept constant.

IWC comprising of the smaller size ice particles inside anvils of the MCSs also increase. During the growing phase (Figure 27a), IWC_{216} increases up to 0.75 mg/m^3 due to an increase in 1σ of f_{AOD} when the VWS is moderate to high. When aerosol concentration increases, anvil IWC increases by more than $1mg/m^3$ during the mature phase and up to 0.82 mg/m^3 during the decaying phase (Figure 27c). Like IZ (Figure 26 a), IWC_{216} also decreases with increasing aerosol concentrations at low values of VWS (Figure 27a) during the growing phase. This is consistent with an increase of RR with f_{AOD} under the similar meteorological conditions (Figure 23a).

We also look at the variances of IZ and IWC_{216} explained by different meteorological parameters (Figure 26). CAPE is the dominant parameter that explains most of IZ's variance during all three phases of MCS's lifecycle. VWS

explains significant fraction of IZ's variance during the growing (12%), mature (14%), and decaying (12%) phases since an increase in IZ with 1σ change in f_{AOD} intensifies when VWS is high. Meteorological parameters related to humidity explain 82%, 65%, and 53% of IZ's variance during the growing, mature, and decaying phases, respectively. These indicate that a variation in wind speed up to the deep troposphere with a significant amount of buoyancy and humidity is required for the growth of the larger size ice particles. Owing to the dominant influence from the meteorological parameters, aerosol impacts on IZ is significant only during the decaying phase (explains 35% of IZ's variance). Variance of IZ explained by f_{AOD} is low (4% and 3%) during the growing and mature phase.

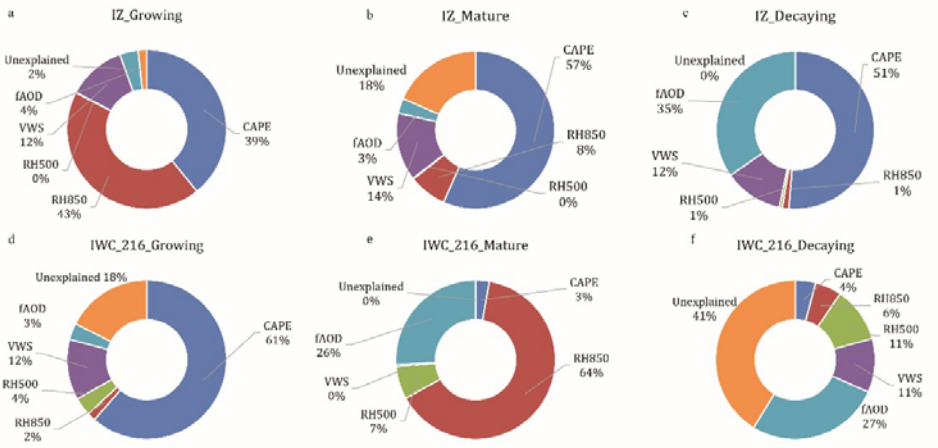

Figure 28. Fraction of variance of IZ derived from CloudSat (a, b, c), and Aura MLS 216 hPa IWC (d, e, f) in the binned data explained by the environmental variables in the multiple regression method associated with the growing, mature, and decaying MCSs.

Meteorological parameters also dominate the fraction of variance of IWC_{216} explained during the growing (67%) and mature (74%) phases, but not during the decaying (21%) phase. f_{AOD} explains 26% and 27% of IWC_{216}'s variance during the mature (δIWC_{216}>1 mg/m^3, Figure 27b) and decaying (δIWC_{216} ~0.82 mg/m^3, Figure 27c) phases. Variance of IWC_{216} as well as IZ explained by f_{AOD} during the growing phases is low (~3 and 4%, respectively, Figures 28a and 28d) because of both the positive (enhancement) and negative (reduction) impacts of aerosols on IWC_{216} (Figure 23a) and IZ (Figure 22a) during that phase.

IZ and IWC_{216} derived from CloudSat and Aura MLS (Figures 26, 27, and 28) and the RR (Figures 22, 23, and 25) and LH (Figure 24) derived from TRMM data set are consistent with each other and show that aerosols suppress the MCSs' precipitation and enhance IWC inside the dense convective as well as stratiform regions.

4.4 Conclusion

This is the first study using a suite of different and multi-year satellite data sets to estimate the relative influence of the aerosols and other meteorological parameters on the strength and precipitation of the MCSs. Our study shows that the different satellites taking measurements of different MCSs are consistent with each other. TRMM 2A25 data set shows that aerosols suppress RR during all three phases of convective lifecycle, especially under the influence of high VWS during the growing and decaying phases and in dry conditions during the mature phase. During the growing phase, f_{AOD} suppresses

RR under high VWS (-0.38 mm/h). During the mature phase RR is suppressed by -0.30 mm/h under dry environmental conditions, whereas during the decaying phase RR is suppressed by -0.47 mm/h, again under the influence of high VWS. As a result, aerosols explain 16%, 23%, and 29% of RR's variance in multiple linear regression during the growing, mature, and decaying phases, respectively. VWS explains 37% and 11% of RR's variance during the growing and decaying phases only because if its influence on aerosols impacts on RR during those phases. Suppression of RR by increasing aerosol concentration leads to a reduced LH release (Figure 24). The suppression of RR by aerosols is due to the fact that they invigorate the MCSs by enhancing IWC of the MCSs. Aerosols increase both IZ and IWC_{216} during the growing, mature, and decay phases (Figure 26 and 27). The impact of aerosols on IZ is intensified when VWS increases from moderate to high values during all three phases of convective lifecycle. Increase in anvil IWC with increasing aerosol concentrations also occurs at high values of VWS during the growing phase (Figure 27a) and VWS explains 12% of its variance (Figure 28d). Hence, our analyses using different satellite data sets are consistent with each other and show that aerosols intensify the MCSs by enhancing the IWC and reducing the rain rates during all three phases of lifecycle.

During the growing phase, aerosols suppress (enhance) RR and intensify (reduce) both IZ and IWC_{216} under moderate to high (low) values of VWS. This suggests that VWS plays an important role in convective development and precipitation during the growing phase. This could be because of the fact that VWS plays important roles in organizing the storms, location of updraft and

downdraft regions, and slantwise accent of the moist air [*Kingsmill and Houze*, 1999; *Moncrieff*, 1978; *Weisman and Rotunno*, 2004] and the MCSs are rooted to the boundary layer during that phase [*R. A. Houze*, 2004]. Detailed analysis using cloud microphysics is required to explore this interdependence between VWS and aerosol concentrations during that phase. However, other meteorological parameters such as CAPE, lower tropospheric humidity, and ambient humidity enhance RR. CAPE, RH850, and RH500 increases RR up to 0.32, 0.3, and 0.2 mm/h, respectively and they explain the largest fraction of RR's variance (47%, 77%, and 45%, respectively) when we consider all the MCSs. Influence of CAPE and lower tropospheric humidity on RR has been documented in many studies [*Robert A. Houze*, 1993; *R. A. Houze*, 2004; *Mapes*, 1993] and *Langhans et al.* [2015] in a recent study showed that entrainment humidity contributes up to one-third to one-half of the surface rainfall.

Our study uses observations from the A-Train based measurements taken approximately at 1:30 am and 1:30 pm local time, whereas the peak strength are achieved by the MCSs during the evening time. Further study using cloud microphysics at three different phases of convective lifecycle is needed to understand aerosol impacts on the MCSs.

Chapter 5

General Conclusions

The findings presented in this dissertation are based on the analyses of multi-year satellite datasets to resolve the relationships between UT ALs surrounding the MCSs and MCS morphology at three different phases of convective lifecycle and to provide a large-scale statistical assessment of the relative influence of aerosols and meteorological conditions (CAPE, RH and VWS) on the rain rates, ice water content, and longevity of the MCSs. To our knowledge, this is the first satellite-based global tropical continental-scale assessment of aerosol-MCS relationships using collocated MCS samples from different satellite observations. These include geostationary ISCCP convective tracking, the A-train constellation, and TRMM, along with MERRA reanalysis products. This dissertation uses multiple datasets from A-Train measurements to obtain aerosol information from CALIPSO, Aqua MODIS, and OMI and cloud information from CloudSat and Aura MLS datasets. Information about rain rates and latent heat are obtained from TRMM measurements.

This dissertation consists of four chapters. Chapter 1 introduces the subject matter and discusses the importance of aerosols in the context of the MCSs and global climate. Chapter 2 focuses on the estimation of the extent of upper tropospheric aerosol layers (UT ALs) surrounding the MCSs and explores the relationships between the extent of such ALs and the morphology of the MCSs located over different tropical continental regions. Such relationships and the variation of UT ALs are derived at three different phases of the convective

lifecycle. Our analysis is based on satellite data collected over equatorial Africa, South Asia, and the Amazon basin between June 2006 and June 2008. We identify substantial variations in the relationships between convective properties and aerosol transport by region and stage of convective development. The most extensive UT ALs over equatorial Africa are associated with mature MCSs, while the most extensive UT ALs over South Asia and the Amazon are associated with growing MCSs. Convective aerosol transport over the Amazon is weaker than that observed over the other two regions despite similar transport frequencies, likely due to the smaller sizes and shorter mean lifetimes of MCSs over the Amazon.

Variations in UT ALs in the vicinity of tropical MCSs are primarily explained by variations in the horizontal sizes of the associated MCSs and are largely unrelated to aerosol loading in the lower troposphere. In addition, we identify potentially important relationships with the number of convective cores, vertical wind shear, and convective fraction during the growing and mature stages of MCS development. Relationships between convective properties and aerosol transport are relatively weak during the decaying stage of convective development.

Our analysis indicates that VWS may play an important role in aerosol transport during the growing stage. The VWS coefficient appears to act as a surrogate for regional variability when all regions are considered together, but AL extent over South Asia increases significantly with increasing VWS ($R = 0.30$, $p = 0.03$). A positive relationship between VWS and aerosol transport is

physically plausible, given the close relationship between convective and boundary layer properties during the growing stage and the potential for VWS to enhance convective aerosol transport by establishing separate regions for updrafts and downdrafts. Our statistical model results further indicate that mature systems with similar sizes will typically produce more extensive ALs when the CF is larger. This positive dependence on CF is only observed for mature systems. By contrast, the extent of ALs associated with decaying systems is negatively correlated with aerosol optical depth (AOD). Our results provide an interpretive framework for devising and evaluating numerical model experiments that examine relationships between convective properties and ALs in the upper troposphere.

Chapter 3 focuses on the relative influence of meteorological conditions and aerosols on the lifetime of the MCSs. Using collocated measurements from geostationary and polar-orbital satellites over tropical South America, equatorial Africa, and South Asia, we provide a large-scale statistical assessment of the relative influence of aerosols and meteorological conditions on the lifetime of the MCSs. Since we use TRMM, which orbits the Earth on a different track and at a different time compared to the A-Train satellites, we are able to extend our collocation period from January 2003 to June 2008 in order to have a larger number of samples. Our results show that globally, over tropical continental regions, MCSs' lifetime increases by 3-24 hours with ambient aerosol optical depth (AOD) only under high relative humidity (RH) in the lower troposphere and moderate vertical wind shear (VWS) in the deep troposphere. However, the

influence of aerosols is not as strong as that of convective available potential energy (12-36 hours), RH (6-30 hours) and deep tropospheric VWS (3-30 hours), which explain 18-22%, 44-62%, and 8-18% of the total variance of MCSs' lifetime, respectively. AOD explains up to 19% of the total variance of MCSs' lifetime mainly during the decaying phase. This result is physically consistent with the variation of the MCSs' ice water content inside their convective cores and anvils, which peak during the decaying phase (35% and 27%, respectively).

The effect of aerosols on MCSs' lifetime varies between continents. AOD appears to explain up to 20%-22% of the total variance in MCS lifetime over equatorial South America compared to 8% over equatorial Africa. Aerosols over the Indian Ocean can explain 14% of the total variance in MCSs' lifetime over South Asia because most MCSs form and develop over the ocean. Using AOD>0.3 as a threshold did not produce any observable difference in terms of aerosol impacts on MCSs. We also observe that the impacts from the low level VWS are poorly correlated with MCS lifetime as compared to deep level VWS.

To our knowledge, this is the first satellite based global tropical continental scale assessment of the relative roles of the meteorological conditions and aerosols using large samples of the MCSs. This study provides a global tropical assessment on the relative influences of aerosols and meteorological conditions on MCCs' lifetime and the mutual dependence of these influences. It also shows how aerosols influence on the cloud ice and lifetime of the MCSs vary within their lifecycle and between different tropical continents ranging from humid equatorial South America during wet season and big

monsoonal systems over South Asia to relatively dry equatorial Africa with high aerosol loading. In doing so, this work has also advanced our capability to evaluate whether or not aerosols could increase convective lifetime on climate scale and what are the favorable meteorological conditions for aerosol to affect the lifetime of the MCSs.

These regional differences in the aerosol impact appear to be linked to different meteorological conditions, but the underlying physical processes and influences of varying aerosol types require further investigation in the future. Moreover, we are unable to observe the microphysical changes associated with MCS convections at different phases of convective lifetime and over different geographic regions. To understand the influence from different types of aerosols, aircraft observations and ground-based measurements can be used in the future.

The focus of chapter 4 is to estimate the relative influence of aerosols and other meteorological conditions on rain rates (RR), cloud ice water content (IWC), and latent heat (LH) profiles through the life cycle of large mesoscale convective systems (MCSs) over the tropical South America, Africa and South Asia for the period of January 2003- June2008 using a suite of co-located geostationary and polar orbital satellite measurements. Under similar lower tropospheric humidity (RH_{850}) and vertical wind shear (VWS) conditions, an increase in aerosol concentrations tends to suppress RR and LH, but intensify cloud ice both in the convective cores and anvils through convective lifecycle. In particular, an increase of aerosol concentrations by one standard deviation can

suppress RR during the entire convective lifecycle, especially during the growing phase and decay phases, at the rate of -0.38 mm/h and -0.47 mm/h, respectively, when VWS is high, and during the mature phase when the humidity is low at the rate of -0.30 mm/h. Consequently, LH released by the MCSs decreases also because it is dominated by the observation of RR by TRMM. Aerosols explain 16%, 23%, and 29% of RR's variance during the growing, mature and decaying phases, respectively, over the global tropical continents, as estimated by a multiple linear regression method.

By comparison, increasing convective available potential energy (CAPE) and humidity (RH_{850} or lower tropospheric humidity and RH_{500} or ambient humidity) explain 47%, 77%, and 45% of the total RR's variance during the growing, mature, and decaying phases, respectively. The rate of enhance RR with CAPE, RH_{850} and RH_{500} is up to 0.32 mm/h, 0.3 mm/h, and 0.3 mm/h, respectively. Different studies have documented the influence of CAPE and lower tropospheric humidity on RR [*Robert A. Houze*, 1993; *R. A. Houze*, 2004; *Mapes*, 1993]. *Langhans et al.* [2015] in a recent study showed that entrainment humidity contributes up to one-third to one-half of the surface rainfall. Our findings are consistent with the previous findings that stronger buoyancy and higher amount of moisture would enhance the RR, whereas aerosols would suppress RR and intensify the MCSs by enhancing their IWC. VWS explains 37% and 11% of RR's variance during the growing and decaying phases only because if its influence on aerosols impacts on RR during those phases. Strong VWS contributes to aerosol impacts by suppressing RR and enhancing IWC. On the

other hand, IWC inside the core and anvil regions of the MCSs decreases and RR increases with increasing aerosols concentrations when VWS is low. This might be due to the fact that VWS plays an important role in organizing relative position of the updraft and downdraft regions, tilting of the systems, and slantwise ascent of the moisture inside the MCSs [*Kingsmill and Houze*, 1999; *Moncrieff*, 1978; *Weisman and Rotunno*, 2004], especially during the growing phase when the storms are rooted to their boundary layer [*R. A. Houze*, 2004].

IWC of the MCSs increases during all three phases of convective lifecycle, as expected from the increase of smaller cloud particle with aerosols and reduced RR. With increasing aerosol concentrations, total integrated reflectivity of the larger cloud ice particles, as detected by CloudSat, increases up to 8, 11, and 18 dBZ in the convective core regions during the growing, mature and decaying phases, respectively. The IWC inside anvils, comprised of smaller-sized ice particles as detected by Aura MLS, also increases by 0.72, 1.41, and 0.82 mg/m^3 during the growing, mature, and decaying phases, respectively.

Using satellite data sets over global tropical continents, this study provides an assessment of the relative influences of the meteorological conditions and aerosols on MCS rain rate and IWC. It also show how aerosol impacts on MCS rain rate and IWC vary at different phases of the convective lifetime and how meteorological parameters influence that. Hence, this work has also advanced our capability to evaluate whether or not aerosols could invigorate the MCSs.

I use observations from the A-Train based measurements that are taken approximately at 1:30 am and 1:30 pm local time, whereas the peak strength are achieved by the MCSs during the evening time. Further study using cloud microphysics at three different phases of convective lifecycle is needed to understand aerosol impacts on the MCSs. Use of ground-based measurements could provide detailed explanation of these findings and can also investigate the same at the peak convective strength.

This dissertation focused on aerosol-MCS relationships over the tropical continents. So far, we have investigated the influence of f_{AOD}, RH, CAPE, and VWS on the MCSs. However, the MCSs over the extra-tropics are frontal and baroclinic in nature; hence, temperature gradient might be another important meteorological parameter that can have a significant influence on the MCSs. Understanding the transport of aerosols along the frontal boundary of extra-topical clouds and the influence of aerosols and other meteorological parameters on MCSs will be the focus of future work. In addition, I intend to focus on the relative influences of those meteorological parameters and aerosols on the mechanism of self-aggregation of convections [*Wing and Emanuel*, 2014] using both satellite and ground-based measurements of the Department of Energy Atmospheric Radiation Measurement (ARM) datasets.

References

Ackerman, A. S., O. B. Toon, D. E. Stevens, A. J. Heymsfield, V. Ramanathan, and E. J. Welton (2000), Reduction of tropical cloudiness by soot, *Science*, *288*(5468), 1042-1047.

Albrecht, B. A. (1989), Aerosols, Cloud Microphysics, and Fractional Cloudiness, *Science*, *245*(4923), 1227-1230.

Altaratz, O., I. Koren, L. A. Remer, and E. Hirsch (2014), Review: Cloud invigoration by aerosols-Coupling between microphysics and dynamics, *Atmos Res*, *140*, 38-60.

Andreae, M. O., D. Rosenfeld, P. Artaxo, A. A. Costa, G. P. Frank, K. M. Longo, and M. A. F. Silva-Dias (2004), Smoking rain clouds over the Amazon, *Science*, *303*(5662), 1337-1342.

Barnes, H. C., M. D. Zuluaga, and R. A. Houze (2015), Latent heating characteristics of the MJO computed from TRMM Observations, *J Geophys Res-Atmos*, *120*(4), 1322-1334.

Bell, T. L., D. Rosenfeld, K. M. Kim, J. M. Yoo, M. I. Lee, and M. Hahnenberger (2008), Midweek increase in US summer rain and storm heights suggests air pollution invigorates rainstorms, *J Geophys Res-Atmos*, *113*(D2).

Bhowmik, S. K. R., S. Sen Roy, and P. K. Kundu (2008), Analysis of large-scale conditions associated with convection over the Indian monsoon region, *Int J Climatol*, *28*(6), 797-821.

Bister, M., and M. Kulmala (2011), Anthropogenic aerosols may have increased upper tropospheric humidity in the 20th century, *Atmos Chem Phys*, *11*(9), 4577-4586.

Chakraborty, S., R. Fu, J. S. Wright, and S. T. Massie (2015), Relationships between convective structure and transport of aerosols to the upper troposphere deduced from satellite observations, *J Geophys Res-Atmos*, *120*(13), 6515-6536.

Charlson, R. J., S. E. Schwartz, J. M. Hales, R. D. Cess, J. A. Coakley, J. E. Hansen, and D. J. Hofmann (1992), Climate Forcing by Anthropogenic Aerosols, *Science*, *255*(5043), 423-430.

Chu, D. A., Y. J. Kaufman, L. A. Remer, D. Tanre, and M. J. Jeong (2003), Multi-year MODIS observation of global aerosols from EOS Terra/Aqua satellites: Validation, variability, and application, *Int Geosci Remote Se*, 863-865.

Chu, D. A., Y. J. Kaufman, C. Ichoku, L. A. Remer, D. Tanre, and B. N. Holben (2002), Validation of MODIS aerosol optical depth retrieval over land, *Geophys Res Lett*, *29*(12).

Chung, C. E., and V. Ramanathan (2004), Aerosol loading over the Indian Ocean and its possible impact on regional climate, *Indian J Mar Sci*, *33*(1), 40-55.

Chylek, P., M. K. Dubey, U. Lohmann, V. Ramanathan, Y. J. Kaufman, G. Lesins, J. Hudson, G. Altmann, and S. Olsen (2006), Aerosol indirect effect over the Indian Ocean, *Geophys Res Lett*, *33*(6).

Cotton, W. R., and R. A. Anthes (1989), *Storm and cloud dynamics*, xii, 883 p. pp., Academic Press, San Diego.

Cotton, W. R., G. D. Alexander, R. Hertenstein, R. L. Walko, R. L. McAnelly, and M. Nicholls (1995), Cloud venting - A review and some new global annual estimates, *Earth-Sci Rev*, *39*(3-4), 169-206.
Crutzen, P. J., and M. O. Andreae (1990), Biomass Burning in the Tropics - Impact on Atmospheric Chemistry and Biogeochemical Cycles, *Science*, *250*(4988), 1669-1678.
de Boer, G., T. Hashino, and G. J. Tripoli (2010), Ice nucleation through immersion freezing in mixed-phase stratiform clouds: Theory and numerical simulations, *Atmos Res*, *96*(2-3), 315-324.
Del Genio, A. D., and J. B. Wu (2010), The Role of Entrainment in the Diurnal Cycle of Continental Convection, *J Climate*, *23*(10), 2722-2738.
Di Pierro, M., L. Jaegle, and T. L. Anderson (2011), Satellite observations of aerosol transport from East Asia to the Arctic: three case studies, *Atmos Chem Phys*, *11*(5), 2225-2243.
Ekman, A. M. L., C. Wang, J. Strom, and R. Krejci (2006), Explicit simulation of aerosol physics in a cloud-resolving model: Aerosol transport and processing in the free troposphere, *J Atmos Sci*, *63*(2), 682-696.
Ervens, B., G. Feingold, G. J. Frost, and S. M. Kreidenweis (2004), A modeling study of aqueous production of dicarboxylic acids: 1. Chemical pathways and speciated organic mass production, *J Geophys Res-Atmos*, *109*(D15).
Fan, J. W., R. Y. Zhang, G. H. Li, and W. K. Tao (2007), Effects of aerosols and relative humidity on cumulus clouds, *J Geophys Res-Atmos*, *112*(D14).
Fan, J. W., L. R. Leung, D. Rosenfeld, Q. Chen, Z. Q. Li, J. Q. Zhang, and H. R. Yan (2013), Microphysical effects determine macrophysical response for aerosol impacts on deep convective clouds, *P Natl Acad Sci USA*, *110*(48), E4581-E4590.
Fan, J. W., T. L. Yuan, J. M. Comstock, S. Ghan, A. Khain, L. R. Leung, Z. Q. Li, V. J. Martins, and M. Ovchinnikov (2009), Dominant role by vertical wind shear in regulating aerosol effects on deep convective clouds, *J Geophys Res-Atmos*, *114*.
Fan, S. M., L. W. Horowitz, H. Levy, and W. J. Moxim (2004), Impact of air pollution on wet deposition of mineral dust aerosols, *Geophys Res Lett*, *31*(2).
Froyd, K. D., D. M. Murphy, T. J. Sanford, D. S. Thomson, J. C. Wilson, L. Pfister, and L. Lait (2009), Aerosol composition of the tropical upper troposphere, *Atmos Chem Phys*, *9*(13), 4363-4385.
Fu, R., Y. L. Hu, J. S. Wright, J. H. Jiang, R. E. Dickinson, M. X. Chen, M. Filipiak, W. G. Read, J. W. Waters, and D. L. Wu (2006), Short circuit of water vapor and polluted air to the global stratosphere by convective transport over the Tibetan Plateau, *P Natl Acad Sci USA*, *103*(15), 5664-5669.
Glaccum, R. A., and J. M. Prospero (1980), Saharan Aerosols over the Tropical North-Atlantic - Mineralogy, *Mar Geol*, *37*(3-4), 295-321.
Gunn, R., and B. B. Phillips (1957), An Experimental Investigation of the Effect of Air Pollution on the Initiation of Rain, *J Meteorol*, *14*(3), 272-280.
Harrison, S. J. (1992), Fundamentals of Weather and Climate - Mcilveen,R, *Scot Geogr Mag*, *108*(2), 133-133.
Heald, C. L., et al. (2011), Exploring the vertical profile of atmospheric organic aerosol: comparing 17 aircraft field campaigns with a global model, *Atmos Chem Phys*, *11*(24), 12673-12696.

Heese, B., and M. Wiegner (2008), Vertical aerosol profiles from Raman polarization lidar observations during the dry season AMMA field campaign, *J Geophys Res-Atmos*, *113*(D17).
Heymsfield, A. J., C. Schmitt, and A. Bansemer (2013), Ice Cloud Particle Size Distributions and Pressure-Dependent Terminal Velocities from In Situ Observations at Temperatures from 0 degrees to-86 degrees C, *J Atmos Sci*, *70*(12), 4123-4154.
Hodson, M. C. (1986), Raindrop Size Distribution, *J Clim Appl Meteorol*, *25*(7), 1070-1074.
Hofmann, D. J. (1990), Increase in the Stratospheric Background Sulfuric-Acid Aerosol Mass in the Past 10 Years, *Science*, *248*(4958), 996-1000.
Hoose, C., U. Lohmann, R. Erdin, and I. Tegen (2008), The global influence of dust mineralogical composition on heterogeneous ice nucleation in mixed-phase clouds, *Environ Res Lett*, *3*(2).
Houze, R. A. (1993), *Cloud dynamics*, xxix, 573 p. pp., Academic Press, San Diego, Calif.
Houze, R. A. (2004), Mesoscale convective systems, *Rev Geophys*, *42*(4).
Houze, R. A., K. L. Rasmussen, M. D. Zuluaga, and S. R. Brodzik (2015), The variable nature of convection in the tropics and subtropics: A legacy of 16years of the Tropical Rainfall Measuring Mission satellite, *Rev Geophys*, *53*(3), 994-1021.
Huang, L., R. Fu, and J. H. Jiang (2014), Impacts of fire emissions and transport pathways on the interannual variation of CO in the tropical upper troposphere, *Atmos Chem Phys*, *14*(8), 4087-4099.
Huang, L., R. Fu, J. H. Jiang, J. S. Wright, and M. Luo (2012), Geographic and seasonal distributions of CO transport pathways and their roles in determining CO centers in the upper troposphere, *Atmos Chem Phys*, *12*(10), 4683-4698.
Huang, L., J. H. Jiang, J. L. Tackett, H. Su, and R. Fu (2013), Seasonal and diurnal variations of aerosol extinction profile and type distribution from CALIPSO 5-year observations, *J Geophys Res-Atmos*, *118*(10), 4572-4596.
Huffman, G. J., R. F. Adler, D. T. Bolvin, G. J. Gu, E. J. Nelkin, K. P. Bowman, Y. Hong, E. F. Stocker, and D. B. Wolff (2007), The TRMM multisatellite precipitation analysis (TMPA): Quasi-global, multiyear, combined-sensor precipitation estimates at fine scales, *J Hydrometeorol*, *8*(1), 38-55.
Ichoku, C., L. A. Remer, Y. J. Kaufman, R. Levy, D. A. Chu, D. Tanre, and B. N. Holben (2003), MODIS observation of aerosols and estimation of aerosol radiative forcing over southern Africa during SAFARI 2000, *J Geophys Res-Atmos*, *108*(D13).
Ito, A., A. Ito, and H. Akimoto (2007), Seasonal and interannual variations in CO and BC emissions from open biomass burning in Southern Africa during 1998-2005, *Global Biogeochem Cy*, *21*(2).
Jiang, H. L., H. W. Xue, A. Teller, G. Feingold, and Z. Levin (2006), Aerosol effects on the lifetime of shallow cumulus, *Geophys Res Lett*, *33*(14).
Jiang, J. H., H. Su, S. T. Massie, P. R. Colarco, M. R. Schoeberl, and S. Platnick (2009), Aerosol-CO relationship and aerosol effect on ice cloud particle size: Analyses from Aura Microwave Limb Sounder and Aqua Moderate Resolution Imaging Spectroradiometer observations, *J Geophys Res-Atmos*, *114*.

Jiang, J. H., H. Su, M. R. Schoeberl, S. T. Massie, P. Colarco, S. Platnick, and N. J. Livesey (2008), Clean and polluted clouds: Relationships among pollution, ice clouds, and precipitation in South America, *Geophys Res Lett*, *35*(14).
Kacenelenbogen, M., M. A. Vaughan, J. Redemann, R. M. Hoff, R. R. Rogers, R. A. Ferrare, P. B. Russell, C. A. Hostetler, J. W. Hair, and B. N. Holben (2011), An accuracy assessment of the CALIOP/CALIPSO version 2/version 3 daytime aerosol extinction product based on a detailed multi-sensor, multi-platform case study, *Atmos Chem Phys*, *11*(8), 3981-4000.
Kato, S., et al. (2011), Improvements of top-of-atmosphere and surface irradiance computations with CALIPSO-, CloudSat-, and MODIS-derived cloud and aerosol properties, *J Geophys Res-Atmos*, *116*.
Kaufman, Y. J., D. Tanre, and O. Boucher (2002), A satellite view of aerosols in the climate system, *Nature*, *419*(6903), 215-223.
Keil, A., and J. M. Haywood (2003), Solar radiative forcing by biomass burning aerosol particles during SAFARI 2000: A case study based on measured aerosol and cloud properties, *J Geophys Res-Atmos*, *108*(D13).
Khain, A., and A. Pokrovsky (2004), Simulation of effects of atmospheric aerosols on deep turbulent convective clouds using a spectral microphysics mixed-phase cumulus cloud model. Part II: Sensitivity study, *J Atmos Sci*, *61*(24), 2983-3001.
Khain, A., D. Rosenfeld, and A. Pokrovsky (2005), Aerosol impact on the dynamics and microphysics of deep convective clouds, *Q J Roy Meteor Soc*, *131*(611), 2639-2663.
Khain, A., A. Pokrovsky, M. Pinsky, A. Seifert, and V. Phillips (2004), Simulation of effects of atmospheric aerosols on deep turbulent convective clouds using a spectral microphysics mixed-phase cumulus cloud model. Part I: Model description and possible applications, *J Atmos Sci*, *61*(24), 2963-2982.
Khain, A. P., N. BenMoshe, and A. Pokrovsky (2008), Factors determining the impact of aerosols on surface precipitation from clouds: An attempt at classification, *J Atmos Sci*, *65*(6), 1721-1748.
Kilroy, G., R. K. Smith, and U. Wissmeier (2014), Tropical convection: the effects of ambient vertical and horizontal vorticity, *Q J Roy Meteor Soc*, *140*(682), 1756-1770.
Kingsmill, D. E., and R. A. Houze (1999), Kinematic characteristics of air flowing into and out of precipitating convection over the west Pacific warm pool: An airborne Doppler radar survey, *Q J Roy Meteor Soc*, *125*(556), 1165-1207.
Knippertz, P., M. Tesche, B. Heinold, K. Kandler, C. Toledano, and M. Esselborn (2011), Dust mobilization and aerosol transport from West Africa to Cape Verde-a meteorological overview of SAMUM-2, *Tellus B*, *63*(4), 430-447.
Koffi, B., et al. (2012), Application of the CALIOP layer product to evaluate the vertical distribution of aerosols estimated by global models: AeroCom phase I results, *J Geophys Res-Atmos*, *117*.
Koren, I., G. Feingold, and L. A. Remer (2010a), The invigoration of deep convective clouds over the Atlantic: aerosol effect, meteorology or retrieval artifact?, *Atmos Chem Phys*, *10*(18), 8855-8872.
Koren, I., J. V. Martins, L. A. Remer, and H. Afargan (2008), Smoke invigoration versus inhibition of clouds over the Amazon, *Science*, *321*(5891), 946-949.

Koren, I., Y. J. Kaufman, D. Rosenfeld, L. A. Remer, and Y. Rudich (2005), Aerosol invigoration and restructuring of Atlantic convective clouds, *Geophys Res Lett*, *32*(14).
Koren, I., L. A. Remer, O. Altaratz, J. V. Martins, and A. Davidi (2010b), Aerosol-induced changes of convective cloud anvils produce strong climate warming, *Atmos Chem Phys*, *10*(10), 5001-5010.
L'Ecuyer, T. S., and J. H. Jiang (2010), Touring the atmosphere aboard the A-Train, *Phys Today*, *63*(7), 36-41.
Lacis, A., J. Hansen, and M. Sato (1992), Climate Forcing by Stratospheric Aerosols, *Geophys Res Lett*, *19*(15), 1607-1610.
Langenberg, H. (2005), Inside information, *Nature*, *437*(7058), 468-469.
Langhans, W., K. Yeo, and D. M. Romps (2015), Lagrangian Investigation of the Precipitation Efficiency of Convective Clouds, *J Atmos Sci*, *72*(3), 1045-1062.
Lee, J., J. Kim, P. Yang, and N. C. Hsu (2012), Improvement of aerosol optical depth retrieval from MODIS spectral reflectance over the global ocean using new aerosol models archived from AERONET inversion data and tri-axial ellipsoidal dust database, *Atmos Chem Phys*, *12*(15), 7087-7102.
Lee, S. S. (2012), Effect of Aerosol on Circulations and Precipitation in Deep Convective Clouds, *J Atmos Sci*, *69*(6), 1957-1974.
Lee, S. S., W. K. Tao, and C. H. Jung (2014), Aerosol Effects on Instability, Circulations, Clouds, and Precipitation, *Adv Meteorol*.
Levy, R. C., L. A. Remer, R. G. Kleidman, S. Mattoo, C. Ichoku, R. Kahn, and T. F. Eck (2010), Global evaluation of the Collection 5 MODIS dark-target aerosol products over land, *Atmos Chem Phys*, *10*(21), 10399-10420.
Li, W. H., and R. Fu (2006), Influence of cold air intrusions on the wet season onset over Amazonia, *J Climate*, *19*(2), 257-275.
Li, X. W., W. K. Tao, H. Masunaga, G. J. Gu, and X. P. Zeng (2013), Aerosol Effects on Cumulus Congestus Population over the Tropical Pacific: A Cloud-Resolving Modeling Study, *J Meteorol Soc Jpn*, *91*(6), 817-833.
Li, Z. Q., F. Niu, J. W. Fan, Y. G. Liu, D. Rosenfeld, and Y. N. Ding (2011), Long-term impacts of aerosols on the vertical development of clouds and precipitation, *Nat Geosci*, *4*(12), 888-894.
Lin, J. C., T. Matsui, R. A. Pielke, and C. Kummerow (2006), Effects of biomass-burning-derived aerosols on precipitation and clouds in the Amazon Basin: a satellite-based empirical study, *J Geophys Res-Atmos*, *111*(D19).
Lindsey, D. T., and M. Fromm (2008), Evidence of the cloud lifetime effect from wildfire-induced thunderstorms, *Geophys Res Lett*, *35*(22).
Liu, J. J., B. Chen, and J. P. Huang (2014), Discrimination and validation of clouds and dust aerosol layers over the Sahara desert with combined CALIOP and IIR measurements, *J Meteorol Res-Prc*, *28*(2), 185-198.
Liu, Z. Y., R. Kuehn, M. Vaughan, D. Winker, K. Powell, C. Hostetler, L. Poole, and M. McGill (2004), A cloud-aerosol discrimination algorithm for calipso lidar observations: Algorithm tests, *Esa Sp Publ*, *561*, 987-990.
Liu, Z. Y., M. Vaughan, D. Winker, C. Kittaka, B. Getzewich, R. Kuehn, A. Omar, K. Powell, C. Trepte, and C. Hostetler (2009), The CALIPSO Lidar Cloud and Aerosol Discrimination: Version 2 Algorithm and Initial Assessment of Performance, *J Atmos Ocean Tech*, *26*(7), 1198-1213.

Livesey, N. J., J. A. Logan, M. L. Santee, J. W. Waters, R. M. Doherty, W. G. Read, L. Froidevaux, and J. H. Jiang (2013), Interrelated variations of O-3, CO and deep convection in the tropical/subtropical upper troposphere observed by the Aura Microwave Limb Sounder (MLS) during 2004-2011, *Atmos Chem Phys*, *13*(2), 579-598.
Livingston, J. M., et al. (2014), Comparison of MODIS 3 km and 10 km resolution aerosol optical depth retrievals over land with airborne sunphotometer measurements during ARCTAS summer 2008, *Atmos Chem Phys*, *14*(4), 2015-2038.
Lohmann, U., and J. Feichter (2005), Global indirect aerosol effects: a review, *Atmos Chem Phys*, *5*, 715-737.
Machado, L. A. T., W. B. Rossow, R. L. Guedes, and A. W. Walker (1998), Life cycle variations of mesoscale convective systems over the Americas, *Mon Weather Rev*, *126*(6), 1630-1654.
Maddox, R. A., C. F. Chappell, and L. R. Hoxit (1979), Synoptic and Meso-Alpha Scale Aspects of Flash Flood Events, *B Am Meteorol Soc*, *60*(2), 115-123.
Mapes, B. E. (1993), Gregarious Tropical Convection, *J Atmos Sci*, *50*(13), 2026-2037.
Marshall, J. S., and W. M. Palmer (1948), The Distribution of Raindrops with Size, *J Meteorol*, *5*(4), 165-166.
Martin, J. J., and H. R. Pruppacher (1978), Scavenging of Aerosol-Particles by Falling Ice Hydrometeors, *B Am Meteorol Soc*, *59*(9), 1244-1244.
Marwitz, J. (1972), Precipitation Efficiency of Thunderstorms in High Plains, *B Am Meteorol Soc*, *53*(3), 321-&.
Massie, S. T., A. Heymsfield, C. Schmitt, D. Muller, and P. Seifert (2007), Aerosol indirect effects as a function of cloud top pressure, *J Geophys Res-Atmos*, *112*(D6).
Matrosov, S. Y. (2007), Potential for attenuation-based estimations of rainfall rate from CloudSat, *Geophys Res Lett*, *34*(5).
Matrosov, S. Y. (2009a), A Method to Estimate Vertically Integrated Amounts of Cloud Ice and Liquid and Mean Rain Rate in Stratiform Precipitation from Radar and Auxiliary Data, *J Appl Meteorol Clim*, *48*(7), 1398-1410.
Matrosov, S. Y. (2009b), Simultaneous estimates of cloud and rainfall parameters in the atmospheric vertical column above the Atmospheric Radiation Measurement Program southern Great Plains site, *J Geophys Res-Atmos*, *114*.
Matrosov, S. Y., K. A. Clark, and D. E. Kingsmill (2007), A polarimetric radar approach to identify rain, melting-layer, and snow regions for applying corrections to vertical profiles of reflectivity, *J Appl Meteorol Clim*, *46*(2), 154-166.
McComiskey, A., and G. Feingold (2008), Quantifying error in the radiative forcing of the first aerosol indirect effect, *Geophys Res Lett*, *35*(2).
Menon, S., J. Hansen, L. Nazarenko, and Y. F. Luo (2002), Climate effects of black carbon aerosols in China and India, *Science*, *297*(5590), 2250-2253.
Mohler, O., C. Linke, H. Saathoff, M. Schnaiter, R. Wagner, A. Mangold, M. Kramer, and U. Schurath (2005), Ice nucleation on flame soot aerosol of different organic carbon content, *Meteorol Z*, *14*(4), 477-484.
Moncrieff, M. W. (1978), Dynamical Structure of 2-Dimensional Steady Convection in Constant Vertical Shear, *Q J Roy Meteor Soc*, *104*(441), 543-567.

Mullendore, G. L., A. J. Homann, K. Bevers, and C. Schumacher (2009), Radar reflectivity as a proxy for convective mass transport, *J Geophys Res-Atmos*, *114*.
Muller, D., I. Mattis, U. Wandinger, A. Ansmann, D. Althausen, and A. Stohl (2005), Raman lidar observations of aged Siberian and Canadian forest fire smoke in the free troposphere over Germany in 2003: Microphysical particle characterization, *J Geophys Res-Atmos*, *110*(D17).
Myhre, G., T. F. Berglen, C. E. L. Myhre, and I. S. A. Isaksen (2004), The radiative effect of the anthropogenic influence on the stratospheric sulfate aerosol layer, *Tellus B*, *56*(3), 294-299.
Nakata, M., I. Sano, S. Mukai, and B. N. Holben (2013), Spatial and Temporal Variations of Atmospheric Aerosol in Osaka, *Atmosphere-Basel*, *4*(2), 157-168.
Okita, T., H. Hara, and N. Fukuzaki (1996), Measurements of atmospheric SO2 and SO42-, and determination of the wet scavenging coefficient of sulfate aerosols for the winter monsoon season over the Sea of Japan, *Atmos Environ*, *30*(22), 3733-3739.
Omar, A. H., et al. (2009), The CALIPSO Automated Aerosol Classification and Lidar Ratio Selection Algorithm, *J Atmos Ocean Tech*, *26*(10), 1994-2014.
Petersen, W. A., and S. A. Rutledge (2001), Regional variability in tropical convection: Observations from TRMM, *J Climate*, *14*(17), 3566-3586.
Petersen, W. A., R. Fu, M. X. Chen, and R. Blakeslee (2006), Intraseasonal forcing of convection and lightning activity in the southern Amazon as a function of cross-equatorial flow, *J Climate*, *19*(13), 3180-3196.
Pratt, K. A., A. J. Heymsfield, C. H. Twohy, S. M. Murphy, P. J. DeMott, J. G. Hudson, R. Subramanian, Z. E. Wang, J. H. Seinfeld, and K. A. Prather (2010), In Situ Chemical Characterization of Aged Biomass-Burning Aerosols Impacting Cold Wave Clouds, *J Atmos Sci*, *67*(8), 2451-2468.
Prospero, J. M. (1996), Saharan dust transport over the North Atlantic Ocean and Mediterranean: An overview, *Envir Sci Tech Lib*, *11*, 133-151.
Pumphrey, H. C., R. E. Cofield, M. J. Filipiak, and N. J. Livesey (2009), An all-sky survey at 230 GHz by MLS on Aura, *Advances in Space Research*, *43*(3), 342-348.
Ramanathan, V., P. J. Crutzen, J. T. Kiehl, and D. Rosenfeld (2001), Atmosphere - Aerosols, climate, and the hydrological cycle, *Science*, *294*(5549), 2119-2124.
Redemann, J., M. A. Vaughan, Q. Zhang, Y. Shinozuka, P. B. Russell, J. M. Livingston, M. Kacenelenbogen, and L. A. Remer (2012), The comparison of MODIS-Aqua (C5) and CALIOP (V2 & V3) aerosol optical depth, *Atmos Chem Phys*, *12*(6), 3025-3043.
Remer, L. A., et al. (2002), Validation of MODIS aerosol retrieval over ocean, *Geophys Res Lett*, *29*(12).
Remer, L. A., et al. (2005), The MODIS aerosol algorithm, products, and validation, *J Atmos Sci*, *62*(4), 947-973.
Riemann-Campe, K., K. Fraedrich, and F. Lunkeit (2009), Global climatology of Convective Available Potential Energy (CAPE) and Convective Inhibition (CIN) in ERA-40 reanalysis, *Atmos Res*, *93*(1-3), 534-545.
Rienecker, M. M., et al. (2011), MERRA: NASA's Modern-Era Retrospective Analysis for Research and Applications, *J Climate*, *24*(14), 3624-3648.
Rosenfeld, D. (1999), TRMM observed first direct evidence of smoke from forest fires inhibiting rainfall, *Geophys Res Lett*, *26*(20), 3105-3108.

Rosenfeld, D. (2000), Suppression of rain and snow by urban and industrial air pollution, *Science*, *287*(5459), 1793-1796.
Rosenfeld, D. (2006), Aerosol-cloud interactions control of earth radiation and latent heat release budgets, *Space Sci Rev*, *125*(1-4), 149-157.
Rosenfeld, D., and I. M. Lensky (1998), Satellite-based insights into precipitation formation processes in continental and maritime convective clouds, *B Am Meteorol Soc*, *79*(11), 2457-2476.
Rosenfeld, D., and W. L. Woodley (2000), Deep convective clouds with sustained supercooled liquid water down to-37.5 degrees C, *Nature*, *405*(6785), 440-442.
Rosenfeld, D., S. Sherwood, R. Wood, and L. Donner (2014a), Climate Effects of Aerosol-Cloud Interactions, *Science*, *343*(6169), 379-380.
Rosenfeld, D., M. Fromm, J. Trentmann, G. Luderer, M. O. Andreae, and R. Servranckx (2007), The Chisholm firestorm: observed microstructure, precipitation and lightning activity of a pyro-cumulonimbus, *Atmos Chem Phys*, *7*, 645-659.
Rosenfeld, D., U. Lohmann, G. B. Raga, C. D. O'Dowd, M. Kulmala, S. Fuzzi, A. Reissell, and M. O. Andreae (2008), Flood or drought: How do aerosols affect precipitation?, *Science*, *321*(5894), 1309-1313.
Rosenfeld, D., et al. (2014b), Global observations of aerosol-cloud-precipitation-climate interactions, *Rev Geophys*, *52*(4), 750-808.
Satheesh, S. K., and V. Ramanathan (2000), Large differences in tropical aerosol forcing at the top of the atmosphere and Earth's surface, *Nature*, *405*(6782), 60-63.
Schumacher, C., R. A. Houze, and I. Kraucunas (2004), The tropical dynamical response to latent heating estimates derived from the TRMM precipitation radar, *J Atmos Sci*, *61*(12), 1341-1358.
Sherwood, S. (2002), A microphysical connection among biomass burning, cumulus clouds, and stratospheric moisture, *Science*, *295*(5558), 1272-1275.
Sherwood, S. C. (2002), Aerosols and ice particle size in tropical cumulonimbus, *J Climate*, *15*(9), 1051-1063.
Solomon, S., J. S. Daniel, R. R. Neely, J. P. Vernier, E. G. Dutton, and L. W. Thomason (2011), The Persistently Variable "Background" Stratospheric Aerosol Layer and Global Climate Change, *Science*, *333*(6044), 866-870.
Stephens, G. L., et al. (2002), The cloudsat mission and the a-train - A new dimension of space-based observations of clouds and precipitation, *B Am Meteorol Soc*, *83*(12), 1771-1790.
Stevens, B., and G. Feingold (2009), Untangling aerosol effects on clouds and precipitation in a buffered system, *Nature*, *461*(7264), 607-613.
Su, H., J. H. Jiang, X. H. Lu, J. E. Penner, W. G. Read, S. Massie, M. R. Schoeberl, P. Colarco, N. J. Livesey, and M. L. Santee (2011), Observed Increase of TTL Temperature and Water Vapor in Polluted Clouds over Asia, *J Climate*, *24*(11), 2728-2736.
Tackett, J. L., and L. Di Girolamo (2009), Enhanced aerosol backscatter adjacent to tropical trade wind clouds revealed by satellite-based lidar, *Geophys Res Lett*, *36*.
Tao, W. K., J. P. Chen, Z. Q. Li, C. Wang, and C. D. Zhang (2012), Impact of Aerosols on Convective Clouds and Precipitation, *Rev Geophys*, *50*.

Tao, W. K., S. Lang, W. S. Olson, R. Meneghini, S. Yang, J. Simpson, C. Kummerow, E. Smith, and J. Halverson (2001), Retrieved vertical profiles of latent heat release using TRMM rainfall products for February 1988, *J Appl Meteorol*, *40*(6), 957-982.
Tao, W. K., et al. (2006), Retrieval of latent heating from TRMM measurements, *B Am Meteorol Soc*, *87*(11), 1555-+.
Thorpe, A. J., M. J. Miller, and M. W. Moncrieff (1982), Two-Dimensional Convection in Non-Constant Shear - a Model of Mid-Latitude Squall Lines, *Q J Roy Meteor Soc*, *108*(458), 739-762.
Torres, O., H. Jethva, and P. K. Bhartia (2012), Retrieval of Aerosol Optical Depth above Clouds from OMI Observations: Sensitivity Analysis and Case Studies, *J Atmos Sci*, *69*(3), 1037-1053.
Tulet, P., K. Crahan-Kaku, M. Leriche, B. Aouizerats, and S. Crumeyrolle (2010), Mixing of dust aerosols into a mesoscale convective system Generation, filtering and possible feedbacks on ice anvils, *Atmos Res*, *96*(2-3), 302-314.
Turner, D. D., R. A. Ferrare, and L. A. Brasseur (2001), Average aerosol extinction and water vapor profiles over the southern great plains, *Geophys Res Lett*, *28*(23), 4441-4444.
Twomey, S. (1977), Influence of Pollution on Shortwave Albedo of Clouds, *J Atmos Sci*, *34*(7), 1149-1152.
Van Den Heever, S. C., and W. R. Cotton (2007), Urban aerosol impacts on downwind convective storms, *J Appl Meteorol Clim*, *46*(6), 828-850.
van den Heever, S. C., G. G. Carrio, W. R. Cotton, P. J. DeMott, and A. J. Prenni (2006), Impacts of nucleating aerosol on Florida storms. Part I: Mesoscale simulations, *J Atmos Sci*, *63*(7), 1752-1775.
Varnai, T., and A. Marshak (2009), MODIS observations of enhanced clear sky reflectance near clouds, *Geophys Res Lett*, *36*.
Vernier, J. P., L. W. Thomason, and J. Kar (2011), CALIPSO detection of an Asian tropopause aerosol layer, *Geophys Res Lett*, *38*.
Weisman, M. L., and R. Rotunno (2004), "A theory for strong long-lived squall lines'' revisited, *J Atmos Sci*, *61*(4), 361-382.
Wing, A. A., and K. A. Emanuel (2014), Physical mechanisms controlling self-aggregation of convection in idealized numerical modeling simulations, *J Adv Model Earth Sy*, *6*(1), 59-74.
Winker, D. M., M. A. Vaughan, A. Omar, Y. X. Hu, K. A. Powell, Z. Y. Liu, W. H. Hunt, and S. A. Young (2009), Overview of the CALIPSO Mission and CALIOP Data Processing Algorithms, *J Atmos Ocean Tech*, *26*(11), 2310-2323.
Wu, D. L., J. H. Jiang, W. G. Read, R. T. Austin, C. P. Davis, A. Lambert, G. L. Stephens, D. G. Vane, and J. W. Waters (2008), Validation of the Aura MLS cloud ice water content measurements, *J Geophys Res-Atmos*, *113*(D15).
Zhang, D. M., Z. Wang, and D. Liu (2010), A global view of midlevel liquid-layer topped stratiform cloud distribution and phase partition from CALIPSO and CloudSat measurements, *J Geophys Res-Atmos*, *115*.
Zhang, R. Y., G. H. Li, J. W. Fan, D. L. Wu, and M. J. Molina (2007), Intensification of Pacific storm track linked to Asian pollution, *P Natl Acad Sci USA*, *104*(13), 5295-5299.

Zipser, E. J. (1977), Mesoscale and Convective-Scale Downdrafts as Distinct Components of Squall-Line Structure, *Mon Weather Rev*, *105*(12), 1568-1589.
Zipser, E. J. (2003), Some Views On "Hot Towers" after 50 Years of Tropical Field Programs and Two Years of TRMM Data, in *Cloud Systems, Hurricanes, and the Tropical Rainfall Measuring Mission (TRMM): A Tribute to Dr. Joanne Simpson*, edited by W.-K. Tao and R. Adler, pp. 49-58, American Meteorological Society, Boston, MA.
Zou, H., and T. Hastie (2005), Regularization and variable selection via the elastic net (vol B 67, pg 301, 2005), *J Roy Stat Soc B*, *67*, 768-768.